MONITORING AND ANALYSIS OF FROZEN DEBRIS LOBES USING REMOTE SENSING

OASRTRS-14-H-UAF-B

Final Report

Principal Investigator:

Dr. Margaret M. Darrow

University of Alaska Fairbanks

Co-Investigators:

Dr. Franz Meyer, Dr. Keith W. Cunningham

Contributors:

Dr. Wenyu Gong, Nora L. Gyswyt, Ryan P. McCoy, Dr. Ronald P. Daanen, David McAlpin

Program Manager:

Mr. Caesar Singh

Office of the Assistant Secretary for Research and Technology

U.S. Department of Transportation

EXECUTIVE SUMMARY

Frozen debris lobes (FDLs) are slow-moving landslides within permafrost on slopes located in the Brooks Range of Alaska. Forty-three FDLs are located within the Dalton Highway corridor, with 23 occurring less than one mile uphill of the Dalton Highway and the Trans Alaska Pipeline System (TAPS). Although slow-moving for landslides, their size and close proximity to infrastructure make FDLs geohazards. This project used remotely sensed data from multiple acquisition methods to monitor and analyze FDLs at different temporal scales, thereby increasing our understanding of rates and episodes of movement of these geohazards. Each technique was evaluated for its overall cost, east of use, and applicability to assess the flow dynamics of FDLs. This research involved: 1) measuring surface movement in the field with a differential GPS unit; 2) analyzing remotely sensed data using multiple data acquisition methods (i.e., historic optical imagery, LiDAR data, InSAR data, and UAS-acquired photography) to monitor and analyze the FDLs at different temporal scales; and 3) summarizing and synthesizing the research results, making them available to the public and to the agencies with a vested interest in FDLs through several different deliverable formats.

The results of this integrated research indicate:

- The rate of motion of FDLs has increased over the last 60 years, with the eight FDLs investigated moving asynchronously to each other.
- In the last 40 years, scarps have developed in the catchments of the investigated FDLs, which may indicate increasing instability.
- The movement dynamics across the surface of a given FDL vary significantly throughout the year.
- All of the investigated FDLs demonstrated a maximum rate movement in late October, and a minimum rate of movement in late February.
- The closest FDL to the Dalton Highway is FDL-A.
    - As of October 2016, FDL-A was 32.2m from the toe of the highway embankment.
    - It moved at an average rate of 6.4m/yr over 2015/16, and its rate steadily increased over the measurement period.
    - Based on these values, FDL-A will reach the Dalton Highway by 2021.
    - FDL-A is impacting the subsurface ahead of its toe, possibly shearing deeper that the original ground surface.
    - When FDL-A impacts the highway, its narrowest portion will deposit over 19m^3 (or 25yd^3) of material on the highway every day. This equates to about two dump truck loads a day, and does not consider that FDL-A becomes wider uphill.

The results of this research were disseminated through a variety of sources, including two peer-reviewed journal papers and eight conference papers. Links to the documents available from the internet are provided on the project website (www.fdlalaska.org). Also available on the website are two short videos developed as part of this research, which describe the relative scale and shape of FDLs, and illustrate their downslope progression through time. Finally, accompanying this report is a “best practices guide”, which briefly lists the pros and cons of each method used in this research.

ACKNOWLEDGEMENTS

This research was funded by USDOT grant: OASRTRS-14-H-UAF-Project B. We would like to acknowledge the ongoing support provided by the Alyeska Pipeline Service Company and the Alaska Department of Transportation and Public Facilities. We also recognize the efforts and thank our colleagues from the Geographic Information Network of Alaska.

DISCLAIMER

GLOSSARY OF TERMS

3D – Three-dimensional

ADAS – Automated Data Acquisition System

ADOT&PF – Alaska Department of Transportation and Public Facilities

AHAP – Alaska High Altitude Photography

AOI – Area of Interest

ASF – Alaska Satellite Facility

bgs – below ground surface

d-InSAR – Differential InSAR

DEM – Digital Elevation Model

DGGS- Alaska Division of Geological & Geophysical Surveys

DGPS – Differential Global Positioning System unit

DLR – German Aerospace Center

DoD – DEM of Difference

DSM – Digital Surface Model

ERS – European Remote Sensing

ESA – European Space Agency

FDL – Frozen Debris Lobe

GCPs – Ground Control Points

GCS – Ground Control Stations

GSD – Ground Sample Distance

GSP – Ground Survey Point

GINA – Geographic Information Network of Alaska

GIS – Geographic Information System

IfSAR/InSAR – Interferometric Synthetic Aperture Radar

IW – Interferometry Wide-swath mode

LiDAR – Light Detection and Ranging

MEMS – Micro-electro-mechanical Systems

M-IPI – MEMS-based In-Place Inclinometer

MCF – Minimum Cost Flow

NDL – Non-Debris Lobe

PALSAR – Phased Array type L-band Synthetic Aperture Radar

QA/QC – Quality Assurance / Quality Control

QSI – Quantum Spatial, Inc.

RTS – Retrogressive Thaw Slump

S1A – Sentinel-1A satellite

SAR – Synthetic Aperture Radar

SfM – Structure-from-Motion

SLC – Single-Look-Complex

TAPS – Trans Alaska Pipeline System

TIN – Triangulated Irregular Network

TSX – TerraSAR-X

USDOT – US Department of Transportation

USGS – US Geological Survey

UAF – University of Alaska Fairbanks

UAS – Unmanned Aircraft System

TABLE OF CONTENTS

Page

LIST OF FIGURES

LIST OF TABLES

CHAPTER 1: INTRODUCTION

Frozen debris lobes (FDLs) are slow-moving landslides within permafrost on slopes located in the Brooks Range of Alaska. Forty-three FDLs exist within the Dalton Highway corridor, with 23 occurring less than one mile uphill of the Dalton Highway and the Trans Alaska Pipeline System (TAPS). Although slow-moving for landslides, their size and close proximity to infrastructure make FDLs geohazards.

This research employed remotely sensed data from multiple acquisition methods to monitor and analyze FDLs at different temporal scales, thereby increasing our understanding of rates and episodes of movement of these potential geohazards. Each technique was evaluated for its overall cost, ease of use, and applicability to assess the flow dynamics of FDLs. Thus, the results obtained from this study fall into two overall categories: 1) advancing the science and understanding of this specific geohazard; and 2) evaluating the success of each remote sensing technique for this and other similar analyses. The results produced from this study are critical for stakeholders to make informed future decisions regarding the infrastructure and mitigation strategies of FDLs. While the work focused on these slow-moving landslides within the Brooks Range of Alaska, the results of the remote sensing evaluation are more wide-spread, as the successful techniques may be applied to other regions with forested mass-movement features having similar rates of movement.

Mirroring the dual nature of the results, this report is structured in two parts. Part I details the specific measurements, results, and analyses made to improve our understanding of FDLs. Part II is a summary of the performance of each of the remote sensing methods employed. Accompanying this report is a short guide summarizing these best management practices, which is intended to provide an at-a-glance summary for the practitioner searching for the correct method for a specific application.

CHAPTER 2: SUMMARY OF PREVIOUS FROZEN DEBRIS LOBE RESEARCH

FDLs were identified initially by several individuals working along the proposed Dalton Highway corridor in the 1970's and early 1980's (Hamilton 1978, 1979, 1981; Kreig and Reger 1982; Brown and Kreig 1983). These authors thought that they were inactive, and called them by other names, including flow slides and rock glaciers. In 2008, Daanen (collaborator on this project) observed features that led him to believe that several of the FDLs were indeed moving. Through preliminary remote sensing analysis and field investigations, Daanen et al. (2012) established initial estimates of movement for four FDLs (FDL-A, -B, -C, and –D). In 2011, Darrow joined Daanen to make observations of the FDLs. In 2012, Darrow and Daanen conducted a geotechnical subsurface investigation of FDL-A (funded by the Alaska University Transportation Center and the Alaska Department of Transportation and Public Facilities (ADOT&PF) (Grant No. DTR T06-G-0011 and T2-12-17). During the investigation, geotechnical instrumentation, including a micro-electro-mechanical systems (MEMS)-based in-place inclinometer (M-IPI), thermistors, and vibrating wire piezometers, were installed within FDL-A, and marker pins were installed on the surface of FDL-A for repeat measurements using a differential global positioning system (DGPS) device. Results from the 2012 project indicated that FDL-A moves mostly through shear in a zone 20.9 to 22.5m below the ground surface (bgs), and that it moves faster than suggested by the preliminary remote sensing analysis. Results from the 2012 investigation and subsequent analyses are detailed in Darrow et al. (2012; 2013; 2015).

In 2013 and 2014, the research was expanded to include seven additional FDLs. Funded by a Capital Improvement Project from the Alaska Division of Geological & Geophysical Surveys (DGGS) and the US Department of Transportation (USDOT) (Grant No. DTRT06-G-0011), the research team: 1) collected samples of rocks from each of the FDL catchments for assessment of rock strength and to refine existing geologic maps of the area of interest (AOI); 2) sampled the near-surface soils (upper 1m) of each of the FDLs to determine engineering index properties; and 3) installed surface marker pins on the additional FDLs to determine their movement rates. Results from that project indicated that: 1) the bedrock comprising each of the FDL catchments consists of mostly low-strength, heavily fractured, platy and foliated metamorphic rocks; 2) all of the FDLs consist of silty sand with gravel (or slight variations thereof); and 3) the eight FDLs investigated currently move at a variety of rates. Results from the 2013/14 investigation are included in Darrow (2015), Darrow et al. (2016), Hubbard et al. (2013), Simpson et al. (2016), Spangler et al. (2013), and two publications currently in review (Simpson et al. (in review), and Spangler and Hubbard (in review)).

CHAPTER 3: PART I - CURRENT FDL RESEARCH RESULTS

3.1 Monitoring surface movement on FDL-A, and additional FDLs

As part of this project, the research team continued the monitoring started in late 2012 on FDL-A, and in 2013 for seven additional FDLs. The original goal was to monitor the seven FDLs accessible from the Dalton Highway; however, helicopter support provided by the Alyeska Pipeline Service Company (Alyeska) allowed access to FDL-7 across the Dietrich River on several occasions. Figure 3.1 is a location map of the AOI relative to the closest communities on the road system in Alaska, and the locations of the eight investigated FDLs within the AOI. Table 3.1 is a summary of the trips to the field made during this project.

During each trip to the field, the locations of surface marker pins were measured using a Leica DGPS unit, having horizontal and vertical accuracies of ±5cm. Figure 3.2 is an example of the results from the surface movement monitoring for FDL-A over the 2015-16 monitoring period. The direction of displacement of each surface marker pin is indicated by an arrow, and the annual amount of movement in meters for each pin is indicated in text next to the arrow. Appendix A contains surface movement maps for each of the FDLs for both the 2014-15 and 2015-16 measurement periods. Figure 3.3 is a summary of the annualized movement rates from late 2012 (for FDL-A) to 2016 for all of the measured FDLs, with trend lines shown for the summer rates (i.e., May/June to August) from 2013 to 2016. With the exception of FDL-11, the rates of movement of all FDLs have increased over the measurement period, with the final measurements in August 2016 yielding the largest summer rates recorded. The 2012 early winter rates measured on FDL-A indicated that it moved the fastest in late October, which also was supported by subsurface movement rates and historic InSAR analysis (discussed in Section 3.2.3). To confirm this early set of measurements, an additional set of measurements were collected on October 22, 2016 to determine late fall / early winter rates for FDL-A. As presented in Figure 3.3, the 2016 October rates for FDL-A were high and in the same range as those measured in October 2012, indicating the possible peak movement period. As of October 2016, FDL-A was 32.3m from the toe of the Dalton Highway embankment. At its current rate of movement, FDL-A will reach the embankment by 2021. Table 3.2 is a summary of the average rates of movement for all of the monitored FDLs, and their 2016 distances to the Dalton Highway and TAPS.

On each trip to FDL-A, data was downloaded from three automated data acquisition systems (ADAS) installed during the 2012 geotechnical investigation; and inclinometer casings installed adjacent to FDL-A, and between its toe and the toe of the Dalton Highway embankment, were measured (see Figure 3.4 for locations). These instrument installations have yielded tremendously useful data about the subsurface temperatures, water pressure, and rate of movement. Unfortunately, the research team discovered the main ADAS lying knocked over on the ground under the snow and dysfunctional in April 2016. After recovering and analyzing its data, it is suspected that sometime between September 5 and September 6, 2015, a moose became entangled in the flexible casing leading from the ADAS to the boring, knocking over the ADAS and breaking the M-IPI installed within the boring. During the May and August 2016 trips, the ADAS and some of its components were repaired in order to have an operating weather station on FDL-A.

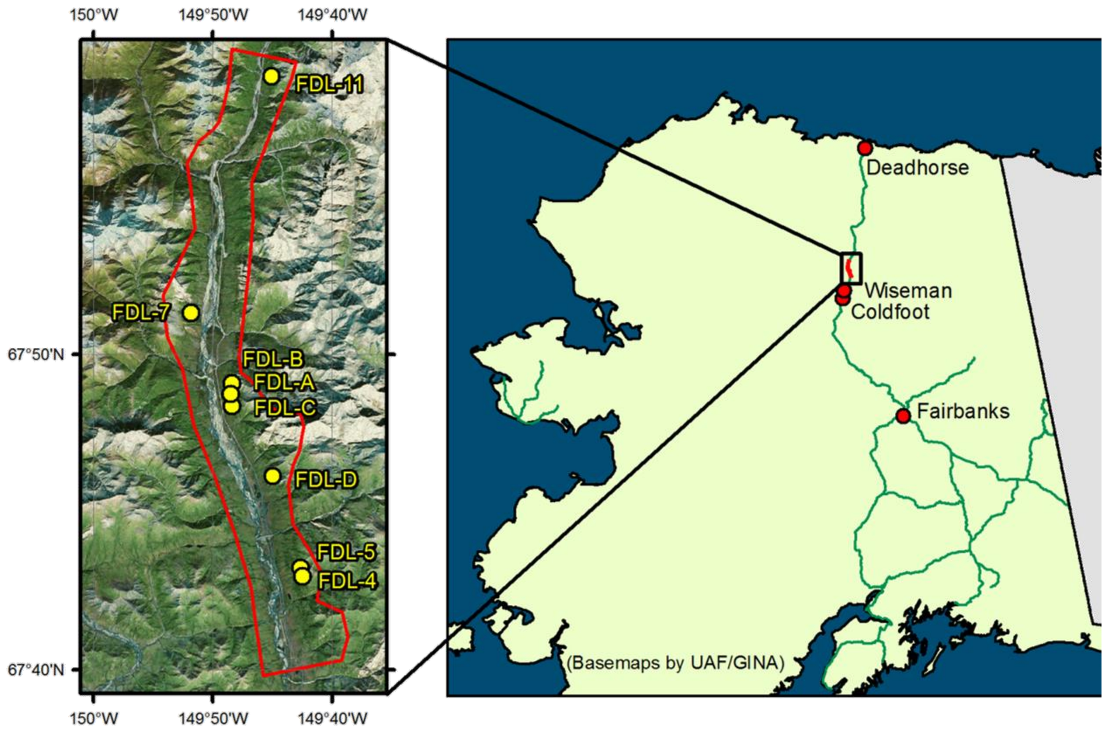

Figure 3.1. Location map of the Area of Interest (AOI), in relation to Fairbanks, Coldfoot, and Deadhorse, Alaska. Inset details the distribution of the eight investigated FDLs. (Base map from GINA 2016).

Table 3.1. Summary of field work done for monitoring FDLs.

Dates	FDLs Visited, Purpose
March 13-15, 2015	FDL-A: collect surface marker measurements; download data
May 16-22, 2015	All measured FDLs: collect surface marker measurements; collect ground survey points for LiDAR collection; download data; measure inclinometers (FDL-A)
August 16-22, 2015	All measured FDLs: collect surface marker measurements; download data; measure inclinometers (FDL-A)
April 14-16, 2016	FDL-A: collect surface marker measurements; download data
May 23-27, 2016	All measured FDLs (except FDL-7): collect surface marker measurements; download data; measure inclinometers (FDL-A)
August 14-20, 2016	All measured FDLs: collect surface marker measurements; download data; measure inclinometers (FDL-A)

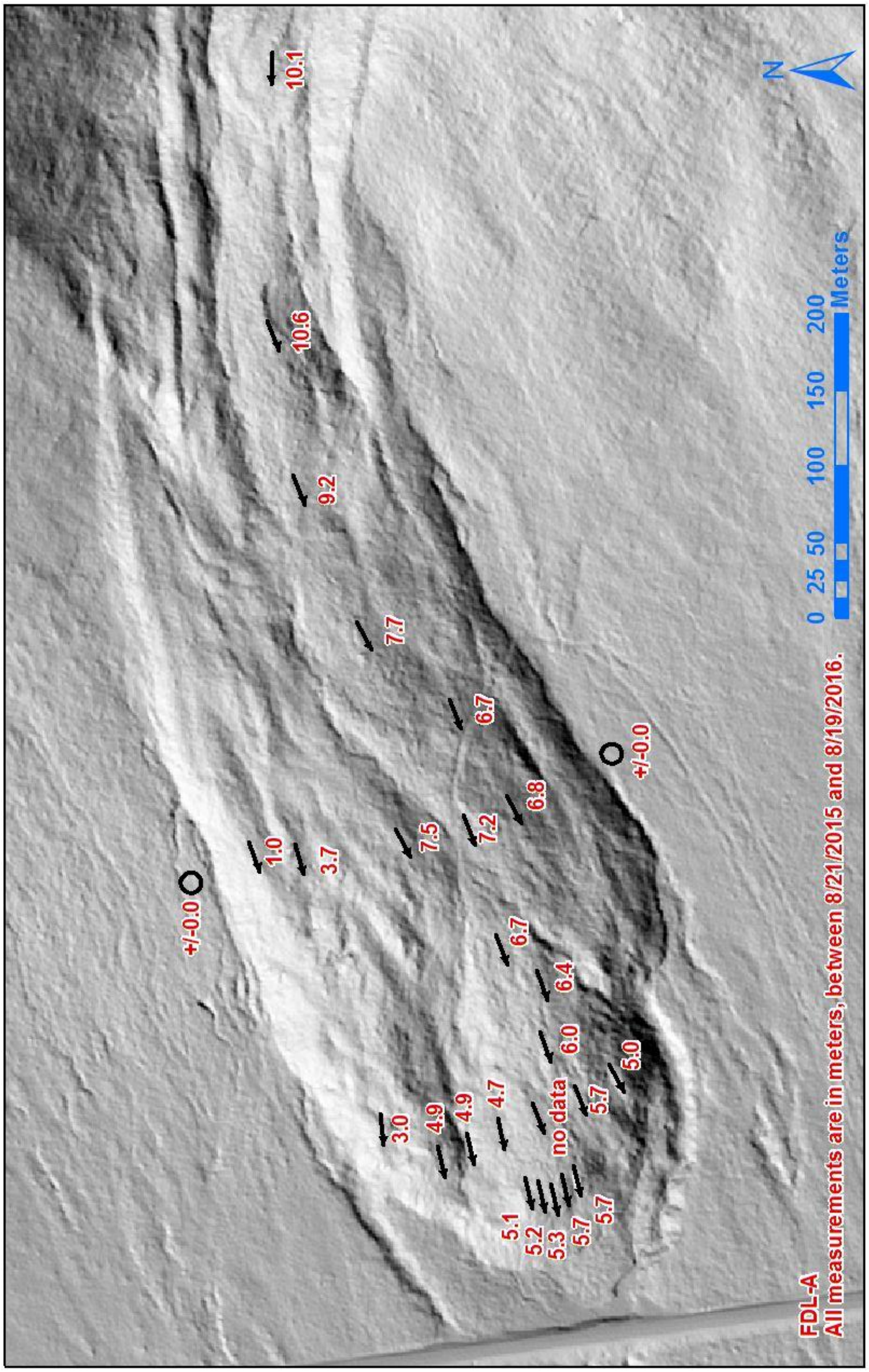

Figure 3.2. Spatial distribution of yearly movement for FDL-A. Values shown are in meters and indicate the amount of movement measured between August 21, 2015 and August 19, 2016.

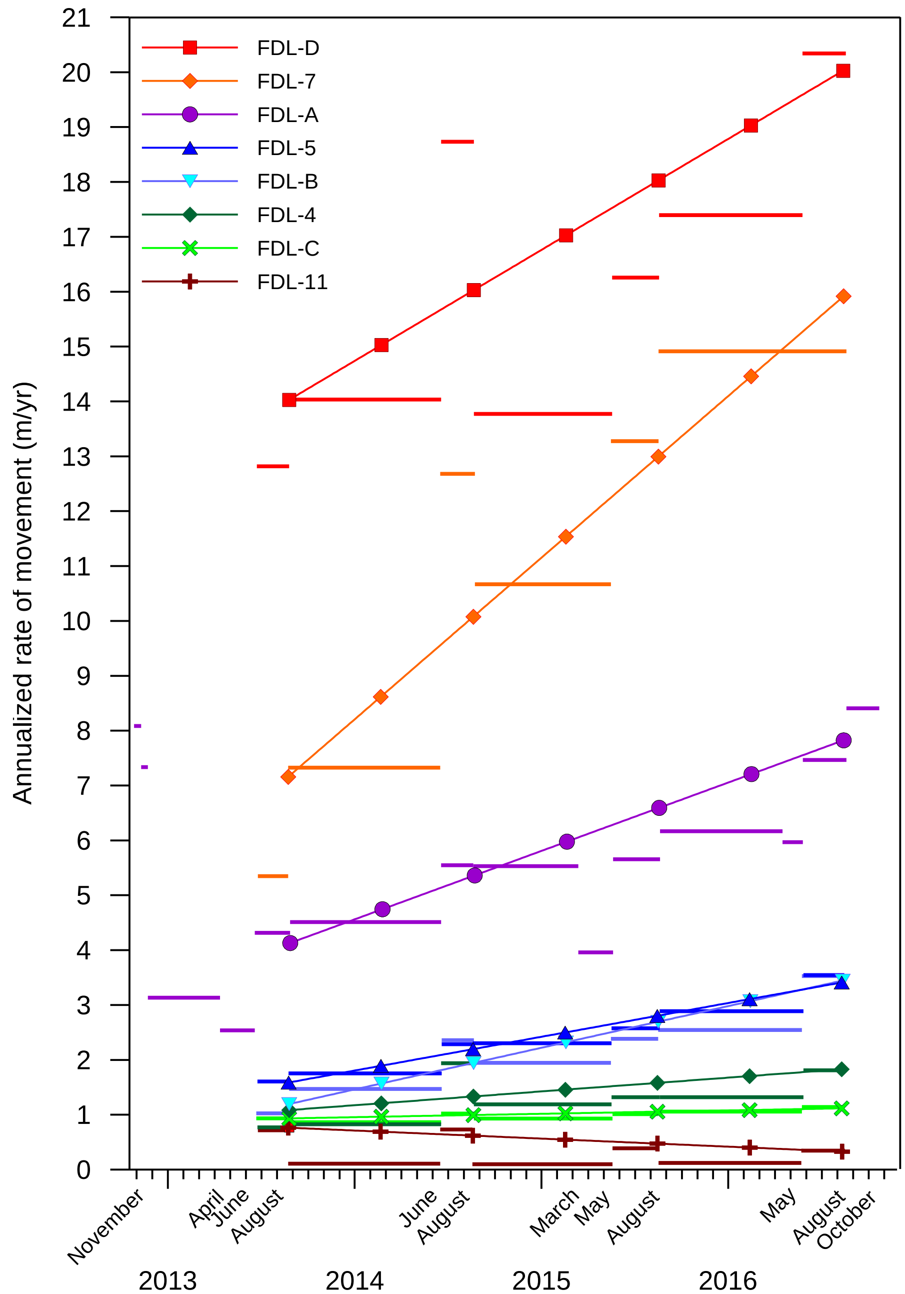

Figure 3.3. Rate of movement summary for the eight investigated FDLs. All rates are annualized and indicate the average rate of movement between two measurement periods. Trend lines indicate the average rate trend based on May/June to August measurements from 2013 to 2016 (markers on trend lines are for better visualization and do not indicate specific measurements).

Table 3.2. Summary of average rates for surface markers on eight FDLs measured between August 2013 and August 2016. The FDLs are listed in descending order of annual average rate, and averages do not include control points or stakes on levees. FDL-D rate does not include points above detachment area. Distance to the Trans Alaska Pipeline System (TAPS) is based on a shapefile of the pipe centerline from Alaska Department of Natural Resources.

FDL	Avg. rate Aug 2013-14 (m/yr)	Avg. rate Aug 2014-15 (m/yr)	Avg. rate Aug 2015-16 (m/yr)	2016 distance to highway (m)	2016 distance to TAPS (m)
FDL-D	16.2	15.0	19.1	398	936
FDL-7	8.6	11.2	15.0	---	---
FDL-A	4.6	5.2	6.4	32.3	264
FDL-5	1.9	2.4	3.0	968	1,026
FDL-B	1.6	2.0	2.8	422	637
FDL-4	1.0	1.2	1.4	1,075	1,024
FDL-C	0.9	0.9	1.1	198	363
FDL-11	0.2	0.2	0.2	229	334

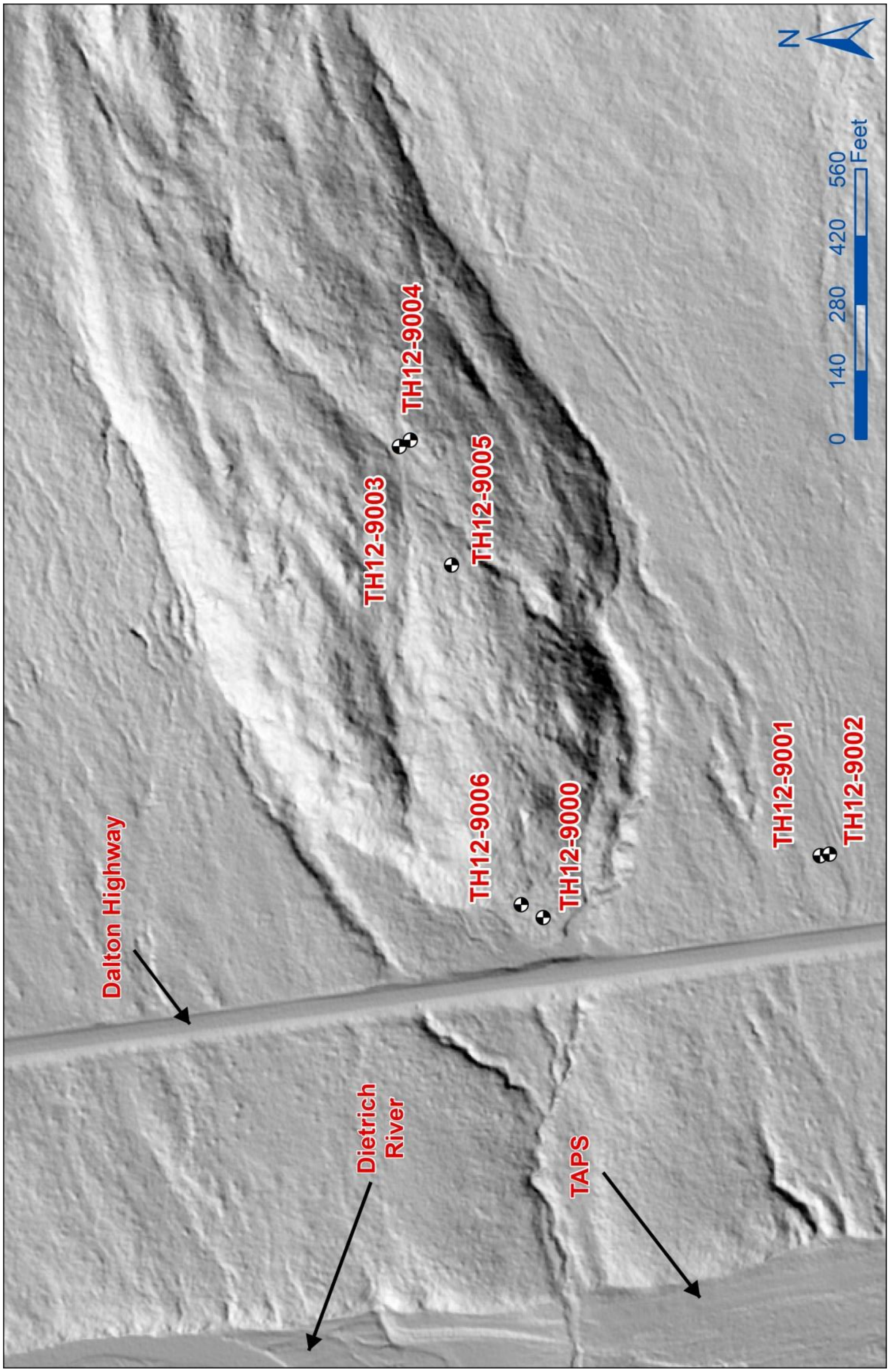

Figure 3.4. Locations of borings from 2012 subsurface investigation. ADAS installations are located at TH12-9001, TH12-9004, and TH12-9005.

Figure 3.5 is a graphical summary of the motion within FDL-A over the operating life of the M-IPI. The bottom of the M-IPI sheared off approximately one month after installation in 2012 (Darrow et al. 2012); however, the upper portion continued to report data until it was severed at the top in September 2015. Using DGPS measurements to locate the upper measurement point, the upper portion of the M-IPI moved 15.7m downhill between 2012 and 2015. While FDL-A moves mostly through shear at its base, it also demonstrates an internal flow or creep. Analysis of the M-IPI data, surface and sub-surface temperatures suggests that this motion is temperature-dependent, with FDL-A experiencing a peak in movement approximately four months after the peak in surface temperatures (Darrow and Daanen 2016).

Another part of the field work at FDL-A was measuring inclinometer casing with a manual inclinometer probe. Figure 3.6a contains the inclinometer measurements from the "undisturbed" site to the south of FDL-A (TH12-9002). These data demonstrate just over 3cm of downslope movement near the surface, with all movement contained within the active layer depth (i.e., the upper 1.5m). These data are typical of seasonal downslope soil movement on a permafrost slope. Another casing (TH12-9000) was installed in September 2012 between FDL-A and the highway embankment; unfortunately, the upper portion of this critical casing was broken at the surface sometime before June 2013. Thus, the current analysis only includes movement since "resetting" the inclinometer readings in August 2013 (Figure 3.6b). While the small movement within the casing TH12-9000 could be attributed to movement within the active layer, comparison of Figures 3.6a and 3.6b illustrates that TH12-9000's movement is fundamentally different in nature than at the undisturbed site. The May 2016 readings indicate that the casing continued to deform downslope, and that the deformation propagated from 2m to 3m bgs between 2015 and 2016. Although the magnitude of downslope movement is small (only a few cm), the movement is present throughout the entire soil profile until the bedrock surface (approximately 3m bgs). These measurements indicate that the subsurface between FDL-A and the highway is beginning to see small effects from the approaching FDL. Thus, <u>FDL-A is impacting the subsurface ahead of the toe, which suggests it may be shearing deeper than the ground surface</u>. Although the M-IPI and inclinometer measurements are a legacy from previous ADOT&PF funding, these data continue to provide important insights into the nature of FDL-A's movement, and potential success or failure of various mitigation methods.

3.2 Using remote sensing techniques to monitor and analyze FDLs at different temporal scales

3.2.1 <u>Decadal scale: Historic rates of movement</u>

Several sources were used to identify potential scenes for the AOI, including USGS EarthExplorer, Alaska High Altitude Photography (AHAP), and satellite imagery from DigitalGlobe WorldView. Scenes that covered portions of the AOI were evaluated for cloud coverage, obscuring smoke or haze, look angle, shadows, and overall resolution. Table 3.3 contains a summary of the final years of coverage and sources used to produce ortho-mosaics for the AOI. Personnel with the Geographic Information Network of Alaska (GINA) orthorectified and produced mosaics from the imagery. Two digital elevation models (DEM) were created

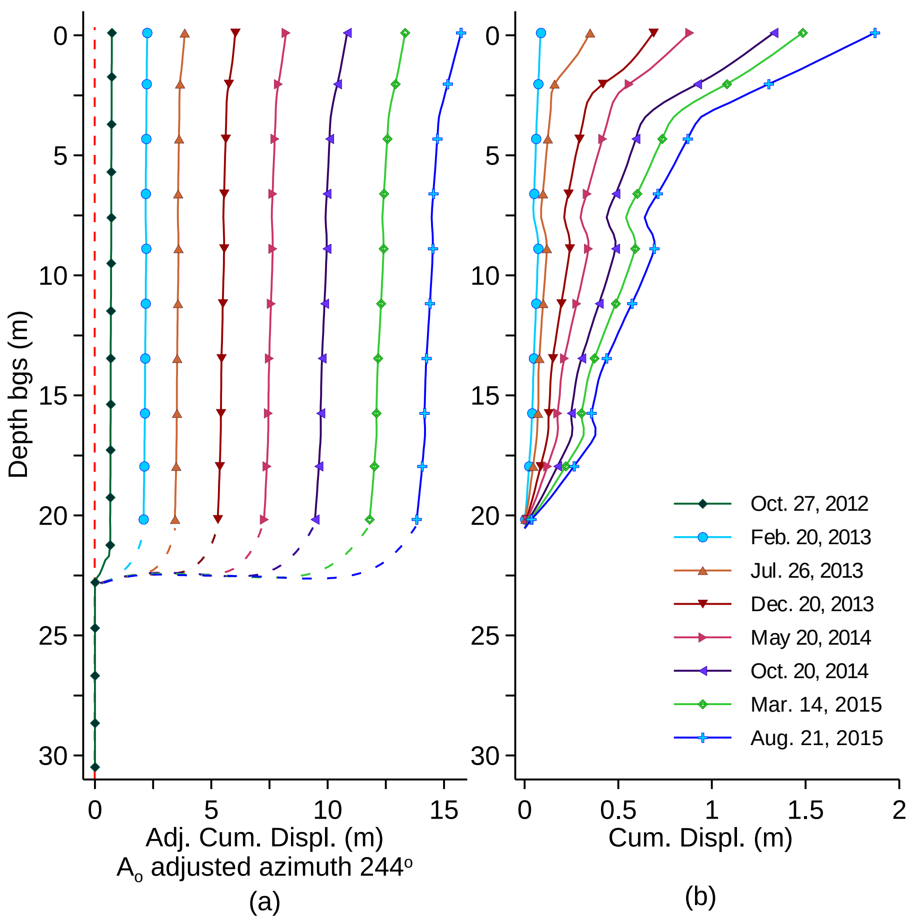

Figure 3.5. M-IPI data for TH12-9005 within FDL-A from initial installation to August 21, 2015.

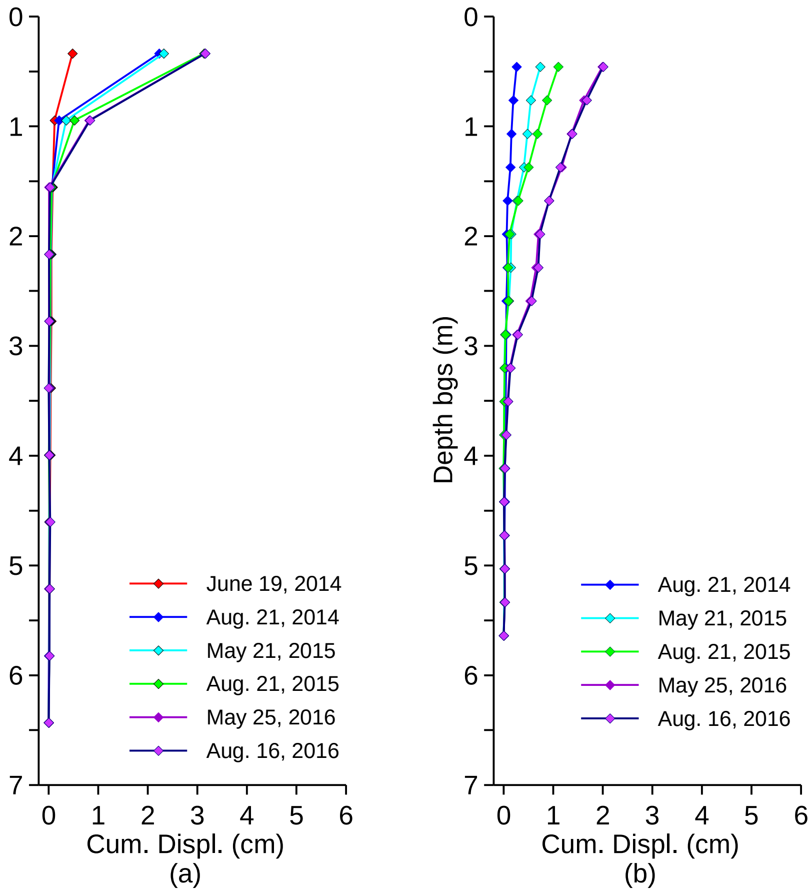

Figure 3.6. Manual inclinometer measurements of (a) TH12-9002, and (b) TH12-9000. All data were corrected using vector summation (Cornforth 2005).

Table 3.3. Summary of historic aerial photography and satellite imagery year of collection, source, resolution, and FDL coverage. USGS is the U.S. Geological Survey, AHAP stands for Alaska High-Altitude Photography, and DGGS is the Alaska Division of Geological & Geophysical Surveys. If all FDLs are covered by a given data set, “NONE” is stated under Limitations.

Year	Source	Resolution (m)	Limitations in FDL coverage
1955	USGS (Aerial)	1.78	NONE
1970	AHAP (Aerial)	2.0	NONE
1978	AHAP (Aerial)	1.5	no FDL-5, -4
1979	AHAP (Aerial)	1.5	only FDL-11, -7, -B
1981	AHAP (Aerial)	1.5	only FDL-D, -5, -4
1993	Quantum Spatial (Aerial)	0.3	NONE
2007	DigitalGlobe Ikonos (Satellite)	1.5	only FDL-7, FDL-B
2009	DigitalGlobe WorldView (Satellite)	0.5	no FDL-11
2011	DGGS (LiDAR)	1.0	NONE
2014	DigitalGlobe WorldView (Satellite)	0.5	NONE

using 2001 Interferometric Synthetic Aperture Radar (IfSAR) data (GINA 2001) and 2011 Light Detection and Ranging (LiDAR) data (Hubbard et al. 2011), which were evaluated for quality assurance / quality control (QA/QC) during the historic imagery ortho-mosaic process. Metadata was added to each ortho-mosaic to identify the source of scenes, and to credit those responsible for the orthorectification. All datasets were bundled and delivered to ADOT&PF and Alyeska for their use. These entities represent the main constituents that benefit from the results of this research, as they are responsible for the functionality of the adjacent infrastructure.

For each data year, each lobe was outlined in a geographic information system (GIS) environment (Figure 3.7). Movement rates for each FDL were calculated by measuring the displacement of the toe of each lobe between each available data year's outline, and then dividing the displacement by the time period each imagery pair spanned. Table 3.4 is a summary of the movement rates determined by the historical imagery analysis. The mapped outlines also provide a means for visual analysis of the morphology of each FDL as it moves downslope.

Analysis of the historic imagery results indicates two main movement rate trends, FDLs with increasing movement rates (i.e., FDL-A, -B, -D, -4, -5, and -7) and those with decreasing movement rates (i.e., FDL-C and -11). For example, FDL-B, adjacent to FDL-A to the north, moved only 0.2 m/yr in 1970, yet accelerated to 3.9 m/yr by 2014. The FDL with the greatest known rate of movement, FDL-D, moved at just 1.2 m/yr in 1970, but reached an average rate of 32.1 m/yr in 2011. FDL-7, located on the east side of the Dietrich River, is the second fastest FDL in the study group, with rates of 1.6 m/yr in 1970 and 12.2m/yr in 2014. FDL-A moved 1.9 m/yr in 1970, increasing to an average rate of 3.9 m/yr in 2014. In contrast, FDL-11 experienced a peak movement rate in 1978 at 9.4 m/yr and has steadily decreased in movement since then, with no significant change in the toe position from 2011 to 2014. This indicates that FDL movement has been asynchronous during the period of investigation. Figure 3.8 is a graphical summary of the movement rates from the analysis of the historic imagery. Over the last 60 years, seven of the eight measured FDLs demonstrated increasing rates of movement.

Vegetation coverage on the FDLs and within their catchments was analyzed on each historic image, to look for any evidence of rapid movement. This analysis was limited by imagery resolution (e.g., the 1955 imagery was not useful for this purpose), imagery coverage, shadowing, cloud cover, etc. Table 3.5 is a summary of the vegetation coverage analysis. While limited by imagery coverage, the results do indicate that the catchment of each FDL developed a scarp at some point since 1979. This may indicate increasing instability of these features.

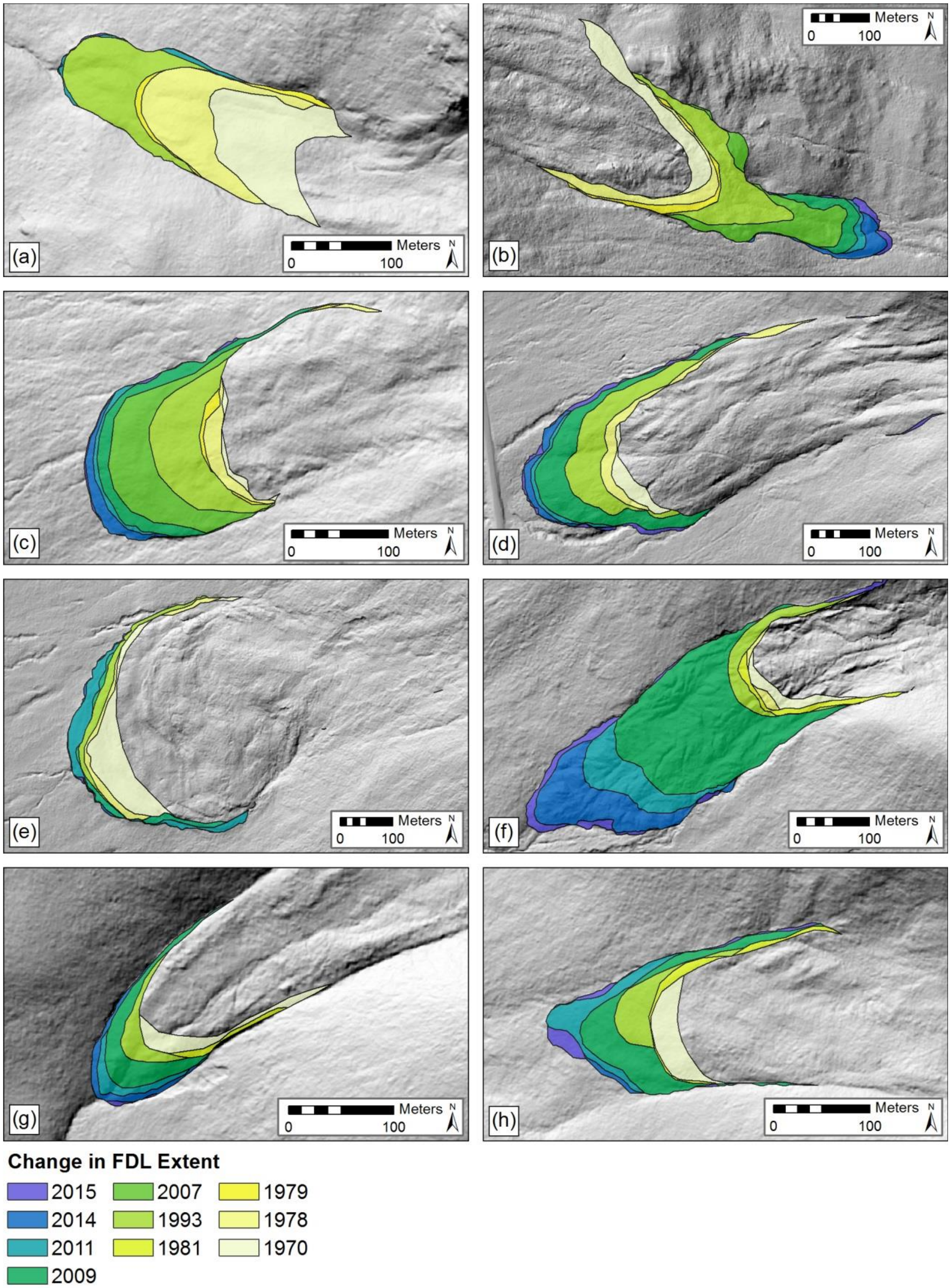

Figure 3.7. Change in FDL extent from 1955 to 2015: (a) FDL-11, (b) FDL-7, (c) FDL-B, (d) FDL-A, (e), FDL-C, (f) FDL-D, (g) FDL-5, (h) FDL-4. (Base maps from 2015 LiDAR data.)

Table 3.4. FDL average movement rates between each year of historic imagery. The '---' indicates lack of data for that lobe (see Table 3.3 for imagery limitations).

Span of data years	Movement rate (m/yr)							
	FDL-11	FDL-7	FDL-B	FDL-A	FDL-C	FDL-D	FDL-5	FDL-4
1955-1970	5.9	1.6	0.2	1.9	4.2	1.2	1.2	1.8
1970-1978	9.4	3.0	2.3	2.2	1.6	0.5	---	---
1978-1979	6.3	5.5	3.9	---	---	---	---	---
1979-1981	---	---	---	---	---	2.1	0.0	0.1
1981-1993	5.6	9.5	3.6	3.8	0.3	1.9	1.5	2.9
1993-2007	---	6.3	3.4	---	---	---	---	---
2007-2009	---	13.6	5.4	4.4	0.5	10.3	1.8	2.4
2009-2011	0.1	8.4	1.8	4.2	0.0	32.1	7.7	5.0
2011-2014	0.0	12.2	3.9	3.9	1.1	30.1	5.6	0.0

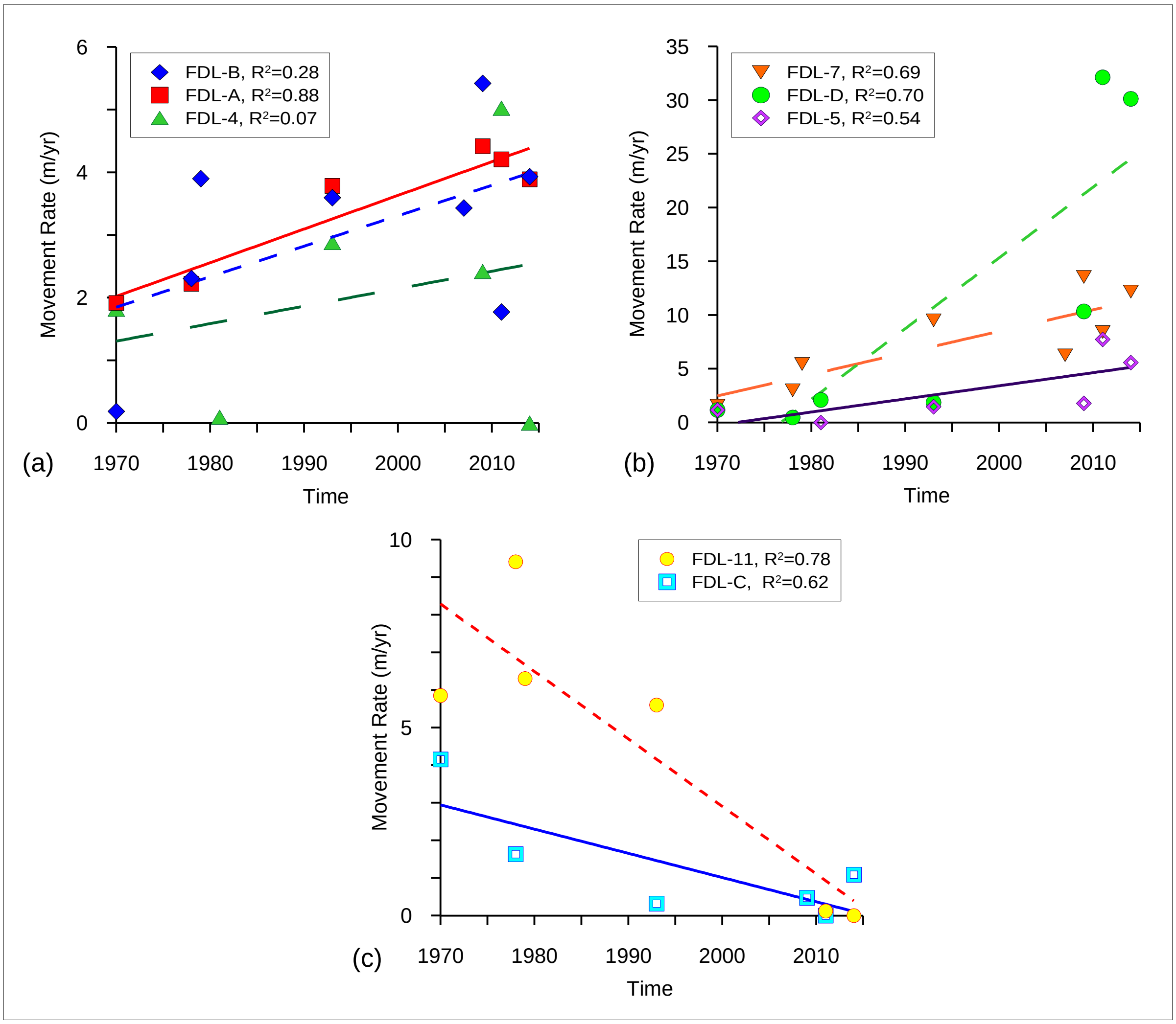

Figure 3.8 Historic FDL movement rates from 1955 to 2014 for lobes with (a) steadily increasing rates, (b) rapidly increasing rates, and (c) decreasing rates. The coefficients of correlation (R^2) for linear trend lines fitted to each lobe data set are presented in the figure legends. (Figure taken from Darrow et al. 2016).

Table 3.5. Vegetation and disturbance summary from historic imagery.

Frozen debris lobe	Summary of vegetation coverage from historic imagery
FDL-11	1978, 1979: possible scarp development on north side and across center of lobe 2002, 2007: disturbed area at toe and south flank prominent 2014: scarp healed
FDL-7	***: well-vegetated, no major scarps until 2002 2002: lower tongue developed, flanks lack vegetation 2007: two main retrogressive thaw slumps (RTSs) at lower tongue; large disturbed trees visible in middle of upper lobe 2009: RTSs increased in lateral extent 2014: lower tongue prominently lacks vegetation coverage
FDL-B	1970: scarp in middle of upper lobe, increases in size up to 2014 1979: lack of vegetation near toe becomes apparent 2014: consistent vegetation coverage over lobe
FDL-A	1970: disturbed area on north half of toe 1978: disturbed area at toe still visible, longitudinal cracks obvious 1979: scarp on north half of toe increases laterally 2002: lack of vegetation above toe, center of lobe, and around drainage 2007: greater vegetation growth on north half of toe, scarp on upper north side of lobe visible 2009: scarp on south side of toe developed
FDL-C	1970: prominent drainage into lobe through catchment 1978: upper half of lobe more thickly vegetated than lower half, similar trend until present
FDL-D	1978: lobe well-vegetated 2001: large scarp on upper lobe, lack of vegetation at toe 2002: upper scarp lengthened 2009: large amount of movement, bare earth obvious in upper scarp, transverse and longitudinal cracks 2014: poorly vegetated
FDL-5	1981: two scarps visible on north side of mid-lobe 2001: disturbed area at toe 2009: pronounced linear features
FDL-4	1981: possible transverse cracks mid-lobe 2009: forested with small trees, becoming denser towards toe 2014: pronounced linear feature on south side and center of lobe

3.2.2 Multi-year scale: 2011 to 2015 LiDAR analysis

Quantum Spatial, Inc. (QSI) was contracted in 2015 to acquire LiDAR of the AOI. QSI completed the acquisition from May 19 through 21, 2015. Two University of Alaska Fairbanks (UAF) teams were in the field at the same time, collecting DGPS and UAS data. The LiDAR data were collected under ideal weather conditions, just after snow melt and before leaf-out on the deciduous vegetation. The instrumentation used was a Leica ALS70 airborne LiDAR sensor, on board a Piper Navajo aircraft. The AOI was covered with 126 flight lines, and a minimum of 8 laser points per m^2 was achieved. Ground survey points (GSP) were collected by the UAF field team for use as redundant ground control data for LiDAR QA/QC. After delivery to UAF, the data was analyzed first by GINA for an independent QA/QC. The 2015 LiDAR coverage included all of the catchments of the investigated FDLs, several of which were not covered by the 2011 LiDAR.

To begin the LiDAR data set comparison, the 2011 DEM was subtracted from the 2015 DEM, resulting in a DEM of difference (DoD) raster that represents elevation change over the four-year time period. Figures 3.9 and 3.11 are portions of the DoD for FDL-A and FDL-D, respectively, and Figures 3.10 and 3.12 are their corresponding longitudinal profiles; similar figures for the remaining FDLs are presented in Appendix B. Positive elevation change signifies mass accumulation and negative elevation change indicates mass wasting. To eliminate error due to the accuracy limitation of both LiDAR datasets, a minimum level of detection was determined for the DoD using propagation of errors. At the 99.7% confidence interval, elevation change greater than ±23.7cm was considered true. The DoD then was masked to exclude any change values less than 23.7cm. The masked DoD was used to calculate the net volume change from 2011 to 2015, reported in Table 3.6. Because the 2011 LiDAR did not cover the entire AOI, the full extents of FDL-7 and FDL-5 are not included in the DoD. The lack of complete coverage for these two FDLs likely caused error in the net volume calculations. All of the FDLs except FDL-11 and -7 demonstrated a negative volume balance, indicating that more material eroded from each FDL area than accumulated. FDL-D, the fastest moving FDL, also had the greatest volume change. This suggests that FDL-D is currently the least stable FDL, as it has lost a large amount of mass through melting of newly-exposed massive ice, the transportation of material in debris flows, and the erosion of sediment by drainage streams.

Large geomorphological features including tension cracks and retrogressive thaw slumps (RTS) were identified in both LiDAR datasets. The head scarps of multiple RTS show clear regression and expansion. The locations of the 2015 head scarps and cracks visible in the LiDAR were verified in the field.

Within the AOI, catchments exist that do not support FDLs; instead alluvial fans have formed from the outflow from these areas. These catchments are termed NDLs, for non-debris lobe. Some of these catchments are immediately adjacent to catchments with FDLs, which raises the question why FDLs form in some areas and not others. To begin to answer this question, these catchment extents and their alluvial fans were delineated in a GIS environment, and their areas and slope angles were quantified.

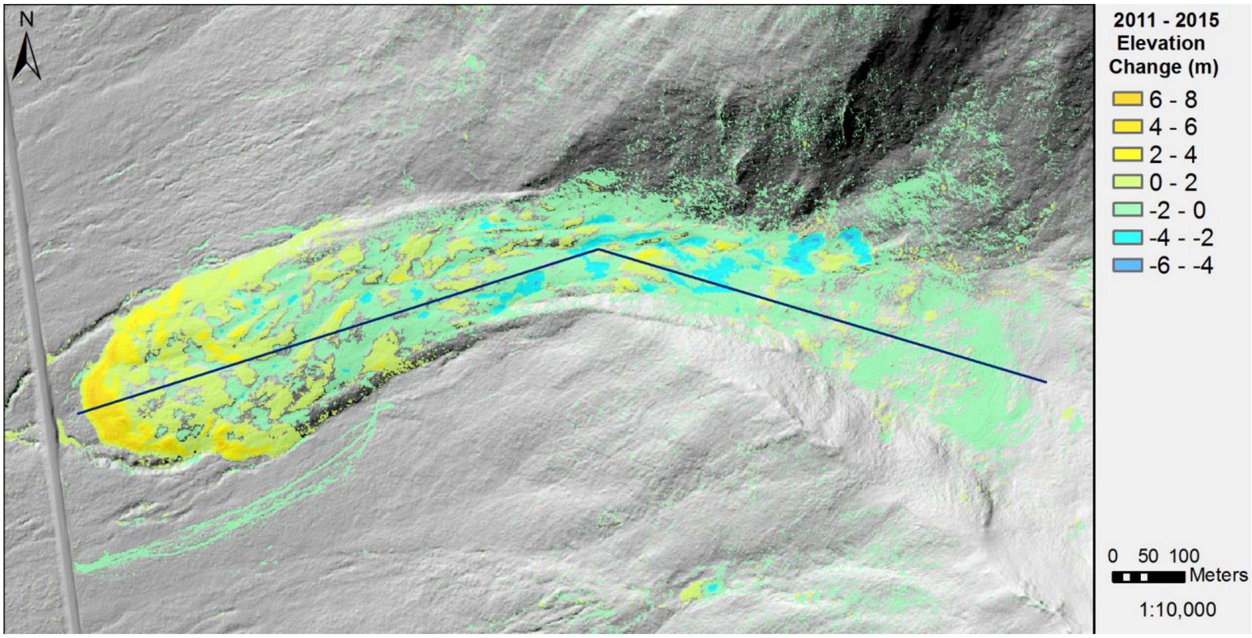

Figure 3.9. DEM of Difference (DoD) for FDL-A, illustrating magnitude of vertical displacement from 2011 to 2015. Dark blue line indicates location of the profile in Figure 3.10.

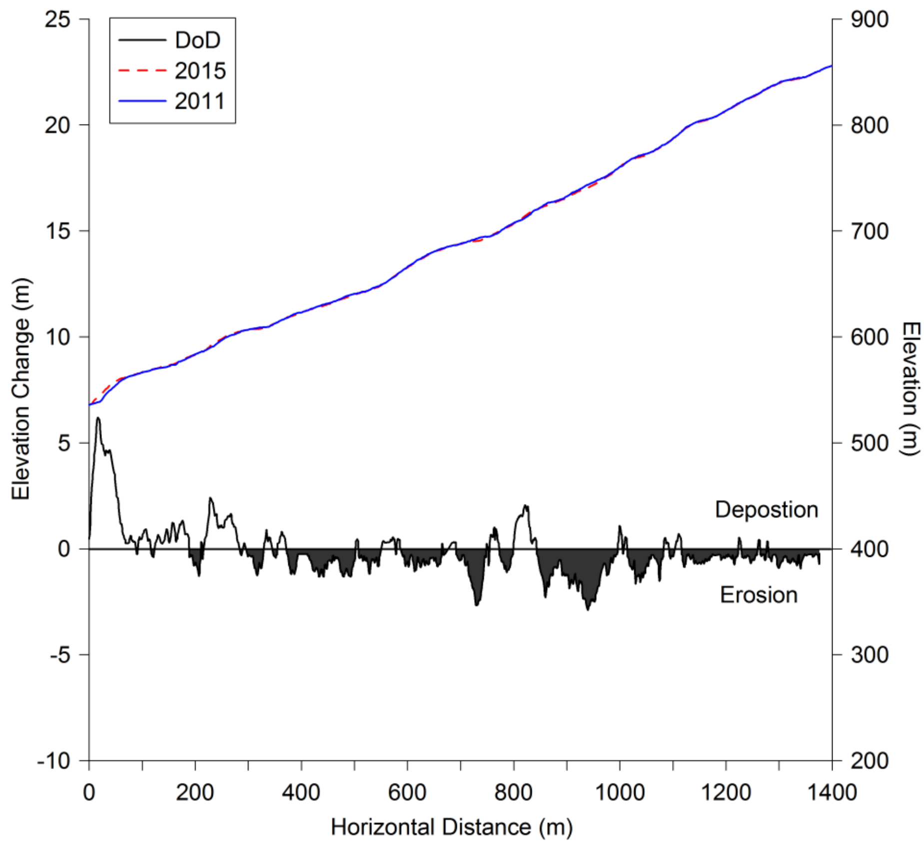

Figure 3.10. Longitudinal profile of FDL-A with a 2:1 vertical exaggeration (blue and red-dashed curves). Change in elevation is illustrated below the longitudinal profile.

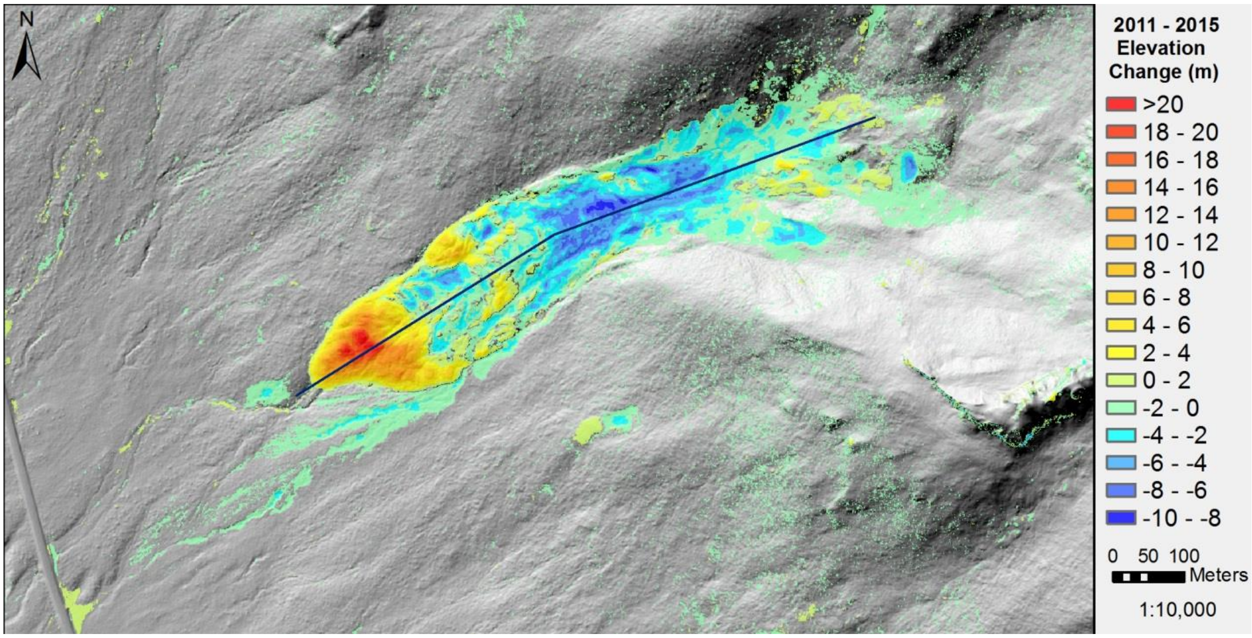

Figure 3.11. DoD for FDL-D, illustrating magnitude of vertical displacement from 2011 to 2015. Dark blue line indicates location of the profile in Figure 3.12.

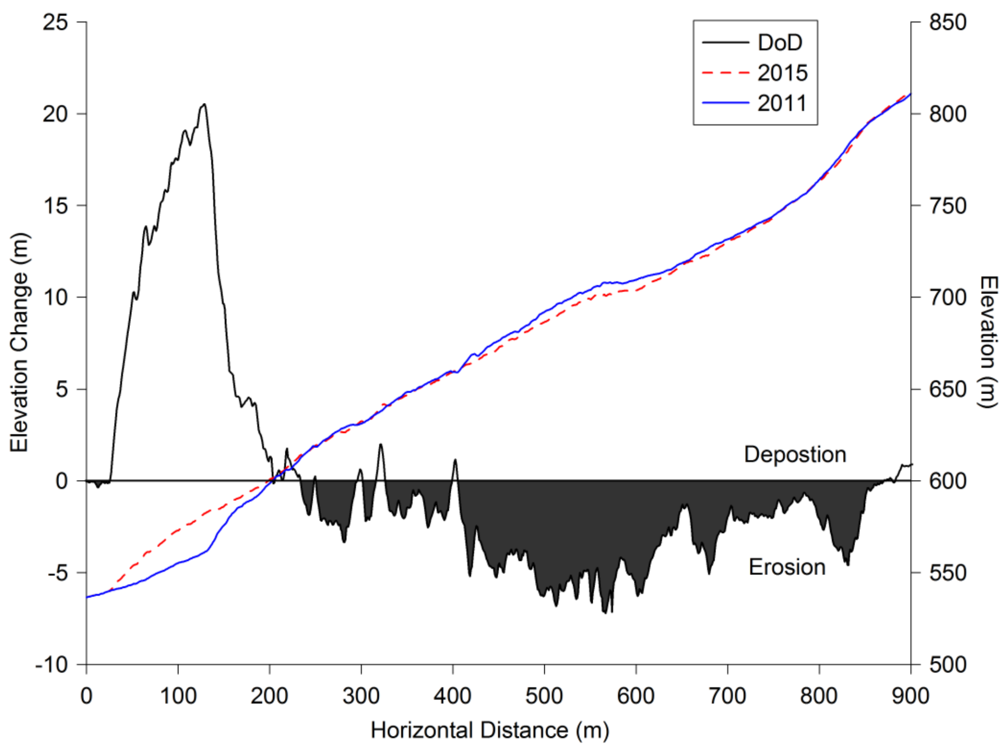

Figure 3.12. Longitudinal profile of FDL-D with a 2:1 vertical exaggeration (blue and red-dashed curves). Change in elevation is illustrated below the longitudinal profile.

Table 3.6. Net volume change from 2011 to 2015 for all eight FDLs (listed from north to south within the AOI).

FDL	Lobe area (m^2)	Net volume change (m^3)	Average elevation change (m)
FDL-11	82,895	2,301	0.03
FDL-7	192,028	759	0.00
FDL-B	91,104	-5,551	-0.06
FDL-A	290,871	-17,990	-0.06
FDL-C	210,375	-13,258	-0.06
FDL-D	159,316	-32,843	-0.21
FDL-5	94,184	-5,240	-0.06
FDL-4	100,482	-6,204	-0.06

Figure 3.13 is an example of an NDL and adjacent FDL. The image contains the outline of the alluvial fan produced from the NDL, the outline of the existing FDL, and the slope angle distribution of each corresponding catchment. A preliminary visual inspection indicates the NDL catchment areas are typically larger than the adjacent FDL catchments. Additionally, each NDL catchment has a greater percentage of steeper slopes than the neighboring FDL catchment. This rough assessment is reinforced with tabulated values for catchment area and slope distribution (see Tables 3.7 and 3.8, and Figure 3.14). Appendix C contains the remaining slope maps, and maps illustrating the aspect distributions of the four NDLs and adjacent FDL catchments.

3.2.3 Seasonal scale: InSAR techniques

Interferometric Synthetic Aperture Radar (InSAR) techniques are recognized as a promising tool for measuring ground deformation with centimeter to millimeter accuracy. Since the 1990s, InSAR techniques have been applied successfully to study a wide range of natural and anthropogenic hazards including earthquakes, hydrological subsidence, and landslides. For this part of the project, the application of InSAR techniques to the study of FDLs was investigated.

The specific goals of this analysis were: (1) to determine the performance of a range of space borne SAR data for the observation of FDLs using InSAR; and (2) to apply SAR data from selected sensors to characterize the deformation behavior of the investigated FDLs within the AOI. To analyze the full spectrum of available SAR data, both medium-resolution historic SAR images as well as high-resolution imagery from the currently-flying TerraSAR-X sensor were included.

3.2.3.1 *Analysis of Historic SAR Data for the Study of FDLs*

The research team examined SAR images from medium-resolution satellite SAR missions that were available through the services of the Alaska Satellite Facility (ASF) at UAF. This included imagery from the Phased Array type L-band Synthetic Aperture Radar (PALSAR) and European Remote Sensing satellites 1/2 (ERS1/2). Conventional small baseline differential interferometric InSAR techniques were applied to extract FDL motion from pairs of images.

The first problem to be addressed was identifying the most appropriate data configurations (i.e., sensor wavelength and temporal separation between images used for InSAR processing) for FDL analysis. To choose the most appropriate data, the ground coverage of northern Alaska was considered, as well as the typical downslope velocity of specific FDLs as measured on the ground (described in Section 3.1). The climate conditions of the study area lead to severe ground coverage changes throughout the year, limiting the temporal baseline, B_t (time separation of InSAR partners), that can be used for InSAR processing. A second constraint for B_t comes from the motion of the observed FDLs. Too short of a B_t will limit the amount of surface motion that occurs between the acquisition times of the InSAR data and results in too little phase signal in processed interferograms. If B_t is too long, the motion will be too strong, leading to decorrelation of the InSAR signal. Both parameters also are dependent on the wavelength used by the sensor.

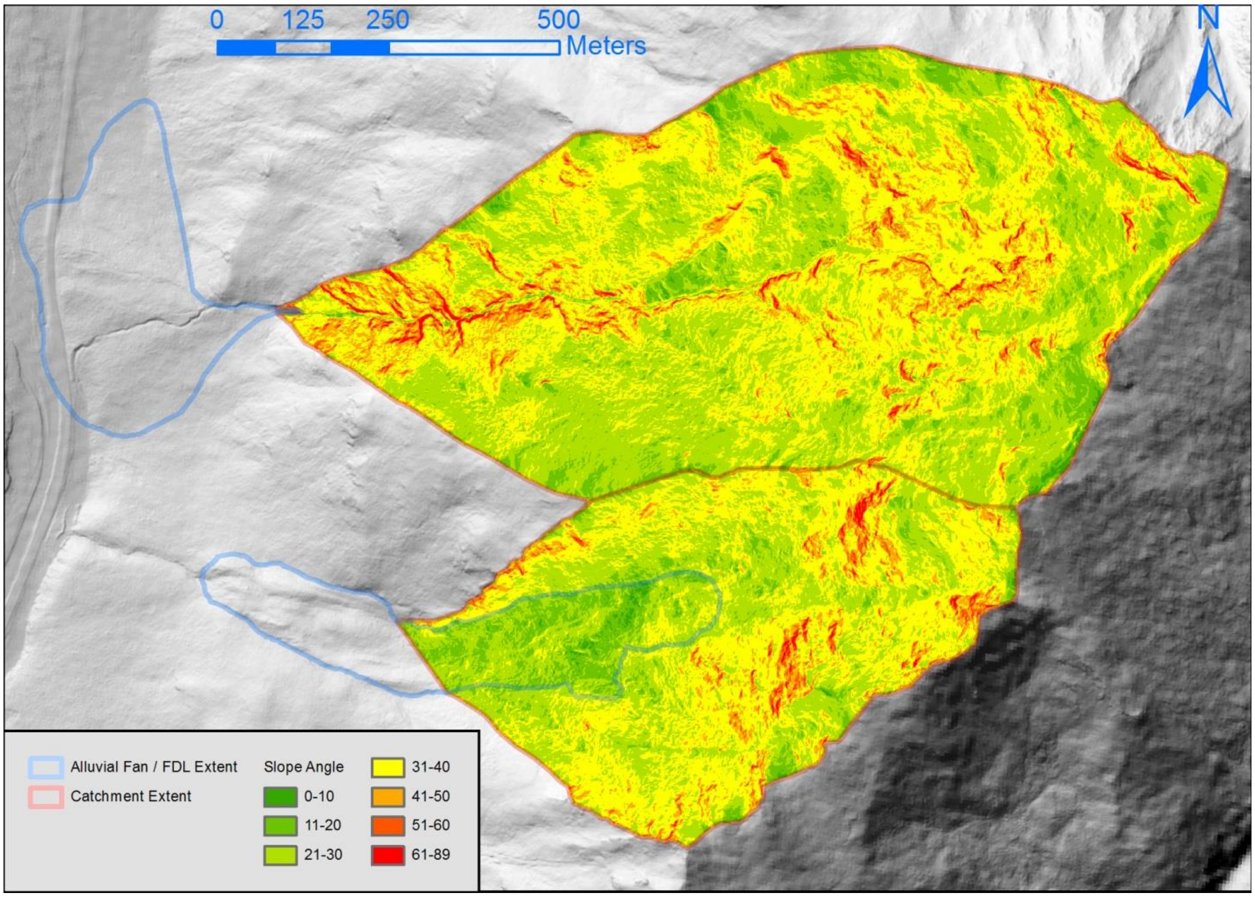

Figure 3.13. Slope angle distributions of NDL-1 and FDL-11 catchments.

Table 3.7. Summary of FDL and NDL catchment areas.

FDL	Catchment area (m^2)	NDL	Catchment area (m^2)
FDL-11	308,081	NDL-1	600,995
FDL-A	937,691	NDL-2	3,001,443
FDL-D	692,298	NDL-3	495,446
FDL-2	627,554	NDL-4	3,557,226

Table 3.8. Summary of FDL and NDL catchment slope angle distributions.

	Percentage (%)							
Slope (°)	FDL-11	FDL-A	FDL-D	FDL-2	NDL-1	NDL-2	NDL-3	NDL-4
0 - 10	0.71	1.95	2.27	0.93	0.49	0.40	0.54	1.97
10 - 20	9.91	21.96	28.23	9.39	7.15	8.01	7.09	27.06
20 - 30	38.83	47.28	49.42	33.80	40.05	34.07	27.75	41.59
30 - 40	40.75	23.37	16.71	47.33	39.65	46.30	52.44	24.93
40 – 50	7.07	3.16	2.51	7.76	9.28	7.85	10.10	4.04
50 – 60	2.18	1.64	0.60	0.67	2.57	1.60	1.47	0.32
60 – 89	0.55	0.64	0.25	0.13	0.80	1.75	0.60	0.09

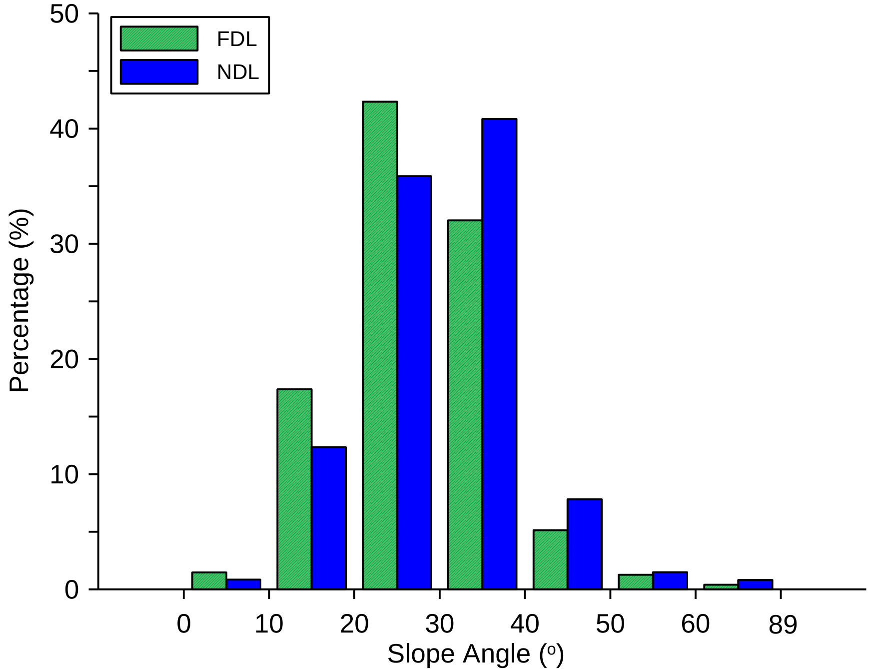

Figure 3.14. Comparison of slope angle distributions for FDL and NDL catchments.

To identify optimal observation configurations, coherence maps over three FDLs (FDL-A, -B, and -C) with different wavelengths and temporal baseline configurations were studied. Examples of these maps are shown in Figure 3.15, overlain on Google Earth optical images acquired in April 2010, when the AOI was snow-covered. C-band data with a temporal baseline of 1 day (B_t = 1 day) obtained coherence almost everywhere (Figure 3.15b), but part of FDL-A and FDL-B decorrelated likely due to their fast motions. In Figures 3.15c and 3.15d, the decorrelation is becoming more severe for interferograms with longer temporal baselines (for Figure 3.15c, B_t = 46 days, and for Figure 3.15d, B_t = 92 days). Thus, to maintain sufficient coherence for SAR interferometry, 13 ERS tandem pairs with B_t = 1 day and nine PALSAR pairs with B_t = 46 days (i.e., one satellite repeat cycle) were selected and processed to reconstruct the motion field of FDLs. Another benefit of using interferograms with a short temporal baseline is that the difficulties in phase unwrapping caused by the excessive motion of FDLs also can be reduced. Table 3.9 is a summary of the differential interferograms with sufficient coherence that we analyzed for this project. Eight PALSAR interferograms and two ERS tandem pairs from ascending tracks were used, as well as one PALSAR and ten ERS interferograms from descending tracks. The DEM derived from the 2001 airborne IfSAR was used to generate differential interferograms (through removal of the topographic signal). The DEM has a 5m posting with a vertical accuracy of 3m over 0-10° slopes (GINA 2001). Additionally, the DGPS measurements from Section 3.1 were used to assist with the InSAR results analysis. As the InSAR and DGPS data do not cover the same time spans, they are used together to understand the long-term behavior of FDLs and changes from year to year.

The unwrapped differential interferometric phase (d-InSAR) ($\phi_{p,i}$) at every pixel *p* in an interferogram *i* was used to estimate FDL motion. This d-InSAR phase can be written as (Hanssen, 2001):

$$\phi_{p,i} = \phi_{p,i,\Delta topo} + \phi_{p,i,defo} + \phi_{p,i,orbit} + \phi_{p,i,atm} + \phi_{p,i,noise} \tag{1}$$

In Eq. 1, $\phi_{p,i,defo}$ is the signal of interest, measuring the projection of the FDL motion vector into the satellite's line-of-sight direction. In addition to this target signal, the original d-InSAR measurement contains other parameters such as: $\phi_{p,i,\Delta topo}$, which is the phase contribution caused by inaccuracy of the InSAR DEM used for topographic correction; a phase introduced by inaccuracies in the satellite orbits ($\phi_{p,i,orbit}$); atmospheric delay differences between two image acquisition times ($\phi_{p,i,atm}$); and noise ($\phi_{p,i,noise}$).

Based on the field measurements, the research team expected excessive deformation for the observed FDLs, making $\phi_{p,i,defo}$ the dominant contribution to $\phi_{p,i}$. The $\phi_{p,i,\Delta topo}$ parameter was minimized by selecting interferograms with small perpendicular baselines (<230m for ERS and <860m for PALSAR). As only the deformation of FDLs is of interest and they have small spatial extents, the typically large-scale phase ramp related to $\phi_{p,i,orbit}$ and $\phi_{p,i,atm}$ was largely removed by subtracting planar trends from $\phi_{p,i}$. Residual impacts of $\phi_{p,i,atm}$ were reduced by setting up a proper spatial reference point close to the targeted FDLs. As only high-coherence interferograms were used in this study, $\phi_{p,i,noise}$ was considered to be small. The interferometric phases were unwrapped using the minimum cost flow (MCF) approach, and

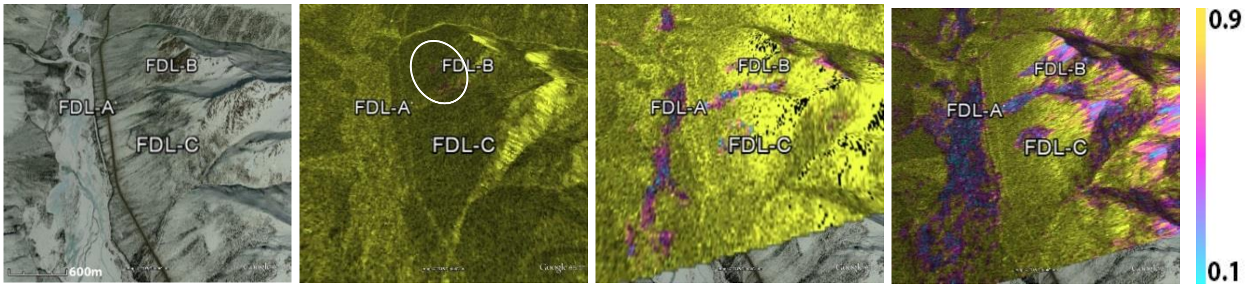

(a) (b) (c) (d)

Figure 3.15. Demonstration of coherence change over FDLs with different radar wavelength and temporal baseline. (a) Ground coverage of FDL-A, -B, and –C in April 2014 (from Google Earth); (b) ERS1/2 tandem pair (1995-10-20 to 1995-10-21); (c) PALSAR 46-day pair (2008-10-24 to 2008-12-09); and (d) PALSAR 92-day pair (2007-10-22 to 2008-01-22). All coherence maps are overlaid on the Google Earth optical image (the scale is noted in (a)). The white circle in (b) outlines the low coherence region near FDL-A and –B.

Table 3.9. Overview of interferogram (IFG) pairs used in quantitative analysis. The heading angle is the approximation of the average value of the corresponding interferogram pairs.

Sensor	No. of IFGs	Baseline range (m)	Year range	Time interval (days)	Pass	Path No.	Heading angle	FDLs
PALSAR	8	-385 – 858	2006 – 2011	46	Ascending	P255	-12°	7, B, A, C
	1	520	2007	46	Descending	P262	-163°	
ERS1/2	2	-70 – 142	1995 – 1996	1	Ascending	P407	-18°	7
	11	-90 – 229	1995 - 1996	1	Descending	P43 P315 P272	-162°	11, B, A, C, D, 5, 4

resulting unwrapped interferograms were checked manually for unwrapping errors, especially for the regions covering the targeted FDLs.

As InSAR is only sensitive to the projection of surface motion into the sensor's line-of-sight, assumptions were needed to derive the three-dimensional (3D) FDL motion vector from the originally one-dimensional InSAR observations. In this study it is assumed that FDL motion is surface parallel. Hence, the measured InSAR signal was projected into the direction of maximum surface gradient using a DEM to derive the true direction and magnitude of FDL motion.

Identifying and outlining active FDLs using PALSAR interferograms: InSAR is a good tool for identifying active slope motion, especially in remote areas such as Northern Alaska. The benefit of using L-band data is related to their longer wavelength (23cm) compared to C-band data (5.6cm), leading to deeper penetration into snow-covered surfaces and improved coherence conditions. PALSAR data also have a longer temporal baseline (46 days), resulting in larger displacements as compared to ERS tandem pairs, which helps in the identification of active regions.

Figure 3.16 contains segments of an InSAR frame covering areas from north to south along the Dalton Highway. Several moving features can be identified along the adjacent slopes, distinguished by their dense (colorful) fringe patterns in contrast to the more homogeneous background. Larger FDLs are highlighted with white arrows in Figure 3.16. A group of smaller FDLs on the west side of the Dalton Highway (not included in this study) is highlighted by a white circle in Figure 3.16b. Other small FDLs are circled in Figure 3.16c. Phase errors in areas with steep topography are masked out in Figure 3.16 and appear as white areas. Also, fringe patterns are present along the Dietrich River (indicated by a dashed line). These are thought to be due to winter aufeis along the riverbed, an example of which is outlined by a white rectangular box in Figure 3.16b. This demonstrates the multifaceted capability of InSAR analysis of Arctic environments.

Heterogeneous deformation inside FDLs: Field DGPS data suggest that the speed with which an FDL moves downslope varies significantly throughout the FDL body. InSAR maps can provide a wealth of information on the spatial patterns of motion within an FDL. For this purpose, medium-resolution SAR images from the PALSAR and ERS sensors were used and demonstrated sufficient performance to identify spatial patterns within the investigated FDLs. Due to geometry effects in the side-looking satellite data, FDLs on the east side of the valley were studied using images acquired in the descending orbit direction, while FDL-7 on the west side of the valley required ascending frames. Thus, two descending tandem pairs, one acquired on 1995-10-04 and 1995-10-05 and another one on 1996-02-20 and 1996-02-21, were selected for FDLs located on the east side of the valley (FDL-A, -B, -C, -D, -4, -5, and -11). Data acquired from 1995-10-14 to 1995-10-15 and 1996-02-12 to 1996-02-13 were selected for FDL-7.

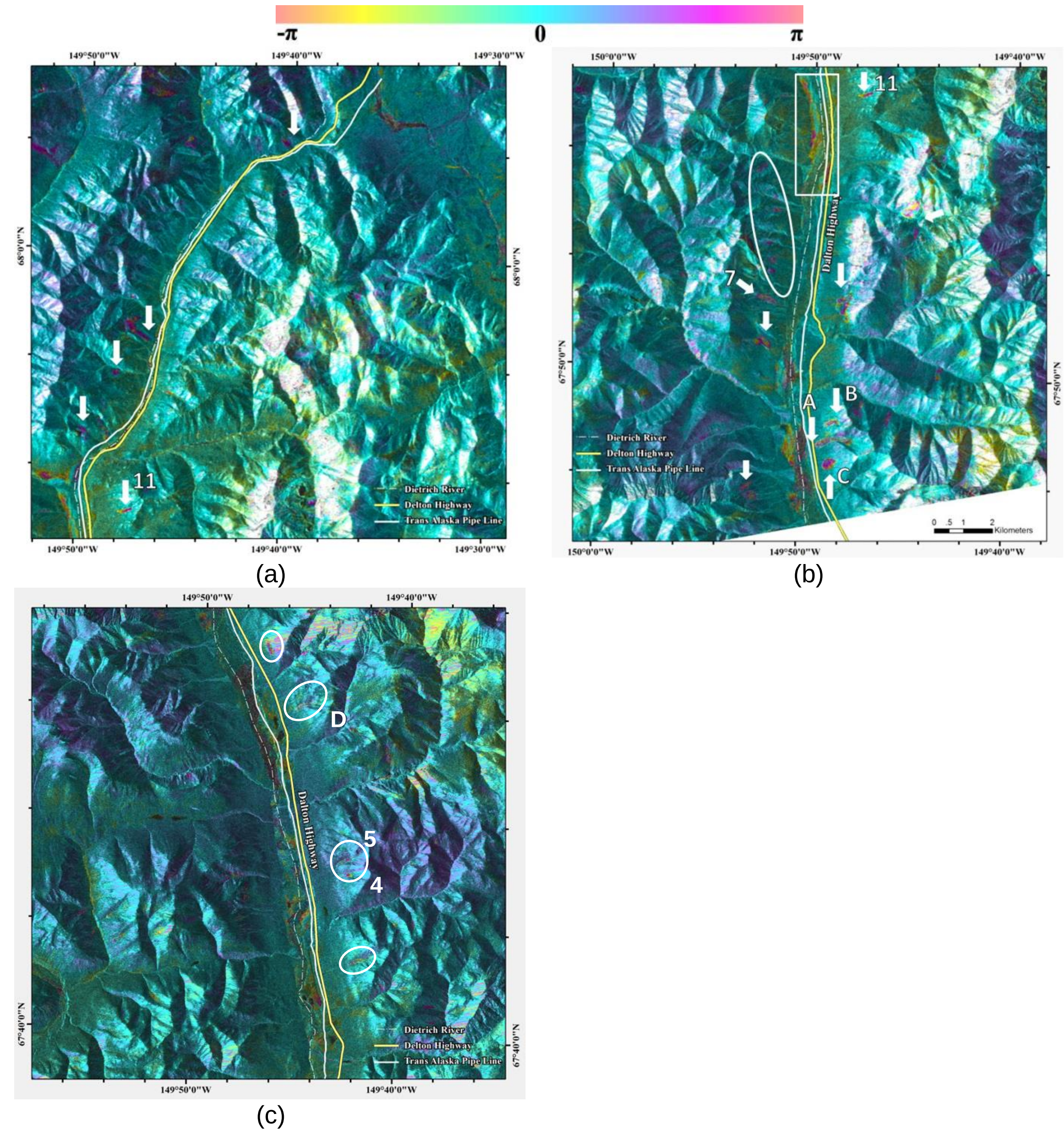

Figure 3.16. PALSAR differential interferograms presented from north to south along the AOI. The images were acquired on 2010-12-15 and 2011-01-30. The targeted FDLs are outlined by circles or are indicated with arrows and their identification. Other active areas also are indicated by arrows. All images share the same scale, as indicated in image (b).

The reconstructed deformation maps from October 1995 and February 1996 are presented in Figures 3.17 and 3.18. Present in each sub-figure, the spatial reference points (red circles) were chosen based on proximity to the Dalton Highway. For FDL-A, -B, and –C, the data indicate that the maximum motion of these FDLs occurred in October 1995 (Figure 3.17a), and the largest displacement was near the toe of FDL-B with a motion of 52 mm/day. At the same time, the maximum displacement on the surface of FDL-A was approximately 27.5 mm/day and located near its center. The displacement of FDL-C was much smaller than its neighbors, with a maximum value of about 11 mm/day. Figure 3.17b demonstrates the one-day motion of the same region in early February 1996. The size of the deforming area on FDL-B shrank significantly, and its maximum displacement dropped to about 3 mm/day. The movement rate and the size of deformation in the upper part of FDL-A decreased, while FDL-A's toe remained relatively active with a maximum observed displacement of about 7 mm/day. The movement of FDL-C was still ongoing in February with a rate similar to that of FDL-B. The maximum deformation of FDL-C was approximately 2.8 mm/day.

The resulting displacement fields for FDL-D are shown in Figures 3.17c and 3.17d. Again, higher velocities occurred in October near the upper part of the lobe, amounting to 37 mm/day. As with FDL-A, -B, and -C, the deformation rate decreased in February with a maximum observed displacement of 4.7 mm/day. In contrast, the displacements of FDL-4 and -5 were much smaller than those previously discussed, being near the noise level (Figures 3.17e and 3.17f). Nevertheless, the deforming areas of FDL-4 and -5 can be isolated from the background, with displacements in the range of 7-15 mm/day in October and 3-6 mm/day in February.

Figures 3.18a and 3.18b contain the displacement field data for FDL-11. For the October displacement field, the maximum displacement measured for FDL-11 was approximately 13 mm/day, which was similar to FDL-4 and -5 (Figure 3.17e). The portion of FDL-11 that was moving was smaller than the other lobes. It is also noteworthy that no deformation was present on FDL-11 in February 1996.

Finally, the motion maps for FDL-7 are presented in Figures 3.18c and 3.18d, which indicate a strong deformation gradient especially in October 1995. The maximum displacement of FDL-7 was located near its toe with a value of ~46 mm/day. The motion pattern changed significantly in February 1996, where the inner part of the lobe demonstrated the strongest motion with a maximum observed displacement of ~15.3 mm/day. It must be stressed that these values were derived by converting the satellite's line-of-sight direction into the downslope motion, potentially resulting in inaccuracy in the absolute movement rates. Relative rates of deformation produced from this analysis, however, are valid. Overall, this analysis indicates that the <u>FDLs experience substantial seasonal spatial variation in their internal deformation rates</u>.

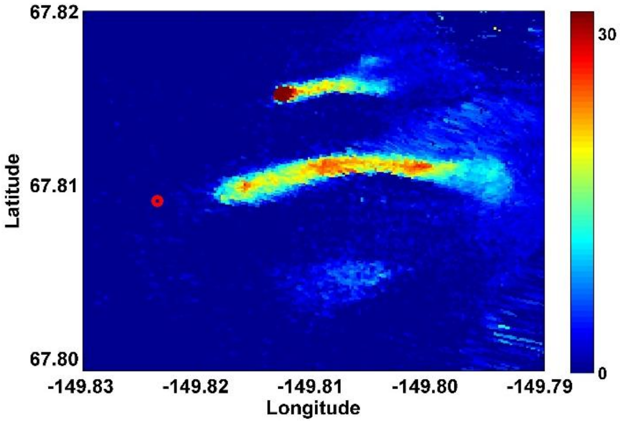

(a) FDL-B, -A, -C (1995-10-04 to 1995-10-05)

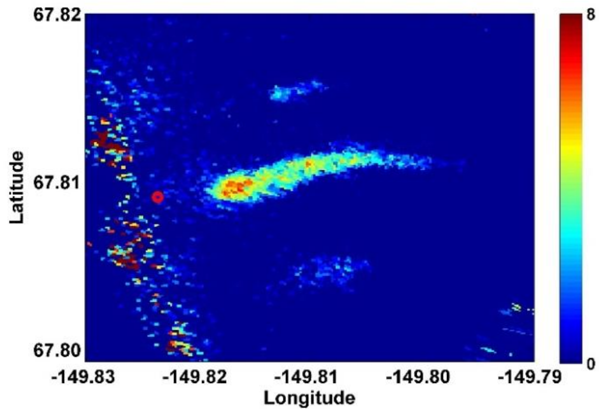

(b) FDL-B, -A, -C (1996-02-20 to 1996-02-21)

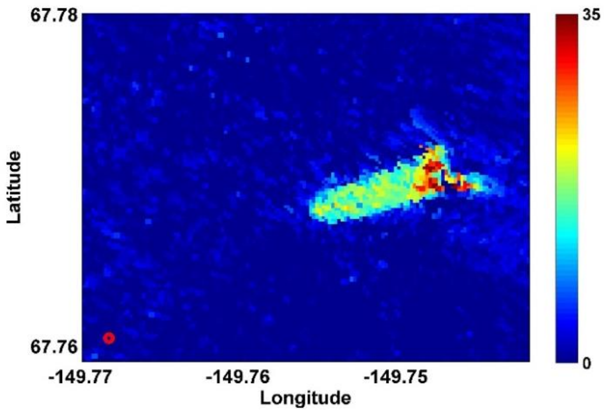

(c) FDL-D (1995-10-04 to 1995-10-05)

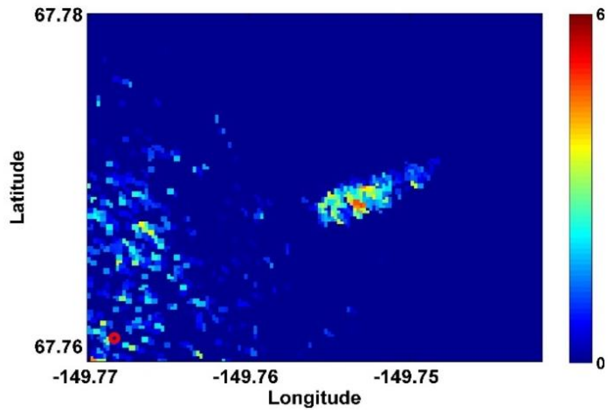

(d) FDL-D (1996-02-20 to 1996-02-21)

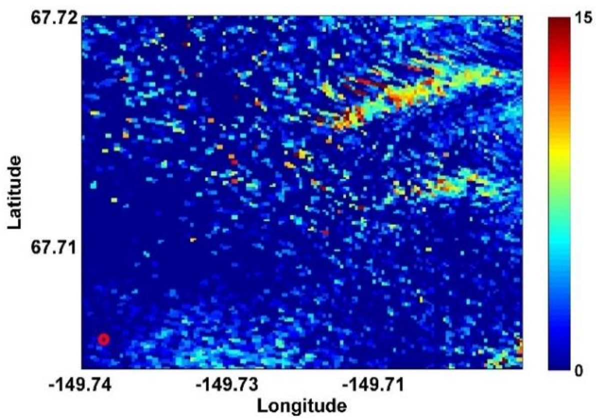

(e) FDL-5, -4 (1995-10-04 to 1995-10-05)

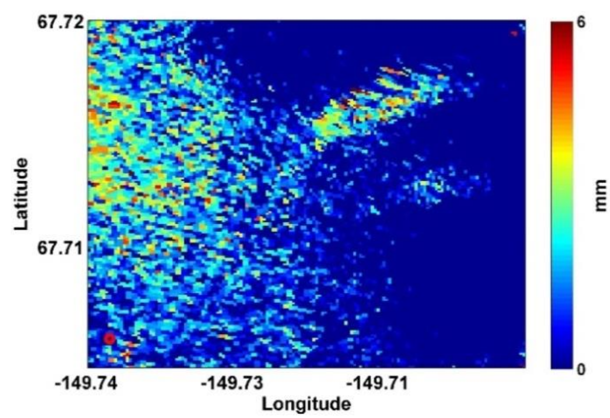

(f) FDL-5, -4 (1996-02-20 to 1996-02-21)

Figure 3.17. Deformation field in the downslope direction reconstructed from tandem pairs for FDL-B, -A, -C (a and b), FDL-D (c and d), and FDL-5 and -4 (e and f). The time periods are as indicated in each sub-figure title.

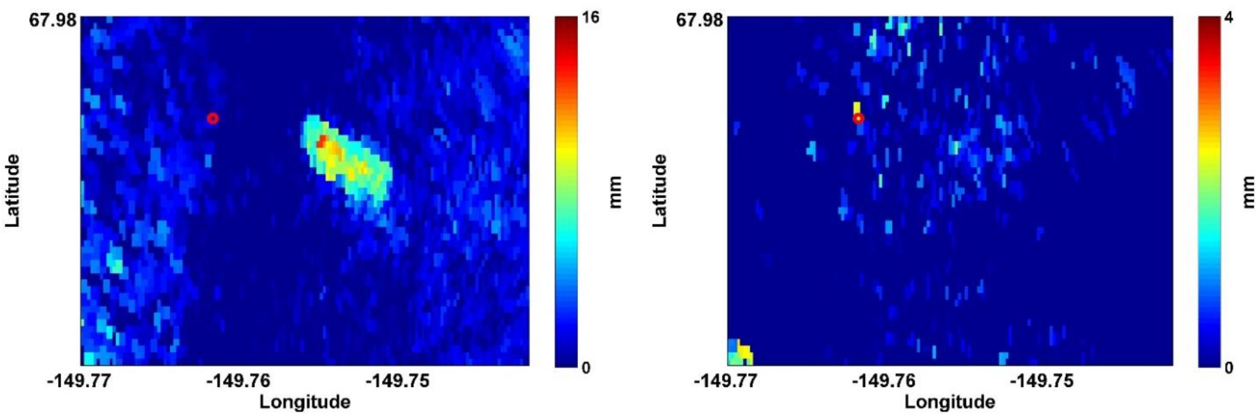

(a) FDL-11 (1995-10-04 to 1995-10-05)

(b) FDL-11 (1996-02-20 to 1996-02-21)

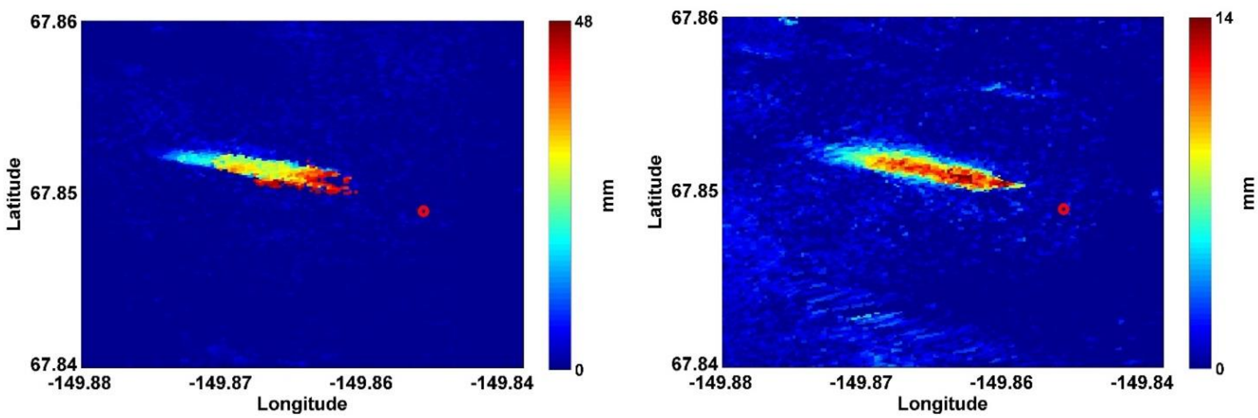

(c) FDL-7 (1995-10-14 to 1995-10-15)

(d) FDL-7 (1996-02-12 to 1996-02-13)

Figure 3.18. Deformation field in the downslope direction reconstructed from tandem pairs for FDL-11 (a and b), and FDL-7 (c and d). The time periods are as indicated in each sub-figure title.

<u>*Seasonal variation of FDL velocity*</u>: To analyze changes in FDL motion throughout a winter season, a set of ten ERS tandem pairs acquired in descending orbit direction were analyzed. Table 3.10 contains a summary of the data used. FDL-7 was excluded from this study because there were not enough ascending interferograms covering its area. Overall, the time span of this study was from October 1995 to May 1996.

To analyze seasonal change and also to facilitate a comparison of estimated rates to reference information, phase values at ground control points (GCPs) were extracted from each interferogram and the extracted information was used for time series analysis. Figure 3.19 contains an example of the averaged and geocoded radar intensity image and the distribution of extracted data points (shown as red crosses in Figure 3.19b). Note that the DGPS measurements at these GCPs were collected beginning in 2012 for FDL-A and in 2013 for the other investigated FDLs, while the ERS-based InSAR measurements stem from the winter of 1995/96. Hence, some of the GCPs were not located on the main moving body in 1995 – especially those located near the current toe positions – and were not included in the analysis. Despite the difference in time between the InSAR and DGPS data, the benefit of using the same GCPs is to record deformation conditions at consistent locations. Additionally, some points indicate negative displacement. This is most likely due to offset of the ground reference point for that set of measurements.

Time series information was extracted for all GCP locations for FDL-A and FDL-B; examples are included in Figures 3.20 and 3.21, respectively. The time series for all GCPs suggest that FDL-A moves fastest in early October followed by a drop of motion rates with a minimum around the late February / early March time frame (Figure 3.20). The temporal change in motion of FDL-B is similar to that of FDL-A. Its motion decreased from October 1995 until reaching a minimum in February 1996, followed by a recovery of motion until the last dataset in May 1996.

For the remaining FDLs, only the time series of the average displacement are presented (Figure 3.22). This is because either the individual FDLs are too small or their deformation rates are too slow, leading to substantial noise in the raw estimates. The averaged deformation time series for these lobes are similar to those measured at FDL-A and -B, as the minimum displacement occurred in late February of 1996. Similarly, the maximum deformation observed occurred in October of the analyzed year; however, given there are no measurements for the period between June and September, it cannot be concluded from the InSAR data alone that October corresponds to the annual motion maximum.

3.2.3.2 *Analysis of Modern High-Resolution TerraSAR-X SAR Data for FDL Analysis*

Finally, as part of this research, the research team proposed to analyze newly acquired data from Sentinel-1. The Sentinel-1A (S1A) satellite, which is a C-band sensor, was launched on April 3, 2014, and started its operational running in October 2014. In order to use InSAR techniques on S1A data, this data must be in interferometry wide-swath (IW) mode and single-look-complex (SLC) format. The primary distribution of S1A data is conducted by the European Space Agency (ESA), which decides the S1A acquisition plan, mode, and distribution format.

Table 3.10. ERS tandem pairs used for the analysis of FDL motion throughout the 1995-1996 winter season.

Index	Master	Slave	*B*⊥	Frame/Path/Orbit
1	19951004	19951005	229.29	F279/P43/D
2	19951213	19951214	-90.09	F279/P44/D
3	19960221	19960222	141.59	F279/P45/D
4	19960327	19960328	-69.78	F279/P46/D
5	19960501	19960502	-39.56	F279/P47/D
6	19951023	19951024	83.73	F279/P315/D
7	19951127	19951128	53.81	F279/P316/D
8	19960101	19960102	-77.15	F279/P317/D
9	19951020	19951021	61.98	F279/P272/D
10	19951124	19951125	151.65	F279/P273/D
11	19951229	19951230	-112.14	F279/P274/D
12	19951014	19951015	-135.838	F171/P407/A
13	19960212	19960213	139.6354	F171/P407/A

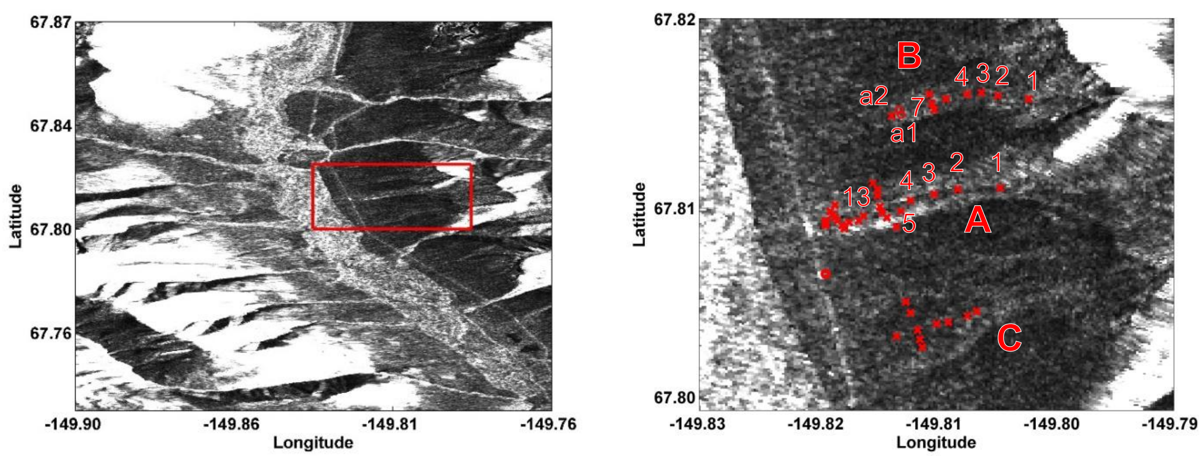

Figure 3.19. General location of FDL-A, -B, and –C (a) and locations of corresponding GCPs (b). In (b), two points (a1 and a2; denoted by red circles) were added to FDL-B to demonstrate the region where it moved the fastest. The gray background image is the averaged and geocoded radar intensity image. The bright surfaces indicate areas impacted by radar geometry errors.

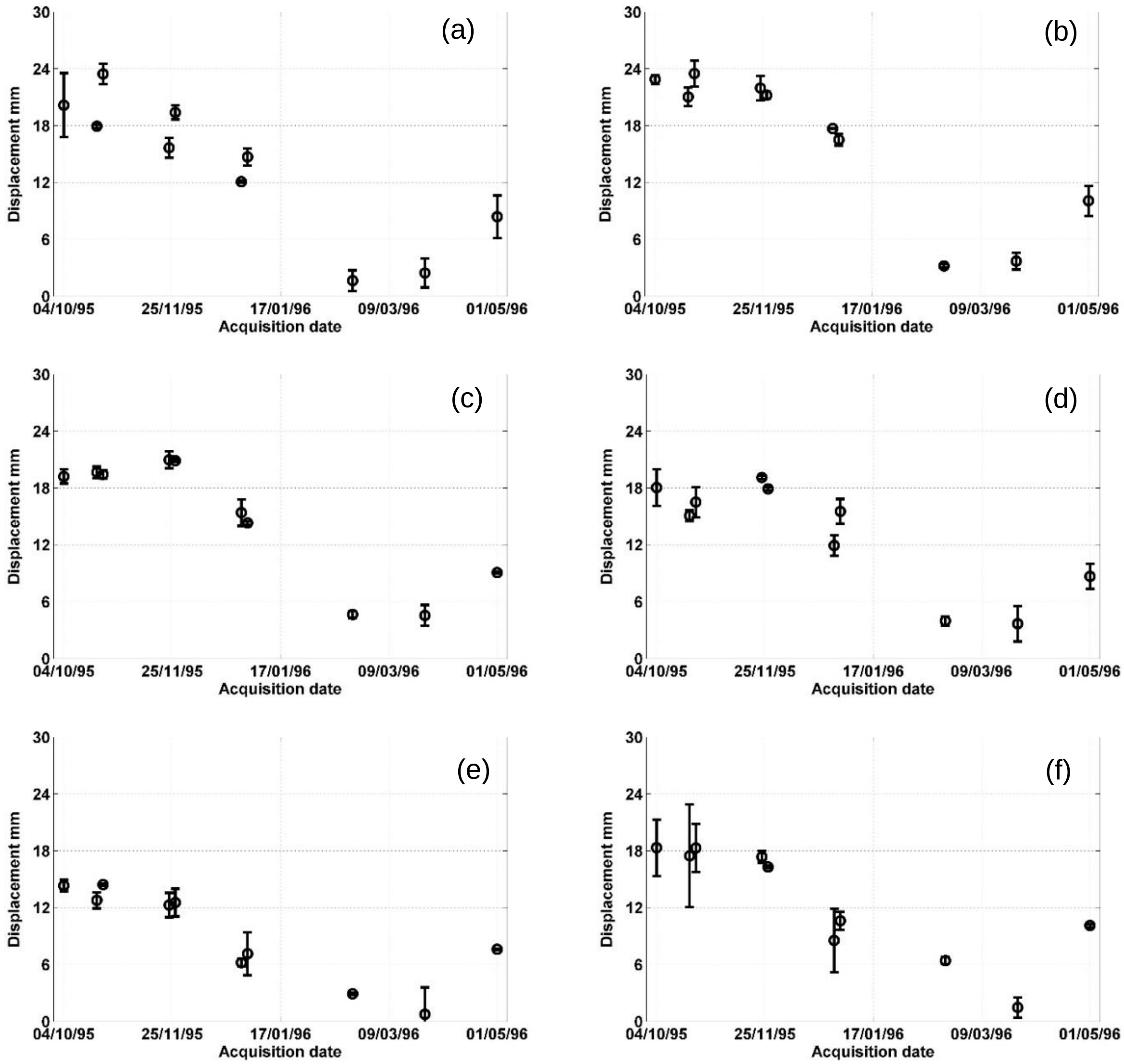

Figure 3.20. Deformation time series of GCPs for FDL-A from the period of October 1995 to May 1996. The corresponding GCPs are as follows: (a) 1, (b) 2, (c) 3, (d) 4, (e) 5, and (f) 13.

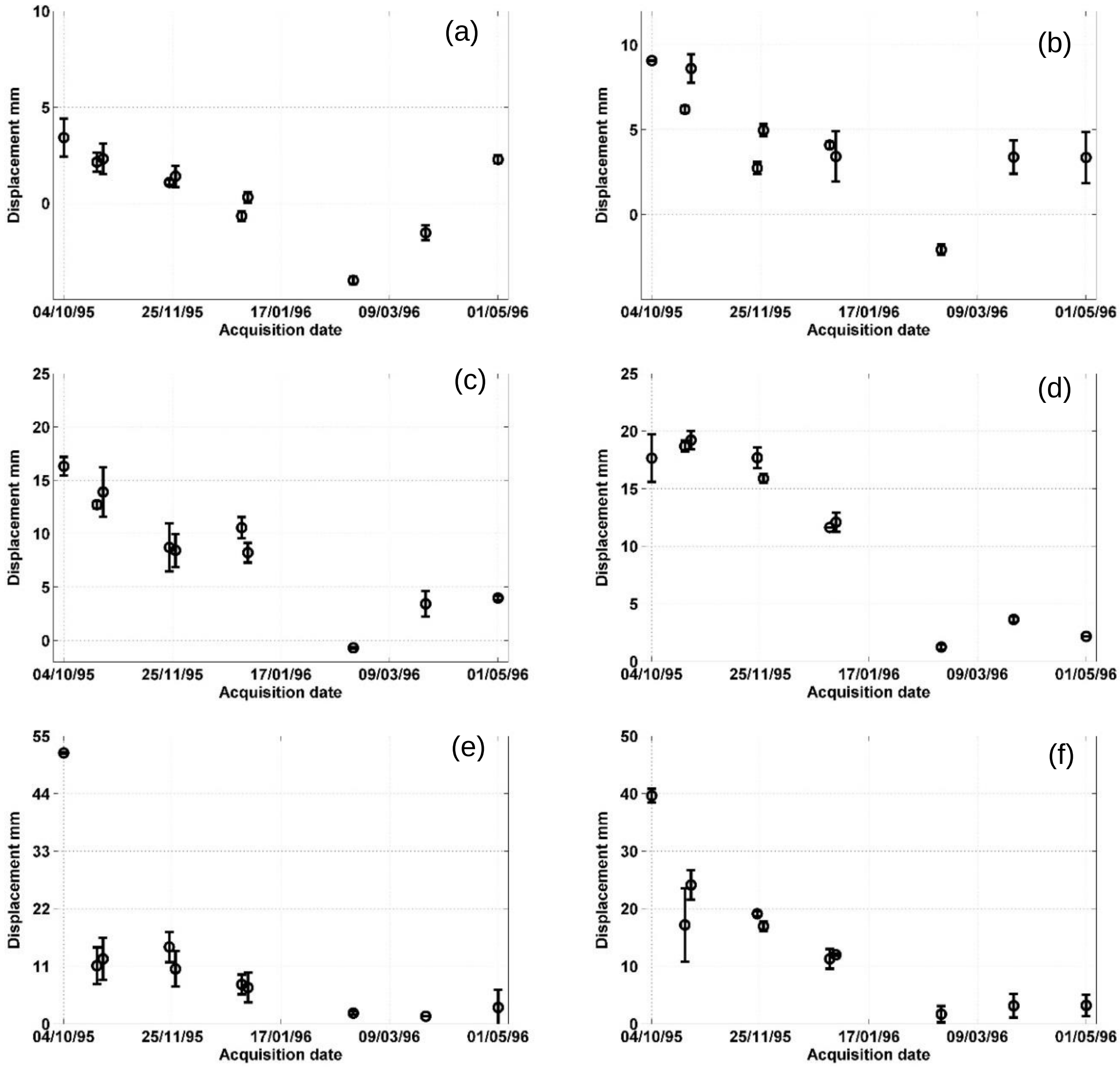

Figure 3.21. Deformation time series of GCPs for FDL-B from the period of October 1995 to May 1996. The corresponding GCPs are as follows: (a) 1, (b) 2, (c) 3, (d) 4, and (e) 7. In (f), two extra points (a1 and a2 in Figure 3.19) located at the toe of FDL-B during the 1995-96 winter were added; they were used to demonstrate displacement where the most deformation occurred on FDL-B.

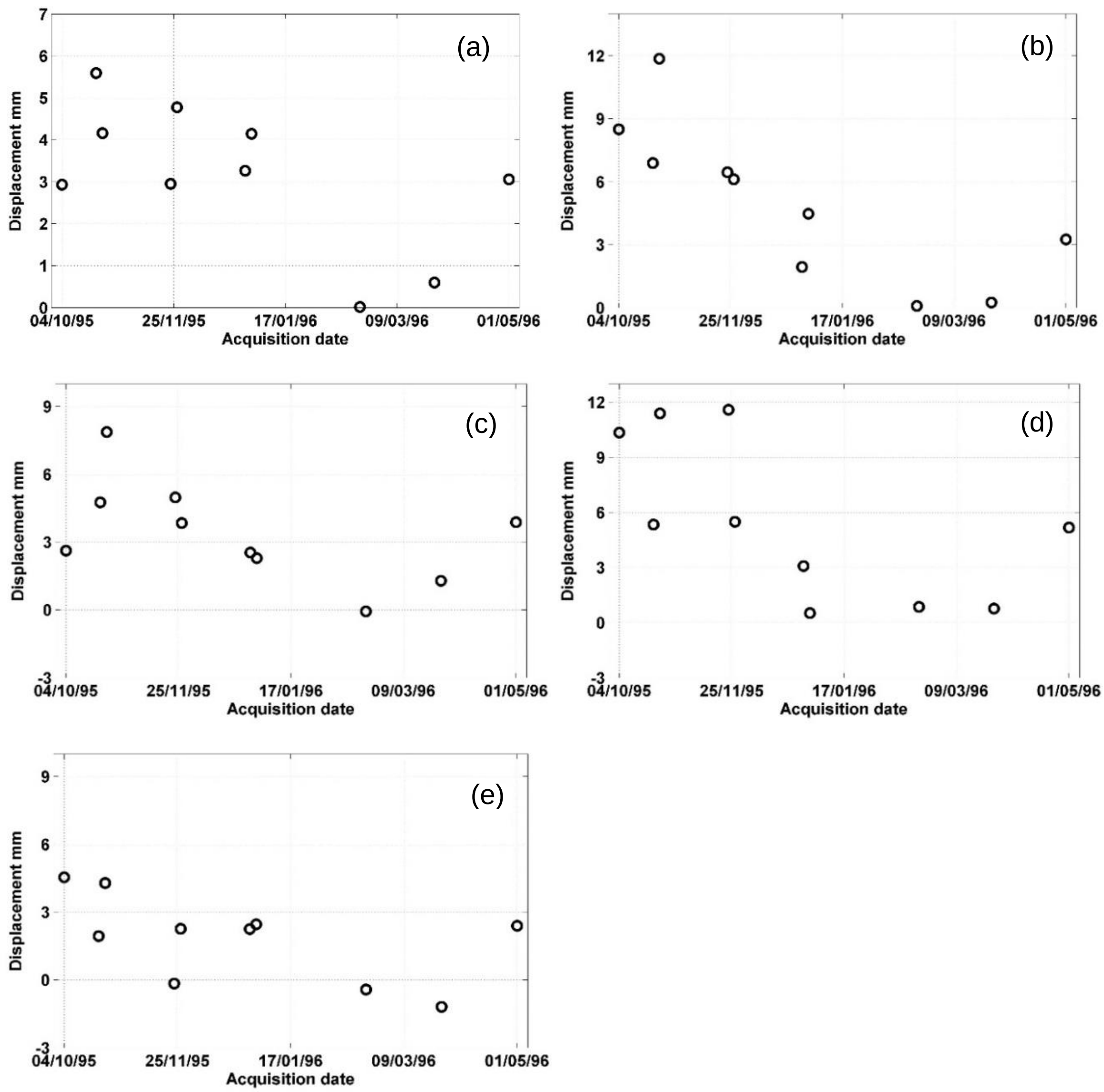

Figure 3.22. Time series of averaged deformation from the period of October 1995 to May 1996 for: (a) FDL-C, (b) FDL-D, (c) FDL-5, (d) FDL-4, and (e) FDL-11.

By mid-2015, ESA had not acquired nor distributed any S1A data that covered our AOI. In late 2015, ESA distributed the first S1A images in IW mode and SLC format covering the AOI. More recently, ESA distributed another three S1A images from the same track over this region, bringing the total to only four images that are potentially useful. As learned from the analysis of the ERS1/2 data, the temporal decorrelation of C-band data over FDLs can occur, especially in the winter with heavy snow cover. Thus, there were concerns about the usefulness of this data for the FDL study. Additionally, the available S1A frames did not fully cover the AOI.

Instead of using the S1A data, an alternate data source was used. Modern SAR data, such as those from the TerraSAR-X (TSX) mission, are an interesting alternative to historic data. Their advantages include higher spatial resolution and shorter revisit times. At the same time, acquisitions are only scheduled on request and data access is not free. Furthermore, the X-band frequency reduces penetration into vegetation canopies, reducing the value of TSX for InSAR analysis on FDLs.

TSX is an X-band radar satellite operated jointly by Airbus, Inc. and the German Aerospace Center (DLR). Its Stripmap-mode product (the one used in this project) has a spatial coverage of 50 × 30 km^2. Its spatial resolution is 3m, which is finer than most other satellite system data analyzed for this project. TSX provides data with a revisit time of 11 days. To access data for this project separate proposals were submitted to DLR to obtain: (1) archived data acquired in the summer of 2013 (free of charge); and (2) new acquisitions programmed in the summer of 2016 (incurring handling fees). The following discussion summarizes the first experimental results with TSX data using both InSAR and offset tracking methods.

InSAR on FDLs with TSX Data: Figures 3.23 and 3.24 include two examples of TSX wrapped differential interferograms, as well as the corresponding coherence maps. These examples include one ascending pair acquired on 2016-06-28 and 2016-07-09 with 24.84m perpendicular baseline, and a descending pair acquired on 2016-07-07 and 2016-07-18 with -69.07m perpendicular baseline. Both of these pairs were selected to minimize seasonal scattering differences as well as spatio-temporal baselines to support coherence conditions.

The coherence maps for both examples (Figures 3.23a and 3.24a) indicate that coherence is maintained at higher altitudes near the tops of hills (yellow colors); however, significant decorrelation can be identified along the valley and especially along slopes. Since all FDLs are located on slopes, no information on FDLs could be extracted from the acquired data. The interferometric phase maps for both data sets are shown in Figures 3.23b and 3.24b. They indicate spatial phase variations that are most likely associated with atmospheric effects and residual terrain signals. Due to decorrelation, little information can be retrieved on FDLs.

Overall, based on this experiment, two main issues were identified that significantly impact the quality of the TSX interferometric results:

(1) Penetration depth of the X-band data: The summer scenes were selected for this study in order to avoid snow coverage during the winter period; however, the vegetation coverage during the summer season is likely too dense for the X-band signals to

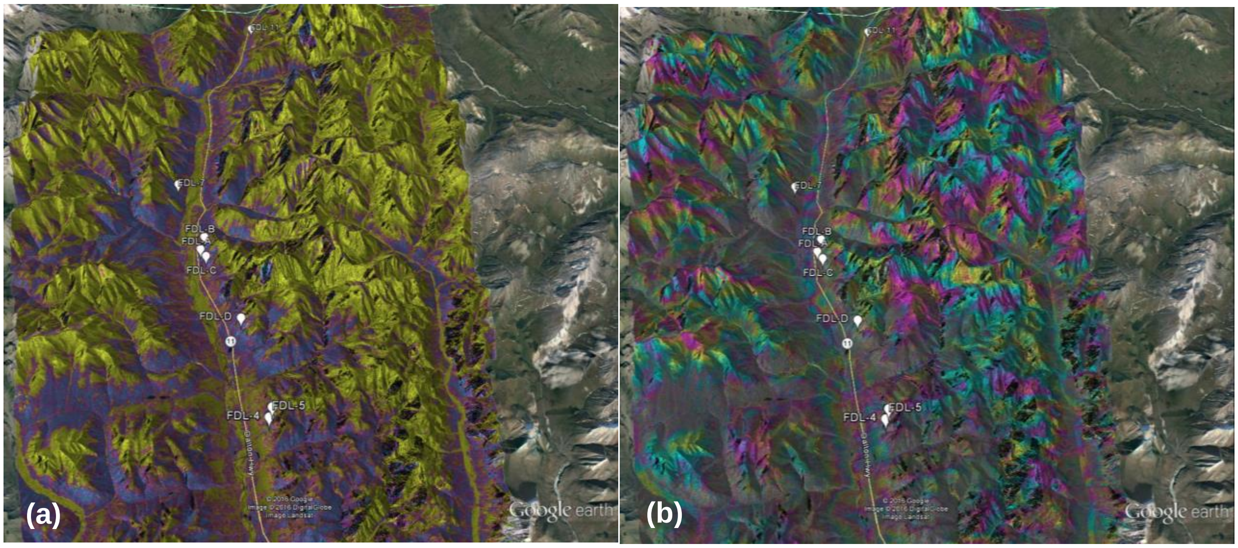

Figure 3.23. Interferometric example of the ascending pair acquired on 2016-06-28 and 2016-07-09 with 24.84m perpendicular baseline and 11-day temporal baseline: (a) In the coherence map, yellow indicates high coherence; and (b) in the wrapped differential interferograms, one color cycle indicates phase changes between [-π, π].

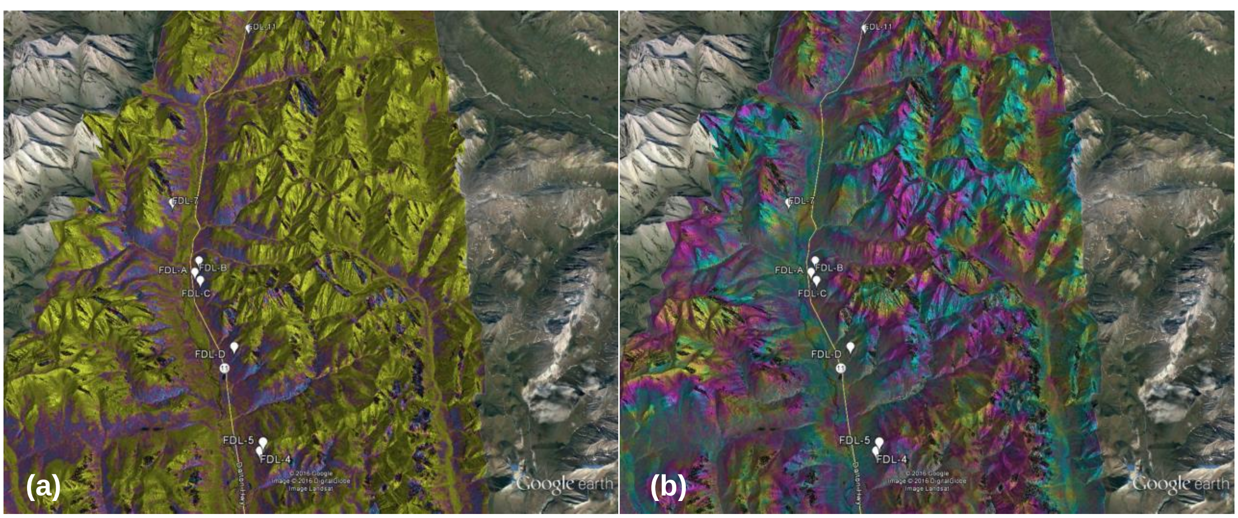

Figure 3.24. Interferometric example of the descending pair acquired on 2016-07-07 and 2016-07-18 with -69.07m perpendicular baseline and 11-day temporal baseline: (a) In the coherence map, yellow indicates high coherence; and (b) in the wrapped differential interferograms, one color cycle indicates phase changes between [-π, π].

penetrate, leading to rapid signal decorrelation within the 11-day repeat period. Lower vegetation coverage at higher elevations preserves coherence better, as shown in Figures 3.23 and 3.24.

(2) Spatially diverse FDL motion: As indicated in the previous InSAR analysis, during the summer season the motion of FDLs can vary significantly over short distances. This spatially "incoherent" motion pattern may lead to the decorrelation of InSAR data.

Offset Tracking on FDLs: In addition to InSAR, offset tracking methods on FDLs were analyzed. SAR-based offset tracking has been implemented successfully for many applications such as glacier motion tracking and the measurement of co-seismic slip. The accuracy of the technique can be at the tens of centimeters level. Hence, it could be a potentially interesting technique when applied to TSX data. In contrast to InSAR, a relatively large time interval (e.g., tens of month or several years) of the data pair is preferred to allow for sufficient motion to occur.

This method was applied successfully to one PALSAR data pair with about a 1-year time interval for testing purposes. The total deformation on FDL-A, -B, and -C was captured well by this data; Figure 3.25a is a presentation of the deformation in ground range while Figure 3.25b is a presentation of deformation measured in azimuth directions. For example, the total displacement of FDL-A was about 5.5m in the ground range direction and about 2.7m in the azimuth direction. These values correspond to an average motion velocity of 1.3 cm/day in ground range and 0.65 cm/day in azimuth direction. Unfortunately, the spatial resolution of PALSAR imagery limits the implementation of the same method to the other FDLs.

Test results using TSX data are presented in Figures 3.26 and 3.27. While TSX data should be good for offset tracking due to its finer spatial resolution, initial experiments with data from 2013 did not result in useful information. As mentioned above, this may be because: (1) the ground movement within a few months (e.g., July to September) was not long enough to create detectable displacement (note that the PALSAR example has a temporal baseline of more than a year); or (2) the ground coverage changed as a result of seasonal variation. Thus, requesting new TSX data to form longer time interval pairs and applying the pixel-offset technique potentially could provide more information on FDLs' displacement fields.

With the programmed TSX dataset acquired in 2016, another round of experiments was conducted with TSX data pairs consisting of images from 2013 and 2016, anticipating that a difference of three years would provide sufficient displacement. Figures 3.26 and 3.27 include two examples of offset tracking results, including one ascending pair (2013-07-05 and 2016-07-09) and a descending pair (2013-07-03 and 2016-06-26), respectively. The image pairs were obtained from similar seasons. To reduce computation load, the TSX images were multi-looked with a factor of 8 (the pixel spacing was approximately 10-15m), and only the portion of the SAR images covering the AOI were cropped and processed. The results from TSX SAR imagery and offset tracking technique, however, were quite disappointing, as no useful displacement information for the FDL locations could be obtained.

Overall, the TSX offset tracking experiment did not yield successful results. Using a longer time span for TSX data pairs (i.e., larger accumulated deformation signals) did not help the performance of TSX with the offset tracking technique. The key issues affecting the results are

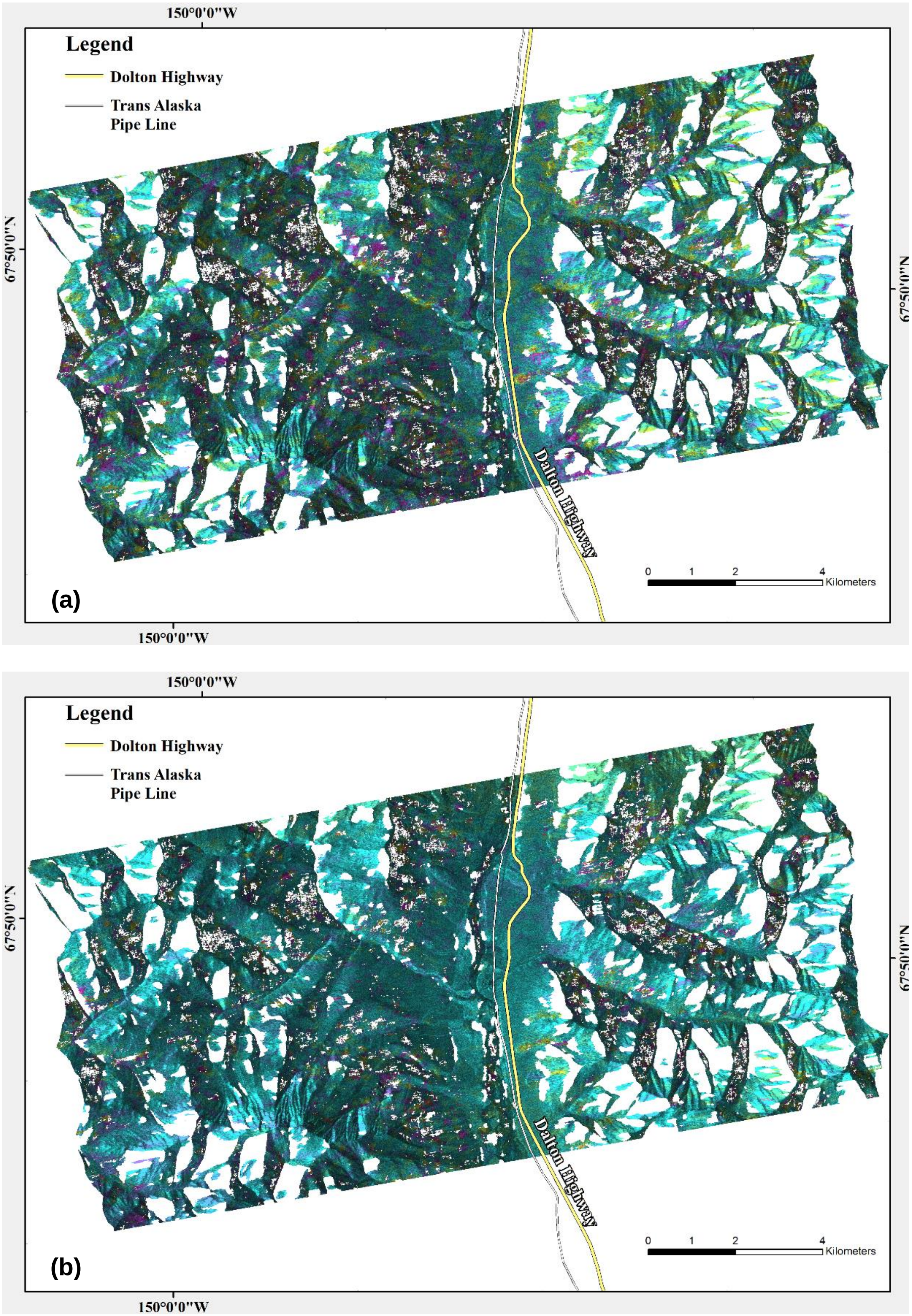

Figure 3.25. Offset tracking results with PALSAR pair 2008-07-24 to 2009-09-11: (a) Ground range offset; (b) azimuth offset.

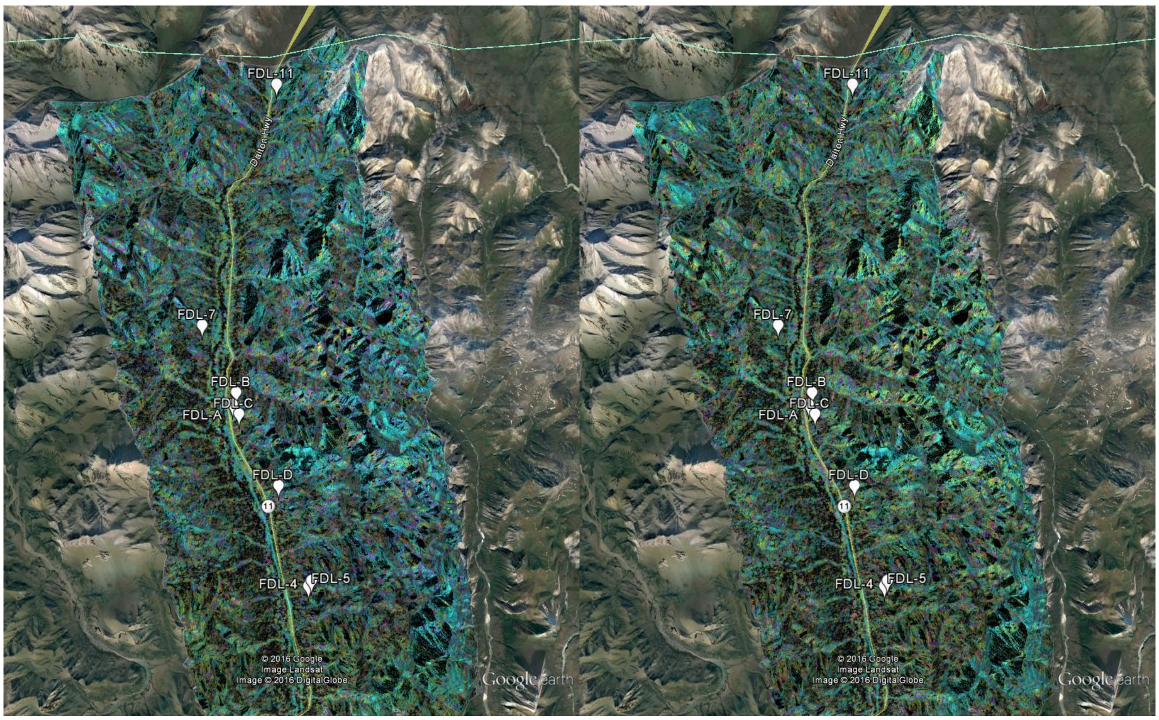

Figure 3.26. Example of offset tracking result measured from TSX ascending data pair 2013-07-05 to 2016-07-09: (a) ground range displacement; (b) azimuth displacement. One color cycle corresponds to 5m. Anomalies (colored speckles) can be observed across the image; regions with black color indicate low signal-to-noise ratio.

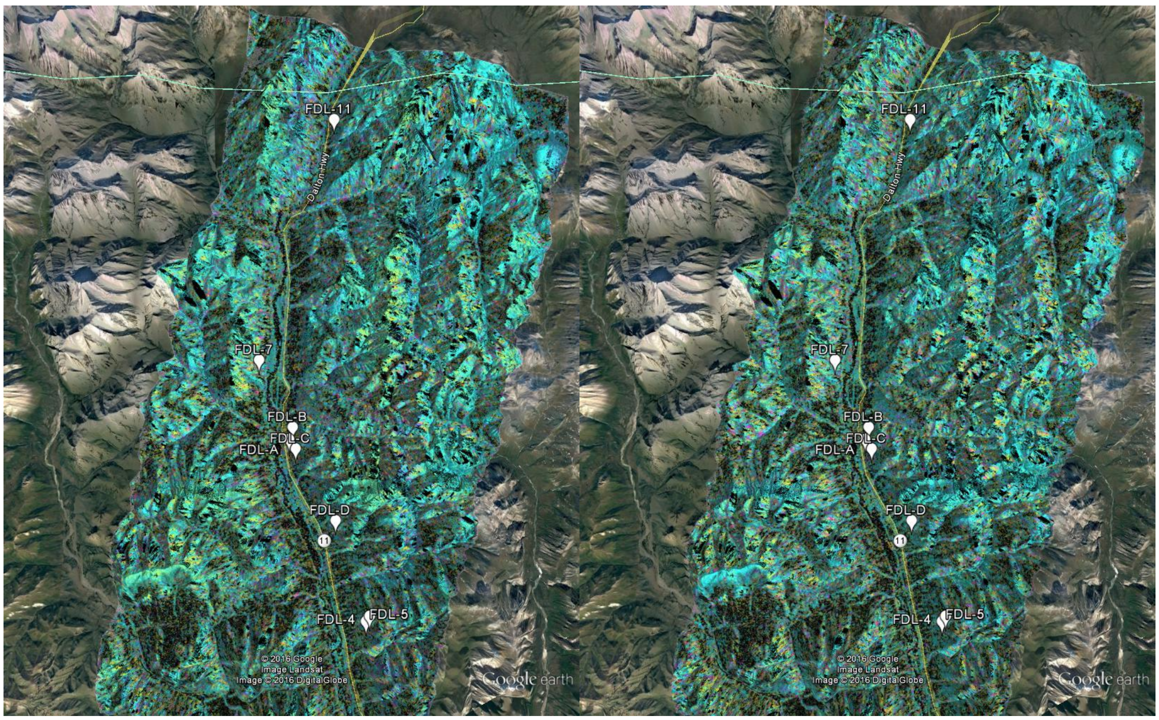

Figure 3.27. Example of offset tracking result measured from TSX descending data pair 2013-07-03 to 2016-06-26. (a) ground range displacement; (b) azimuth displacement. One color cycle corresponds to 5m. Anomalies (colored speckles) can be observed across the image; regions with black color indicate low signal-to-noise ratio.

the complex ground coverage (moving trees, rocks, etc.), shallow penetration depth of the X-band signal, and the non-ideal viewing angle between satellite and slope orientation.

3.2.4 UAS: Low-altitude imaging of FDL-A

Unmanned Aircraft Systems (UAS) were used to collect high-resolution imagery in May 2015 and May 2016, to apply the relatively new photo-modeling technique called Structure-from-Motion (SfM). In this technique, the structure of a feature is resolved using motion-parallax algorithms. The purpose was to generate 3D surface models for each year, and to compare the imagery and models to identify change on the FDL.

Mid- to late-May was identified as the ideal time to acquire the airborne imagery, as this is when there is no snow and the leaves have not yet come out on deciduous vegetation in the Brooks Range, thus ensuring the best imaging of the exposed ground. The missions were conducted on May 20, 2015 and May 18, 2016, and were focused solely near the toe of FDL-A in an attempt to quantify the volumetric change over the course of one year. During each mission, the weather was ideal for imaging with a digital camera; however, light breezes were present, which had a minor effect on UAS performance. The wind had little impact on the rotary-wing hexacopter aircraft. Their autopilots quickly adapted to the changing wind currents in the valley, and these aircraft followed the planned flight lines in the mission programmed into the autopilot. The fixed-wing aircraft demonstrated a reduced performance because the breezes caused a drift from their planned flight lines, creating insufficient image overlap in some swaths of imagery. Table 3.11 is a summary of the different UAS and cameras used during the airborne imagery acquisition.

Approximately 500 images were collected during the 2015 mission, and approximately 800 images were collected in 2016. Flights were planned to capture an 85% overlap with neighboring images, which is required for the SfM algorithm to exploit the parallax of the overlapping imagery to create a 3D model.

To build the 3D model, the first step is to calculate the location and orientation of each camera position corresponding to each image. From these results, a vast number of “tie points” were identified; these link common features from one image to the next, thus generating a matrix of connections that tie all of the images together into a single model of networked tie points. The points are processed further to filter erroneous points and create more points where needed. All of the points in the cloud also are colorized with the corresponding color of the pixels in the imagery. This results in an easily interpreted 3D model that can be moved and rotated for analysis by the user (Figure 3.28).

A wireframe mesh (or triangulated irregular network (TIN)) and gridded mesh (or digital surface model (DSM)) can be created from the points through additional processing steps. For this research, DSMs were produced from the images. The models first were created from each year using positioning data from the aircraft’s on-board GPS. The raw, autonomous accuracy of the GPS is typically 15m. With more GPS readings, and using preplanned flight plans designed to remove GPS bias systematically, the refined GPS accuracy can be improved to 5m. For this analysis, higher accuracy was required. During each May trip, the DGPS unit was used to

Table 3.11. UAS and cameras used during the 2015 and 2016 data acquisitions. (All photographs provided by M2 Flight Solutions (www.m2flightsolutions.com)).

Year	Aircraft	Wing	Camera	Image
2015	DJI Phantom	Rotary	1080p	
2015	3DR Iris	Rotary	1080p GoPro Rectilinear lens	
2015	Raven	Fixed	1080 p GoPro Fish eye lens	
2016	DJI Phantom 4	Rotary	4k	
2016	3DR Arrow	Fixed	Dual (2x) 1080p GoPro	

measure additional survey points installed for the UAS data acquisition (Figure 3.29), which served as additional GSP for imagery correction. After developing the preliminary 3D model, the precise coordinate for each survey point was added, and the model was adjusted to improve its positional accuracy. All DGPS measurements were acquired using the WGS84 coordinate system with ellipsoidal height measurements.

A high-resolution file with a ground sample distance (GSD) of 5cm was developed. Each DSM elevation is an average of bare earth points as well as any points above the ground (i.e., vegetation), and this average is for all neighboring DSM vertices in the sample distance. If there are three vegetation points in the grid, those vegetation points are averaged together, and the height is above the bare earth elevation for that point. Thus, the DSM elevations will not match the DGPS elevations unless the area is void of vegetation. As FDL-A supports spruce trees, alder and willow shrubs, and a variety of ground cover species (Figure 3.28), the vegetation must be removed to produce an adequate DEM. Since the SfM method yields identifiable morphology of surface features, the point cloud data was filtered based on morphology. Through trial and error, the point cloud for FDL-A was processed to remove an estimated 75% of the vegetation data (Figure 3.30).

To assess the accuracy of this technique, the 2015 SfM-derived DEM elevations (as well as the 2015 LiDAR DEM elevations) were compared to the measured DGPS elevations (Table 3.12). As the SfM DEM and DGPS data sets both used the WGS84 ellipsoidal datum, these elevations could be compared directly. The 2015 LiDAR DEM used the orthometric NAVD88 vertical datum, requiring a local correction factor to be applied to all points to convert to ellipsoidal elevations. A minimum error of 10cm was assumed for the DGPS-derived elevations, which is twice the accuracy stated by the manufacturer; only differences greater than this value are listed in Table 3.12. The three different methods produce good agreement in elevations for most of the points. Both the LiDAR and SfM DEMs indicated higher elevations for point FDLA020. This point is surrounded by several spruce trees and shrubs that have potential to obscure the surface, possibly contributing to the differences in elevation (Figure 3.31a). For point FDLA027, both the LiDAR and SfM DEMs indicated lower elevations. This point is falling down the toe slope of FDL-A (Figure 3.31b). The DEMs are rasters with elevations representing an average value for an entire pixel, whereas the DGPS elevations are measured for a specific point. This may explain the discrepancy at point FDLA027.

Finally, the 2015 and 2016 SfM-derived DEMs were compared to determine change in volume for the toe of FDL-A. The two DEM rasters were differenced to produce a DoD for the polygonal area shown in Figure 3.32. Analysis indicates a net volume increase of 7,030m^3 between 2015 and 2016. This equates to about <u>19.3m^3 (i.e., about 25yd^3) advancing to the road per day</u>. Based on typical commercial dump truck capacities, when FDL-A hits the highway, <u>two dump trucks will be required to remove the material every day</u>. It also should be noted that this is for the toe area of FDL-A only, and does not consider its greater width, and thus larger volume, farther upslope.

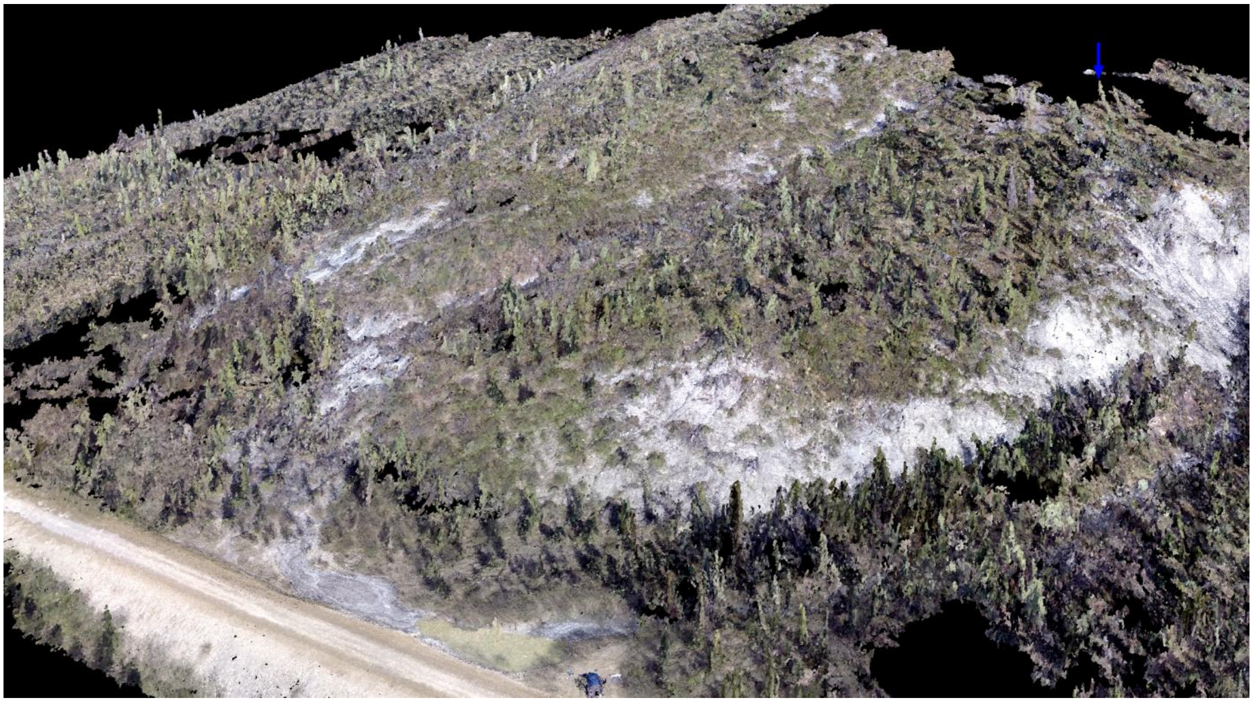

Figure 3.28. Oblique screen shot of the May 2015 FDL-A point cloud data. The view is to the northeast, with the Dalton Highway along the bottom left.

Figure 3.29. Aerial image of an orange bucket lid secured to the ground with a steel bar, which served as a surface marker pin.

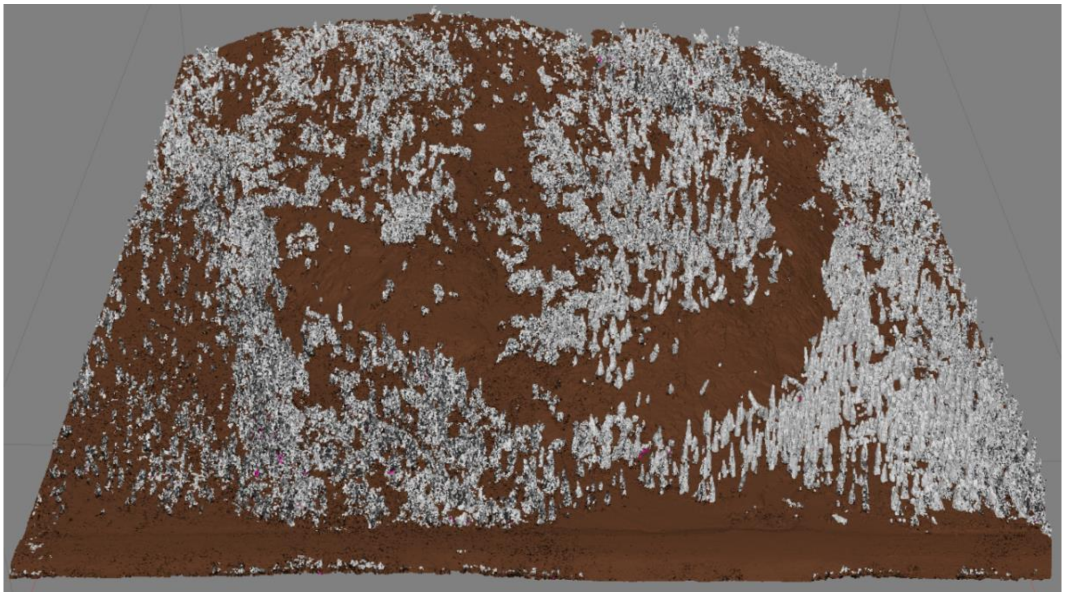

Figure 3.30. Classified point cloud for the toe of FDL-A. Bare earth points are brown, and vegetation is white. View is to the east, and the Dalton Highway is along the bottom edge of the model.

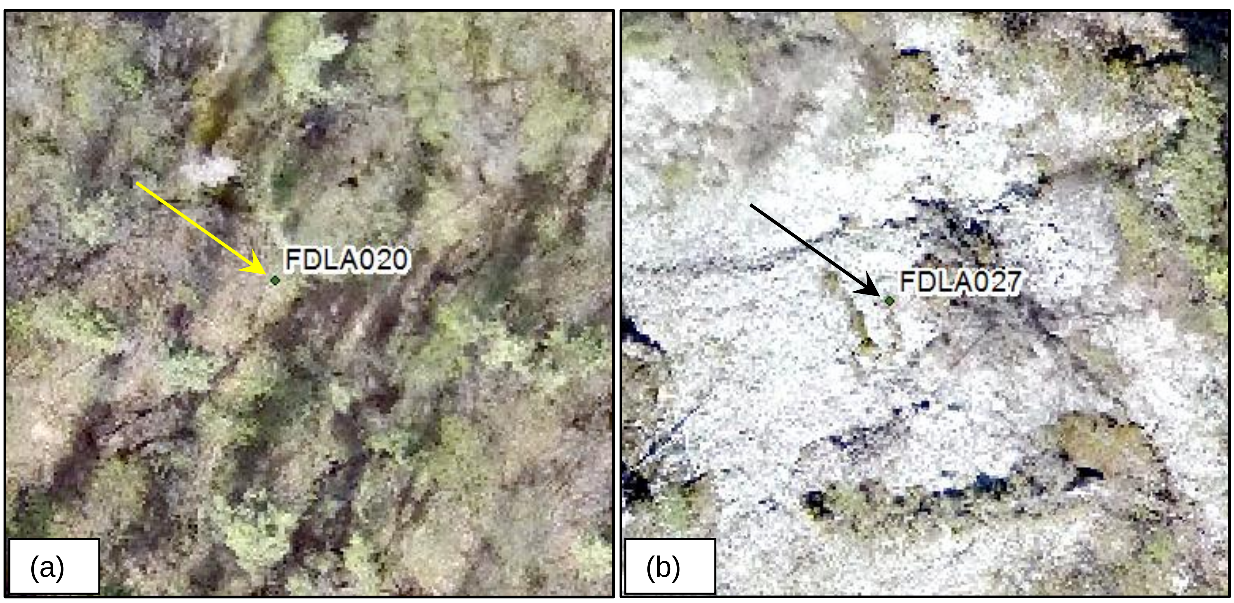

Figure 3.31. UAS-derived image of (a) FDLA020, illustrating spruce tree and shrub coverage over the point; and (b) FDLA027, illustrating the bare, unstable nature of the toe of FDL-A. Both images are at a 1:200 scale.

Table 3.12. Comparison of May 2015 elevation data produced from DGPS measurements (acquired May 26, 2016; WGS84), LiDAR (acquired May 19-21, 2015; converted to ellipsoidal elevation), and SfM (acquired May 20, 2016; WGS84) data.

Surface marker ID	DGPS-derived elevation (m)	LiDAR DEM elevation (m)	LiDAR-DGPS difference (if >±10cm) (m)	SfM-derived DEM elevation (m)	SfM-DGPS difference (if >±10cm) (m)
FDLA014	590.92	590.83	---	590.87	---
FDLA015	584.88	584.84	---	585.06	0.18
FDLA016	574.23	574.07	-0.15	574.19	---
FDLA017	569.09	569.03	---	569.14	---
FDLA018	565.33	565.43	---	565.45	0.11
FDLA019	571.21	571.17	---	571.21	---
FDLA020	575.86	576.05	0.19	576.23	0.37
FDLA021	575.64	575.56	---	575.71	---
FDLA022	575.12	575.27	0.15	575.02	---
FDLA023	565.72	565.82	---	565.69	---
FDLA024	565.51	565.39	-0.12	565.81	0.30
FDLA025	565.91	565.93	---	566.02	0.12
FDLA026	566.41	565.77	-0.64	566.40	---
FDLA027	561.79	561.47	-0.32	561.67	-0.12

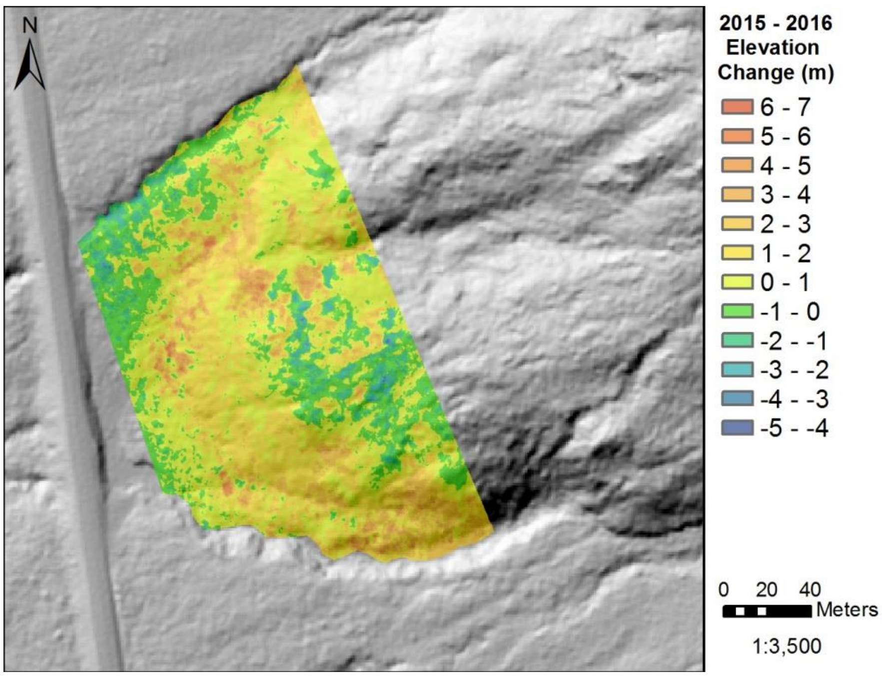

Figure 3.32. DoD for the toe area of FDL-A, illustrating change from 2015 to 2016. The DoD was produced by differencing the SfM-derived DEM rasters. The comparison area was trimmed to the creeks draining from each side of FDL-A.

3.3 Summary of research products

The results of this research have been summarized in regular quarterly reports to the USDOT, and ultimately in this final report. Also available on the project website (fdlalaska.org) are two short videos that were developed as part of this research. Conversations with personnel from the agencies with a vested interest in FDLs (i.e., the Alaska Department of Transportation and Public Facilities (ADOT&PF) and the Alyeska Pipeline Service Company (Alyeska)) indicated that 3D visualizations of these features are important. The 3D graphics in a short video format explain the relative scale and shape of FDLs, and illustrate their downslope progression through time. Agency personnel can use these videos as visual aids when talking with the decision makers about mitigation options.

Over the course of this project, the PI has provided key personnel from the ADOT&PF and Alyeska with regular updates on FDL rates of movement and key findings from field observations. Additionally, the ortho-mosaics and short videos were bundled and delivered to ADOT&PF and Alyeska for their use. The short videos were well received, and immediately disseminated throughout each organization.

Accompanying this report is a "best practices guide", which briefly lists the pros and cons of each method based on the results from this research. The guide also is integrated into the project website.

Research results also were disseminated through a variety of sources, including two peer-reviewed journal papers and eight conference papers and presentations (complete references provided below). Links to the documents available from the internet are provided on the website (fdlalaska.org). The following is a list of the papers and presentations resulting from this research project.

Two Peer-reviewed Papers:

Darrow, M. M., Gyswyt, N. L., Simpson, J. M., Daanen, R. D., Hubbard, T. D. (2016). "Frozen debris lobe morphology and movement: an overview of eight dynamic permafrost features, Brooks Range, Alaska." *The Cryosphere*, 10, 977-993, doi:10.5194/tc-10-977-2016.

Gong, W., Meyer, F. J., McAlpin, D., Darrow, M. M., Daanen, R. P. "Monitoring frozen debris lobes in northern Alaska using satellite radar interferometry." *Remote Sensing of the Environment.* (This paper is currently in preparation.)

Eight Conference Papers and Presentations:

Cunningham, K. W. (2016). "Multidisciplinary unmanned aircraft systems research and applications." *American Society for Photogrammetry and Remote Sensing (ASPRS) Imaging & Geospatial Technology Forum (IGTF),* Fort Worth TX, April 11-15, 2016.

Darrow, M. M. and Daanen, R. P. (2016). "Internal Creep Dynamics of Frozen Debris Lobe-A, Brooks Range, Alaska." *AGU Fall Meeting Abstracts*, San Francisco, CA, December 12-16, 2016, GC31H-1198.

Darrow, M. M., Gyswyt, N. L., Gong, W., Meyer, F. J., Cunningham, K., Daanen, R. P. (2016). "Monitoring and analysis of frozen debris lobes using remote sensing: a multi-modal approach to geohazard analysis along infrastructure." *Transportation Research Board, 95th Annual Meeting - Sensing Technologies for Transportation Applications Workshop*, Washington, D.C., January 10-14, 2016.

Gyswyt, N. L., and Darrow, M. M. (2015). "Geospatial analysis of frozen debris lobe historic movement, Dalton Highway, Alaska." *Cordilleran Section, GSA 111th Annual Meeting,* Anchorage, AK, May 11-13, 2015.

Gyswyt, N. L., and Darrow, M. M. (2016). "Topographic change analysis using LiDAR differencing: A case study from a frozen debris lobe, Brooks Range, Alaska." *Proc., 2016 Association of Environmental and Engineering Geologists Annual Meeting*, September 17-25, 2016.

Gyswyt, N. L., Darrow, M. M., Daanen, R. D. "Using LiDAR to analyze mass movement of frozen debris lobes, Brooks Range, Alaska." *3rd North American Symposium on Landslides*. (Abstract accepted; paper in review.)

Gyswyt, N. L., Darrow, M. M., Daanen, R. D. (2016). "Historic movement analysis of frozen debris lobes, southern Brooks Range, Alaska." *ICOP 2016 - International Conference on Permafrost*, Potsdam, Germany, June 19-24, 2016, 1003-1004.

Gong, W., Meyer, F. J., Darrow, M. M., Daanen, R. P. (2015). "Monitoring frozen debris lobes in northern Alaska using satellite radar interferometry." *2015 IEEE International Geoscience and Remote Sensing Symposium (IGARSS),* July 26-31, 2015.

McAlpin, D. B., Meyer, F. J., Darrow, M. M., Gong, W., Daanen, R. P. (2015). "Using SAR interferometry to assess infrastructure hazards from frozen debris lobes in northern Alaska." *AGU Fall Meeting Abstracts*, San Francisco, CA, December 14-18, 2015, IN11A-1770.

CHAPTER 4: PART II - PERFORMANCE OF THE METHODS

4.1 Measurements Using Differential GPS Device

For this project, the measurements made with the DGPS device are considered to be the most accurate, with manufacturer-reported horizontal and vertical accuracies of ±5cm. Using a DGPS system requires the initial purchase cost or rental fee for use. Subsequently, the user needs sufficient training on how to set up and troubleshoot the system, since typically no external help is available in remote locations. Once past that learning curve, the data is only limited by the number of measurements the user is willing to make.

The limitations with this method as evidenced through this project are the temporal and spatial distributions of data. Measurements were limited to when the research team was in the field, and to where surface measurement markers were placed. Thus, measurements require field work and its associated costs. Despite the discrete rather than continuous nature of this data, DGPS measurements are essential for establishing baseline conditions, and as presented in the previous sections, integrate well into data obtained from other methods, such as optical imagery, and LiDAR and InSAR data.

4.2 Historic Imagery Analysis

Historic imagery analysis requires no field work or special equipment. Depending on the availability of free or lost-cost imagery, this analysis method can be inexpensive in comparison to other methods. It also can cover a longer time frame, if images are available, which is beneficial to the study of FDLs due to their relatively slow rates of movement.

One major limitation of this method is the quality of historic imagery. Low resolution imagery is difficult to orthorectify and yields imprecise measurements, decreasing the accuracy of the overall analysis. Additionally, poor lighting, poor geometry, and cloud or smoke cover at the time of image acquisition also will preclude certain scenes from use. Due to the remote location of the AOI, the frequency of imagery collection prior to 2000 was low, which affects the temporal resolution of rate measurements. Finally, historic imagery does not contain elevation data, which limits the type of analysis that can be done.

4.3 LiDAR Comparison

The LiDAR data available for this project has a high resolution with a pixel size of 1 m^2, which allows for more precise measurements. This method also produces accurate models, since the 2011 and 2015 LiDAR had absolute vertical RMSE accuracies of 3.5cm and 7cm, respectively. LiDAR data is versatile as multiple models can be derived from one data set. The first return of the laser pulse is used to create a DSM, which represents all features present in the study area, including trees and shrubs. The last return of the laser pulse is used to create a DEM, which represents the bare earth. The FDL study area is densely vegetated, so removing the vegetation from view allows more analysis of the geomorphology and precise measurements of the terrain. The extent of an FDL can be mapped from LiDAR data more clearly than with other methods. Other LiDAR products include distribution of slope angle, aspect, and curvature. FDL displacement can be measured on a point-to-point basis by comparing the dataset to other

LiDAR or historic imagery. Additionally, two LiDAR-derived DEMs can be differenced to provide a more comprehensive analysis of change of the entire AOI.

One limitation of this method is that new, airborne LiDAR datasets are expensive to acquire. Part of the expense is the required ground control to orthorectify the final product. Since LiDAR is a relatively new remote sensing tool, it is unlikely that historic LiDAR datasets exist for remote study areas. Additionally, new LiDAR acquisitions require careful planning to ensure that weather conditions are optimal; it also is recommended to acquire LiDAR data when there is no snow coverage and no leaves on deciduous vegetation. When vegetation has leafed-out, it is more difficult for the laser pulses to hit the ground surface, which may result in errors. This type of error can overestimate the bare earth height in densely vegetated areas.

4.4 InSAR Analysis

A diverse set of SAR data were used in this study to be able to make scientifically defendable conclusions about the suitability of InSAR for the monitoring of FDLs. Data differed in center frequency, spatial resolution, and temporal repeat frequencies and allowed the study of InSAR performance with respect to the most relevant observational parameters. The following lists the main findings by starting from the identified capabilities, identifying synergies with other observational methods, and ending in limitations and recommendations.

Capabilities: *(1) Spatial FDL dynamics*: InSAR can be a useful tool for analyzing the spatial variability of FDL flow velocity. Specifically, data acquired in the winter season was able to measure sub-centimeter per year variations of flow velocity across an FDL body. Furthermore, repeated interferograms throughout the winter season were able to trace changes of this flow pattern from late fall into the early spring. Despite its capability, data for this task has to be selected with care, as surface velocity across an FDL changes quickly in space. For example, on FDL-A, motion changed from zero to 3 cm/day across a distance of less than 100m. This strong velocity gradient can lead to signal decorrelation if the motion difference between two pixels exceeds half the sensor wavelength. Hence, the following approximate equation can be used as a rule of thumb to determine the maximum allowable temporal baseline Δt_{max} for analyzing the spatial deformation patterns of FDLs:

$$\Delta t_{max} = \frac{\lambda \cdot (w_{FDL}/(2 \cdot r))}{v_{max} \cdot 2} \tag{2}$$

where w_{FDL} is the approximate width of the FDL, v_{max} is its maximum velocity in m/day, r is the approximate (multi-look) resolution of the InSAR data set, and λ is the sensor wavelength. This equation assumes that the maximum velocity is achieved near the longitudinal center of an FDL. According to this equation, the approximate temporal baselines for X-, C-, and L-band should not exceed (example assumes conditions at FDL-A): $\Delta t_{max}^{X-band} \approx 6\ days$; $\Delta t_{max}^{C-band} \approx 5\ days$; and $\Delta t_{max}^{L-band} \approx 21\ days$. The only data set available to us that met these requirements were the C-band ERS-1/2 tandem data, whose 1-day temporal baseline was shorter than the C-band maximum of 5-days.

(2) Identifying FDLs in a landscape: A second application of InSAR is the identification of FDLs in a previously unexplored landscape. All FDLs for which the condition in Eq. (2) is met are

recognizable through their anomalous phase patterns in formed interferograms. A given interferogram with wavelength λ, resolution r, and temporal baseline Δt should allow for the identification of FDLs whose width-over-velocity ratio meets the following criterion:

$$\frac{w_{FDL}}{v_{max}} = \frac{\Delta t \cdot 4 \cdot r}{\lambda} \quad (3)$$

If several interferograms with different combinations of λ, r, and Δt are used, a wide range of FDL types can be discovered.

(3) Measuring seasonal variations of FDL velocity: The typical regular repeat acquisitions of SAR sensors provide a good basis for analyzing seasonal variations in FDL movement. Especially for the winter season, InSAR data revealed consistent patterns of seasonal velocity variation across all studied FDLs. Surface velocity peaked in late October, dropped significantly until late February to early March and increased again thereafter. As for FDL dynamics, the data used for observations need to meet the criterion in Eq. (2) to yield information.

Limitations: Preserving interferometric coherence is the key to the successful use of InSAR for FDL monitoring. Several decorrelation sources may contribute to signal degradation at FDLs. (1) Decorrelation is aided by the fast motion and small size of FDLs (small is relative to the satellite pixel resolution). The fast motion of FDLs causes co-registration issues of FDL pixels if the temporal baseline Δt is too long (i.e., the content of an FDL pixel of image #1 is not the same as the pixel in image #2). The narrow width of FDLs also causes strong motion gradients that limit Δt according to Eq. (2); longer wavelengths and higher spatial resolutions are more conducive to FDL monitoring. (2) As FDLs are typically covered in vegetation, seasonal change of this vegetation introduces decorrelation and limits the maximum allowable Δt. In addition to vegetation, the strong seasonal snow cover variation in Arctic environments affects coherence if Δt increases. Both vegetation and snow impacts are stronger at high frequencies (e.g., X-band). Coherence limitations are exaggerated by the irregular sampling with SAR data that was experienced during the time frame of this study. None of the currently flying sensors provide repeat acquisitions at a temporal sampling that is required according to Eq. (2).

In addition to coherence constraints, the satellite geometry also can play an important role when monitoring FDLs with InSAR. As FDLs are mostly located in sloped terrain, and as InSAR observations are only sensitive to motion in the sensor's line-of-sight, the relative viewing geometry between sensor and surface slope is an important parameter. Data are preferred where FDL flow direction is reasonably aligned with the sensor look direction.

Of all currently operating space borne radar systems, PALSAR-2 stripmap mode data may be most appropriate for FDL monitoring. If temporal sampling over FDLs can be improved, data from the Sentinel-1 C-band SAR system also may be of interest. Depending on the data sets chosen, commercial fees may be applied.

Synergies: The identified strengths of InSAR lend themselves well for combination with some of the other measurement techniques that were applied in this study. InSAR can be used to understand seasonal cycles in FDL velocity. Once understood, this seasonal cycle information can be used to interpolate episodic measurements made with the DGPS unit. Spatial information of surface velocity from InSAR also can be used together with DGPS measurements to verify volume change estimates from DEM differencing.

4.5 UAS Analysis

The UAS method requires the purchase of the unmanned aircraft and cameras to be used in the data collection. As indicated in this study, one type of aircraft (i.e., fixed-wing or rotary) may be more appropriate for a specific project. The camera must produce high resolution images in order to employ a method such as SfM. All of this equipment requires training and a skilled operator.

Strengths of the UAS and SfM techniques include the ease and flexibility of deployment of the aircraft, and rapid data collection with the onboard camera. One weakness is the limited data collection window. Much like the LiDAR method, the data is best collected during leaf-off and no-snow conditions. Also, winds must be light for the fixed-wing aircraft. Although the on-board GPS linked to the UAS autopilot provided a rough model location with 5-10m accuracy, ground control was required to improve the overall accuracy of the models produced from these methods.

Most of the vegetation was removed during post-processing to create a bare earth DEM; however, the vegetation removal was not 100% complete. The morphology filtering approach requires more software development, which although beyond the scope of this project, is another area of research in remote sensing and geospatial modeling. The SfM data processing is computationally intensive, requiring supervision of the operator. A robust computer (in this case, 16 CPU cores and 32 GB of RAM) required approximately 100 hours of processing time per model. These techniques produced two DEMs that were used to perform change detection and produced reasonable results.

CHAPTER 5: DISCUSSION AND CONCLUSIONS

Before beginning this project, the research team had limited knowledge of historic rates and only one year of field measurements for the eight investigated FDLs. The trips to the field provided the opportunity to observe signs of increasing instability (such as crack and scarp development, and exposure of massive ice). For example, field observations suggested that FDL-11 had experienced rapid movement in the past, although currently it demonstrates negligible movement; however, this hypothesis could not be proven without additional information. By integrating the historic analysis, the InSAR analysis, DGPS measurements, and subsurface measurements, a more comprehensive understanding of FDL rates and movement dynamics has been developed.

The investigated FDLs currently demonstrate different rates of movement, varying from 0.2 m/yr for FDL-11 to nearly 20 m/yr for FDL-D, and seven of the eight FDLs demonstrate increasing rates of movement based on DGPS measurements. For many of the FDLs, the current DGPS measurements fit within the long-term movement trends based on historic imagery (see Figures 5.1 and 5.2). Excellent examples of this are FDL-7 and FDL-A, both of which have been accelerating since 1955 (Figure 5.1b and 5.1d, respectively). Another example, although in opposite trend, is FDL-11. The historic image analysis validated the field observations of FDL-11, since it did experienced rapid movement in the 1970's moving nearly 10 m/yr. For the other FDLs, the DGPS measurements fit within the range of historic rates. Also included in Figures 5.1 and 5.2 are the 1995 movement rates derived from the InSAR analysis. It must be stressed that although the InSAR values were converted into the FDL motion directions from the satellite's line-of-sight direction, uncertainty still remains in the calculation of absolute rates. Despite this known uncertainty, the resulting values are reasonable, fitting the long-term trends for each of the investigated FDLs. In summary, the historic imagery analysis and current DGPS measurements complement each other. Each method yields different information necessary to establish long-term rate trends and the confidence to project such trends into the future.

While there is uncertainty in the absolute rates determined from the InSAR analysis, the InSAR data provides a view into FDL dynamics at a seasonal scale. The initial surface measurements of FDL-A indicated that the lobe may move the fastest in October, reaching a minimum rate of movement in February or March; however, this hypothesis initially was based on very few measurements. It is supported further by the ongoing analysis of subsurface data from the M-IPI, which also indicate a peak in movement in October, and a minimum movement rate in February or March. Integrating the InSAR analysis provides a third piece of evidence to support this hypothesis for FDL-A, as well as all of the other investigated FDLs. The InSAR analysis also illustrated the seasonal changing distribution of internal deformation for all of the FDLs. This is something that was not captured with field DGPS measurements mostly due to the limited number of trips to the field.

In summary, the results of this integrated research indicate:

- The rate of motion of FDLs has increased over the last 60 years, with the eight FDLs investigated moving asynchronously to each other.

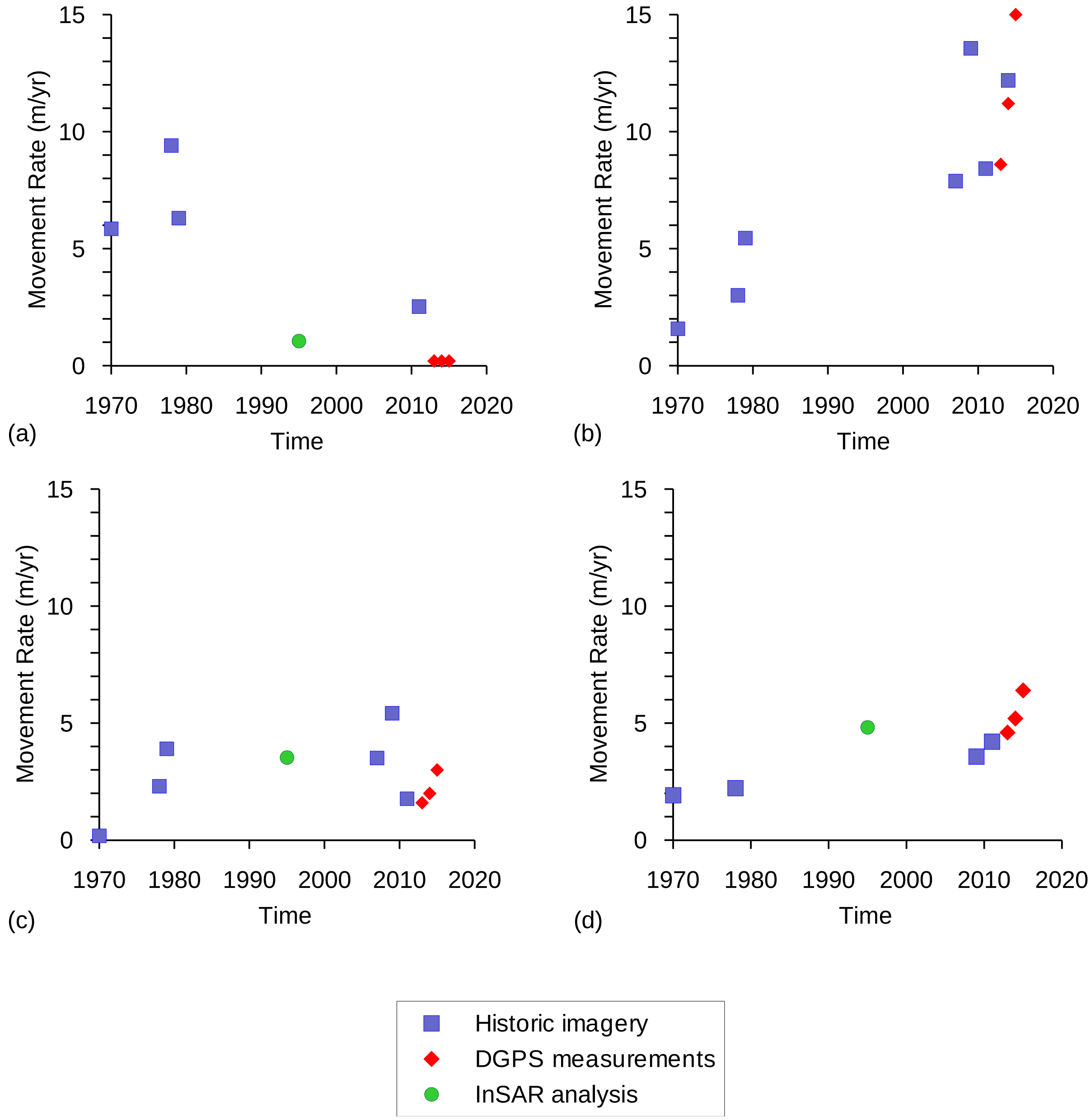

Figure 5.1. Integrated FDL rates from historic imagery and DGPS measurements for the northern portion of the AOI. Rates are listed for FDLs north to south: (a) FDL-11, (b) FDL-7, (c) FDL-B, and (d) FDL-A. No InSAR analysis could be completed for FDL-7 based on available data.

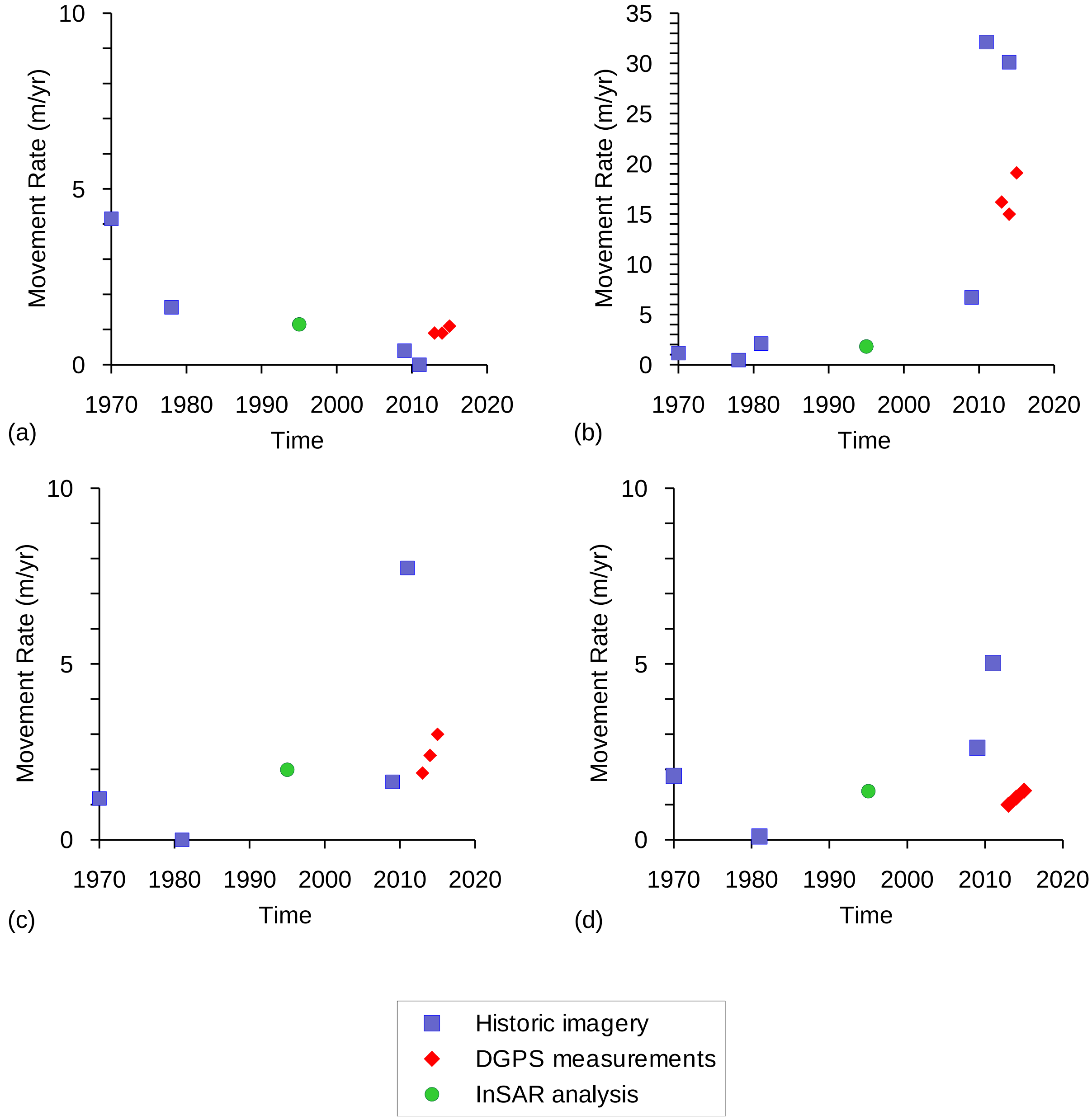

Figure 5.2. Integrated FDL rates from historic imagery and DGPS measurements for the southern portion of the AOI. Rates are listed for FDLs north to south: (a) FDL-C, (b) FDL-D, (c) FDL-5, and (d) FDL-4.

- In the last 40 years, scarps have developed in the catchments of the investigated FDLs, which may indicate increasing instability.
- The movement dynamics across the surface of a given FDL vary significantly throughout the year.
- All of the investigated FDLs demonstrated a maximum rate movement in late October, and a minimum of rate of movement in late February.
- The closest FDL to the Dalton Highway is FDL-A.
  - As of October 2016, FDL-A was 32.2m from the toe of the highway embankment.
  - It moved at an average rate of 6.4m/yr over 2015/16, and its rate steadily increased over the measurement period.
  - Based on these values, FDL-A will reach the Dalton Highway by 2021.
  - FDL-A is impacting the subsurface ahead of its toe, possibly shearing deeper that the original ground surface.
  - When FDL-A impacts the highway, its narrowest portion will deposit over $19m^3$ (or $25yd^3$) of material on the highway every day. This equates to about two dump truck loads a day, and does not consider that FDL-A becomes wider uphill.

REFERENCES

Brown, J. and Kreig, R. A. (1983). *Guidebook to Permafrost and Related Features along the Elliott and Dalton Highways, Fox to Prudhoe Bay, Alaska*: Alaska Division of Geological and Geophysical Surveys Guidebook 4, 230 p.

Cornforth, D. H. (2005). *Landslides in Practice: Investigations, Analysis, and Remedial / Preventative Options in Soils*: John Wiley and Sons, Inc., Hoboken, NJ.

Daanen, R. P., Grosse, G., Darrow, M. M., Hamilton, T. D., Jones, B. M. (2012). "Rapid movement of frozen debris-lobes: implications for permafrost degradation and slope instability in the south-central Brooks Range, Alaska." *Natural Hazards and Earth System Sciences*, 12, 1521-1537, doi:10.5194/nhess-12-1521-2012

Darrow, M. M., Daanen, R. P., Simpson, J. M. (2012). *Monitoring and Analysis of Frozen Debris Lobes, Phase I*: FHWA-RD-AK-12, INE/AUTC 12.25; UAF Institute of Northern Engineering, 63 p.

Darrow, M. M., Daanen, R. P., Simpson, J. M. (2013). "Analysis of a frozen debris lobe: A first look inside an impending geohazard." In Zufelt, J. E. (Ed.), *ISCORD 2013: 10th International Symposium on Cold Regions Development*, Anchorage, AK, June 2-5, 2013, 139-148.

Darrow, M. M. (2015). *Monitoring and Analysis of Frozen Debris Lobes, Phase 1B*: UAF Institute of Northern Engineering, 13 p.

Darrow, M. M., Simpson, J. M., Daanen, R. P., Hubbard, T. D. (2015). "Characterizing a frozen debris lobe, Dalton Highway, Alaska." *Cold Regions Engineering 2015*, Salt Lake City, UT, July 19-22, 2015, 57-67, doi:10.1061/9780784479315.006

Darrow, M. M., Gyswyt, N. L., Simpson, J. M., Daanen, R. P, Hubbard, T. D. (2016). "Frozen debris lobe morphology and movement: an overview of eight dynamic features, southern Brooks Range, Alaska." *The Cryosphere*, 10, 977-993, doi:10.5194/tc-10-977-2016

GINA – Geographic Information Network of Alaska. (2001). *Interferometric Synthetic Aperture Radar (IfSAR).* http://www.gina.alaska.edu/data/ifsar (Last access: 9 December 2015).

GINA – Geographic Information Network of Alaska. (2016). *SDMI best data layer - BDL*. www.alaskamapped.org/bdl/ (Last access: 18 October 2016).

Hamilton, T. D. (1978). *Surficial Geologic Map of the Chandalar Quadrangle, Alaska*: U.S. Geological Survey Miscellaneous Field Studies Map MF-878A, scale 1:250,000.

Hamilton, T. D. (1979). *Surficial Geologic Map of the Wiseman Quadrangle, Alaska*: U.S. Geological Survey Miscellaneous Field Studies Map MF-1122, scale 1:250,000.

Hamilton, T. D. (1981). *Surficial Geologic Map of the Survey Pass Quadrangle, Alaska*: U.S. Geological Survey Miscellaneous Field Studies Map MF-1320, scale 1:250,000.

Hanssen, R. (2001). *Radar Interferometry: Data Interpretation and Error Analysis*: Kluwer Academic Publishers, New York, NY.

Hubbard, T. D., Koehler, R. D., Combellick, R. A. (2011). *High-resolution LiDAR Data for Alaska Infrastructure Corridors.* LiDAR Datasets of Alaska, Alaska Division of Geological & Geophysical Surveys (DGGS) Raw Data File 2011-3, DGGS, http://dggs.alaska.gov/pubs/id/22722. (Last access: 15 June 2013).

Hubbard, T. D., Spangler, E., Daanen, R. D., Darrow, M. M., Simpson, J. M., Southerland, L. (2013). "Frozen debris lobes – characterizing a potential geologic hazard along the Dalton Highway, southern Brooks Range, Alaska." *GSA Abstracts with Programs*, 45(7).

Kreig, R. A. and Reger, R. D. (1982). *Air-photo Analysis and Summary of Landform Soil Properties along the Route of the Trans-Alaska Pipeline System*: Alaska Division of Geological and Geophysical Surveys, Anchorage, AK.

Simpson, J. M., Darrow, M. M., Huang, S. L., Daanen, R. P., Hubbard, T. D. (2016). "Investigating movement and characteristics of a frozen debris lobe, South-Central Brooks Range, Alaska." *Environmental and Engineering Geoscience*, 22(3), 259-277.

Simpson, J. M., Hubbard, T. D., Darrow, M. M. (In review). *Assessing the potential hazards of frozen debris lobes through a GIS analysis*. Alaska Division of Geological & Geophysical Surveys.

Spangler, E. R. and Hubbard, T. D. (In review). *Geologic and Geomorphic Characterization of Frozen Debris Lobe Sources Basins along the Dalton Highway, Southern Brooks Range, Alaska.* Alaska Division of Geological & Geophysical Surveys.

Spangler, E., Hubbard, T. D., Daanen, R. D., Darrow, M. M., Simpson, J. M., Southerland, L. (2013). "Geologic and geomorphic characterization of frozen debris lobe catchments along the Dalton Highway, southern Brooks Range, Alaska." *GSA Abstracts with Programs*, 45(7).

FINAL REPORT - APPENDICES

APPENDIX A: Spatial distribution of yearly movement maps for the eight investigated FDLs

The following figures are arranged in geographic order, presenting the FDLs from north to south within the AOI. A set of images is presented both for 2014-15 and 2015-16.

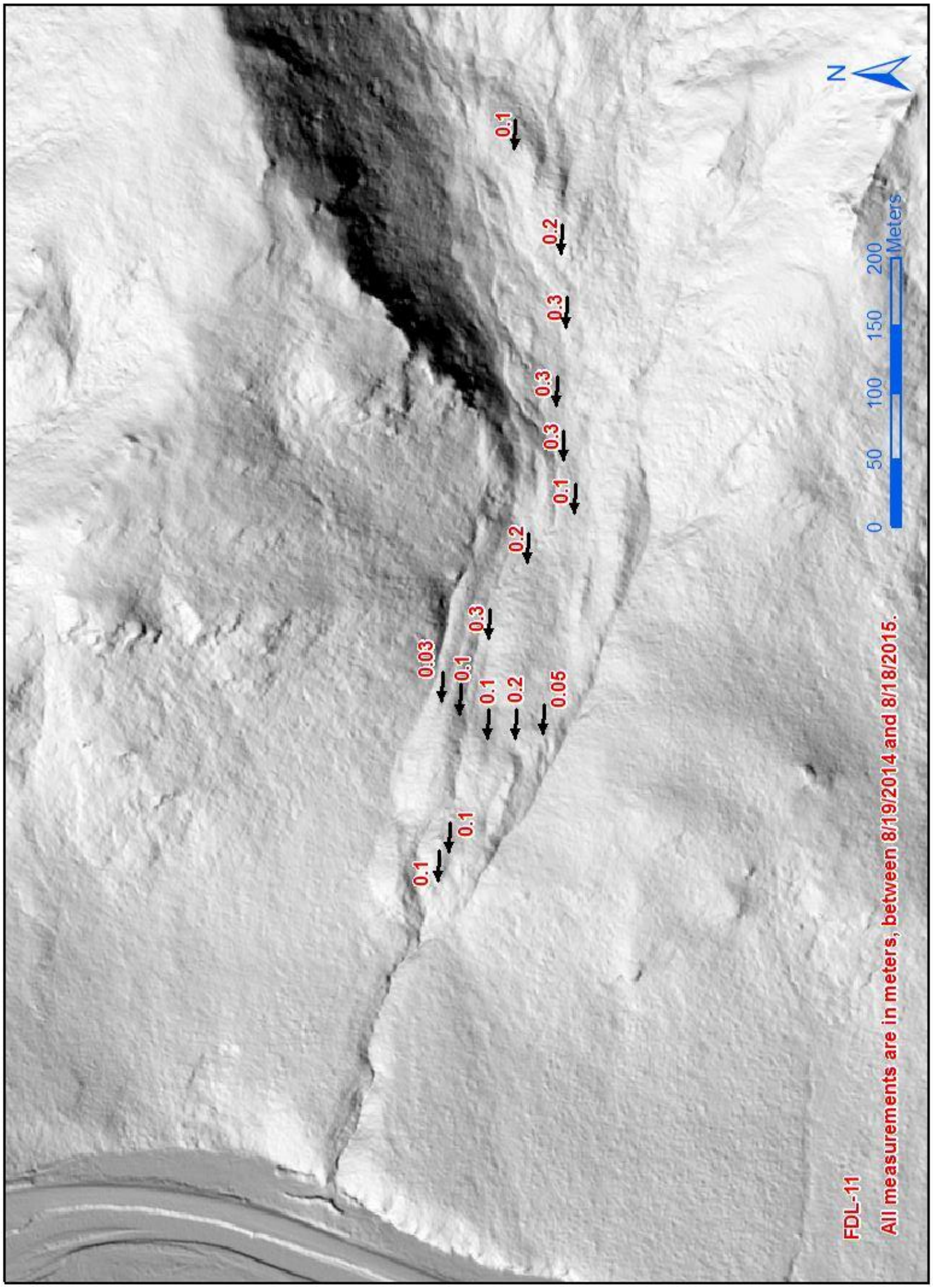

Figure A.1. Spatial distribution of yearly movement for FDL-11. Values shown are in meters and indicate the amount of movement measured between August 19, 2014 and August 18, 2015.

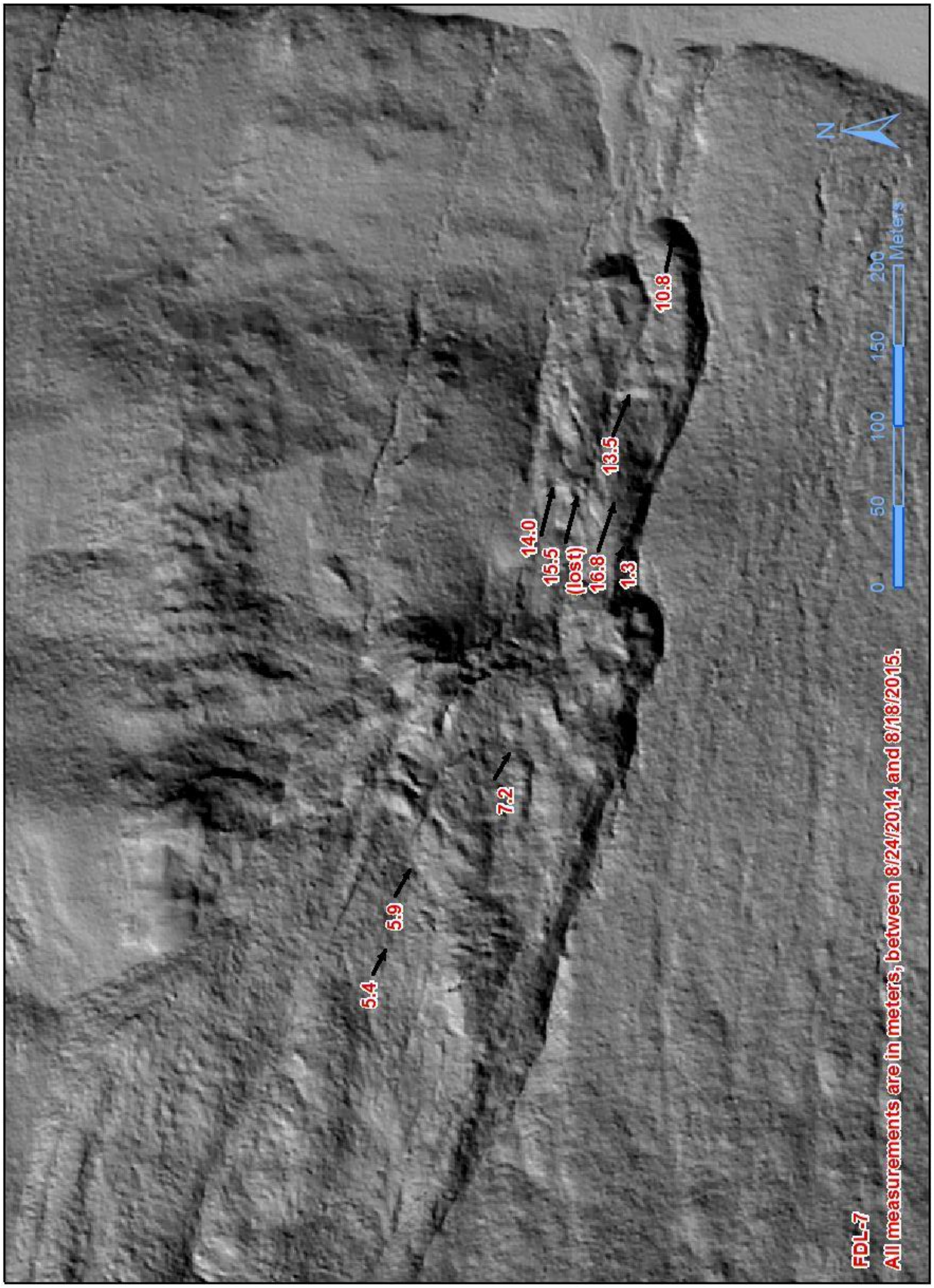

Figure A.2. Spatial distribution of yearly movement for FDL-7. Values shown are in meters and indicate the amount of movement measured between August 24, 2014 and August 18, 2015.

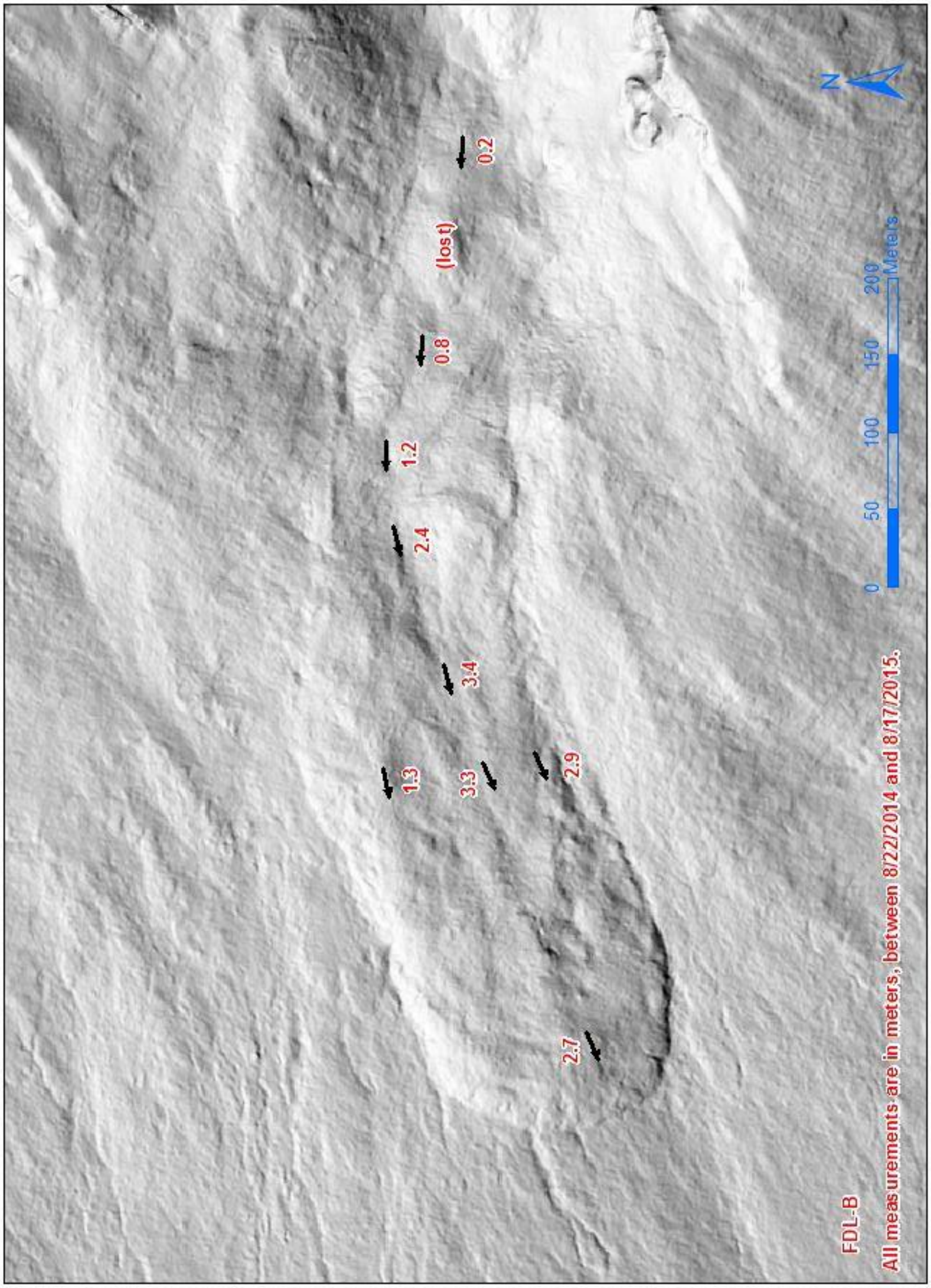

Figure A.3. Spatial distribution of yearly movement for FDL-B. Values shown are in meters and indicate the amount of movement measured between August 22, 2014 and August 17, 2015.

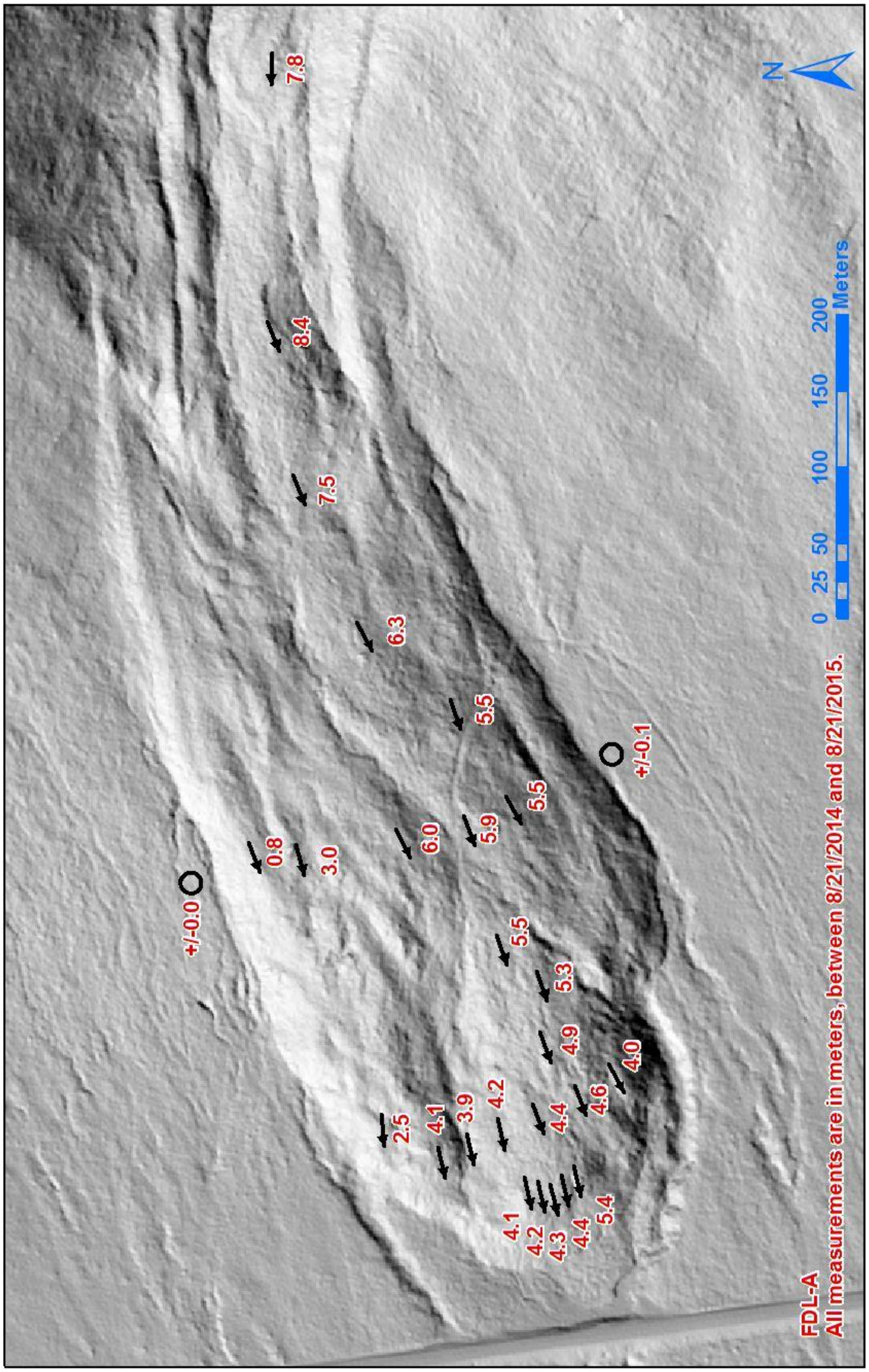

Figure A.4. Spatial distribution of yearly movement for FDL-A. Values shown are in meters and indicate the amount of movement measured between August 21, 2014 and August 21, 2015.

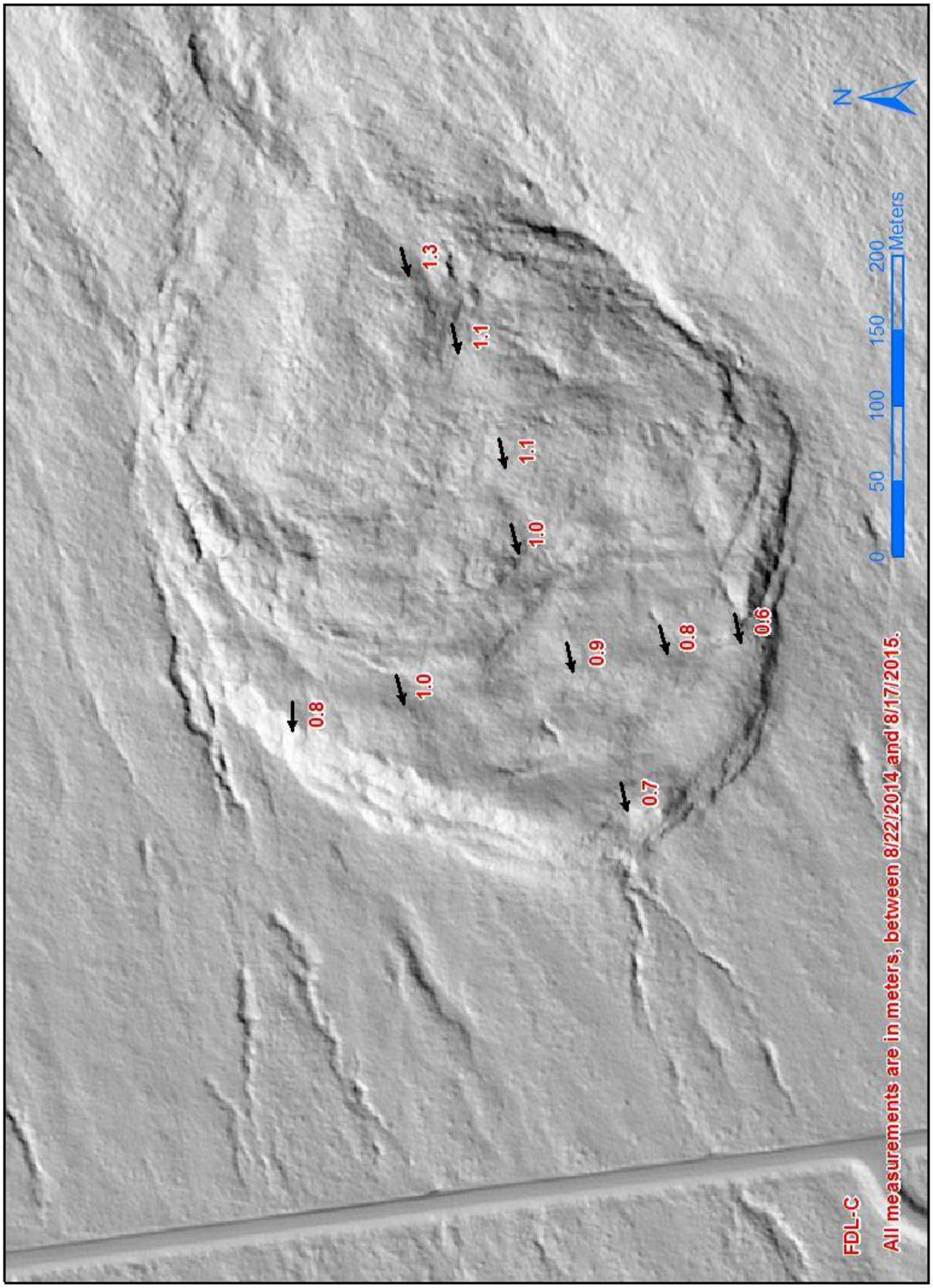

Figure A.5. Spatial distribution of yearly movement for FDL-C. Values shown are in meters and indicate the amount of movement measured between August 22, 2014 and August 17, 2015.

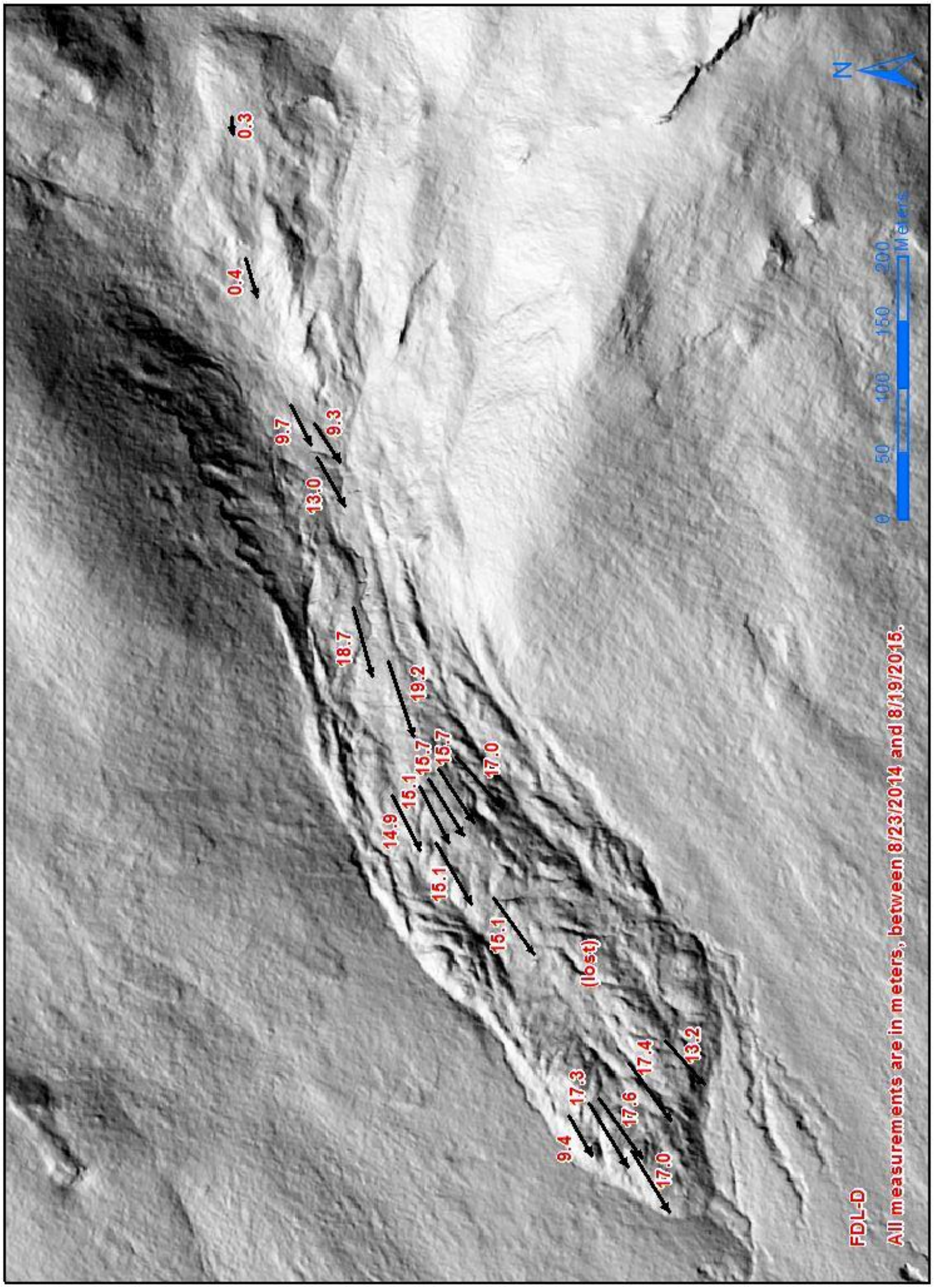

Figure A.6. Spatial distribution of yearly movement for FDL-D. Values shown are in meters and indicate the amount of movement measured between August 23, 2014 and August 19, 2015.

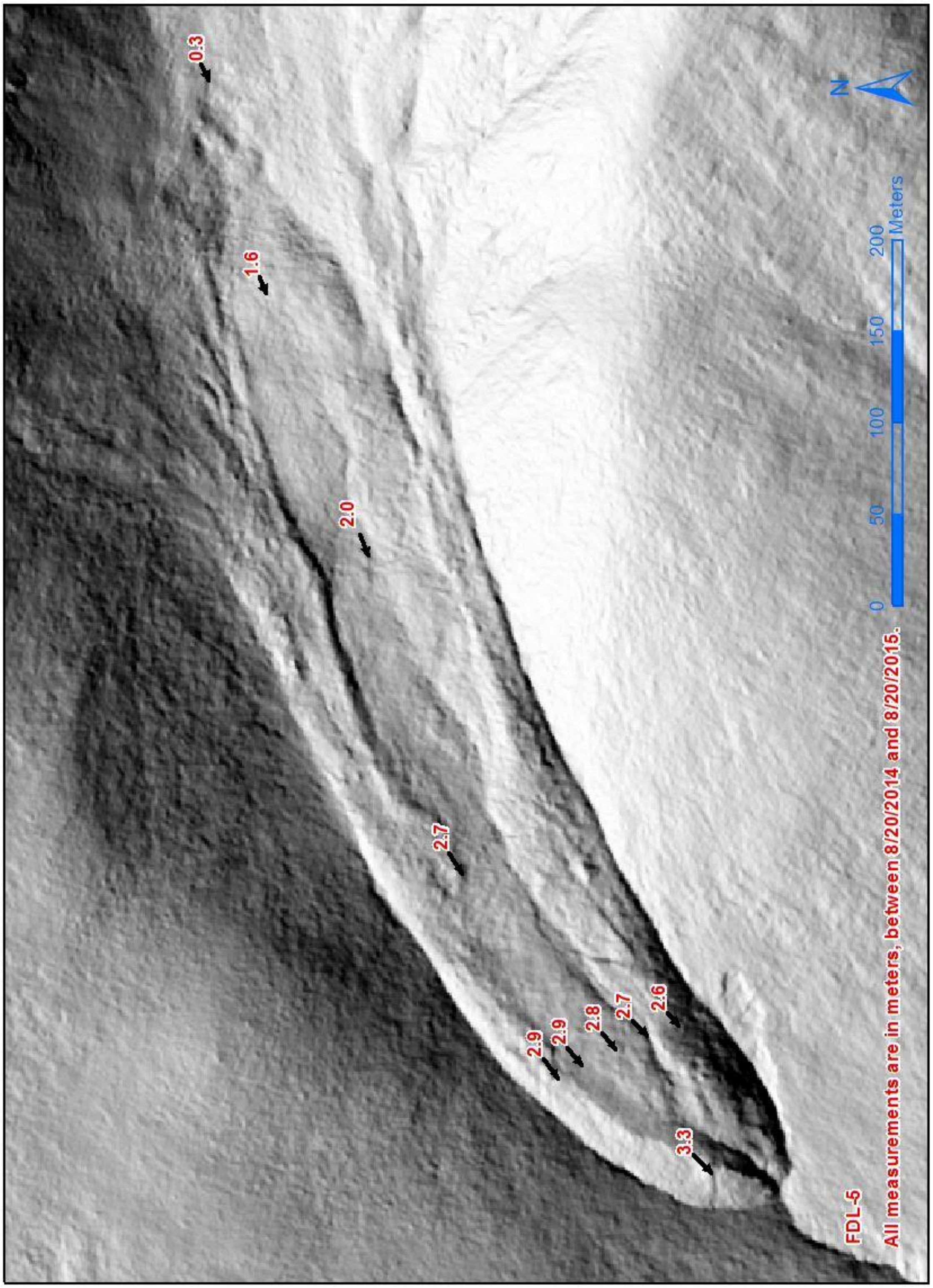

Figure A.7. Spatial distribution of yearly movement for FDL-5. Values shown are in meters and indicate the amount of movement measured between August 20, 2014 and August 20, 2015.

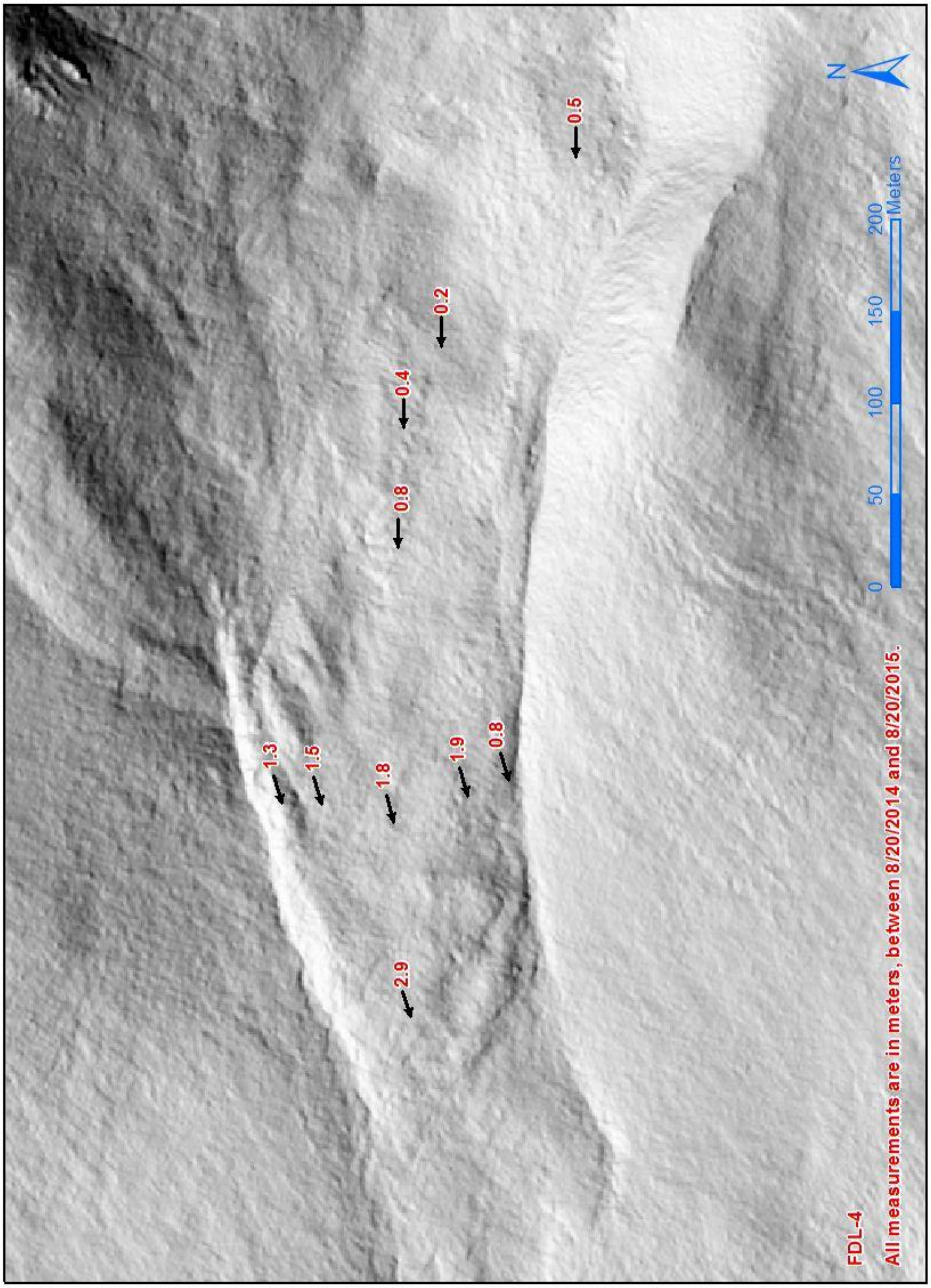

Figure A.8. Spatial distribution of yearly movement for FDL-4. Values shown are in meters and indicate the amount of movement measured between August 20, 2014 and August 20, 2015.

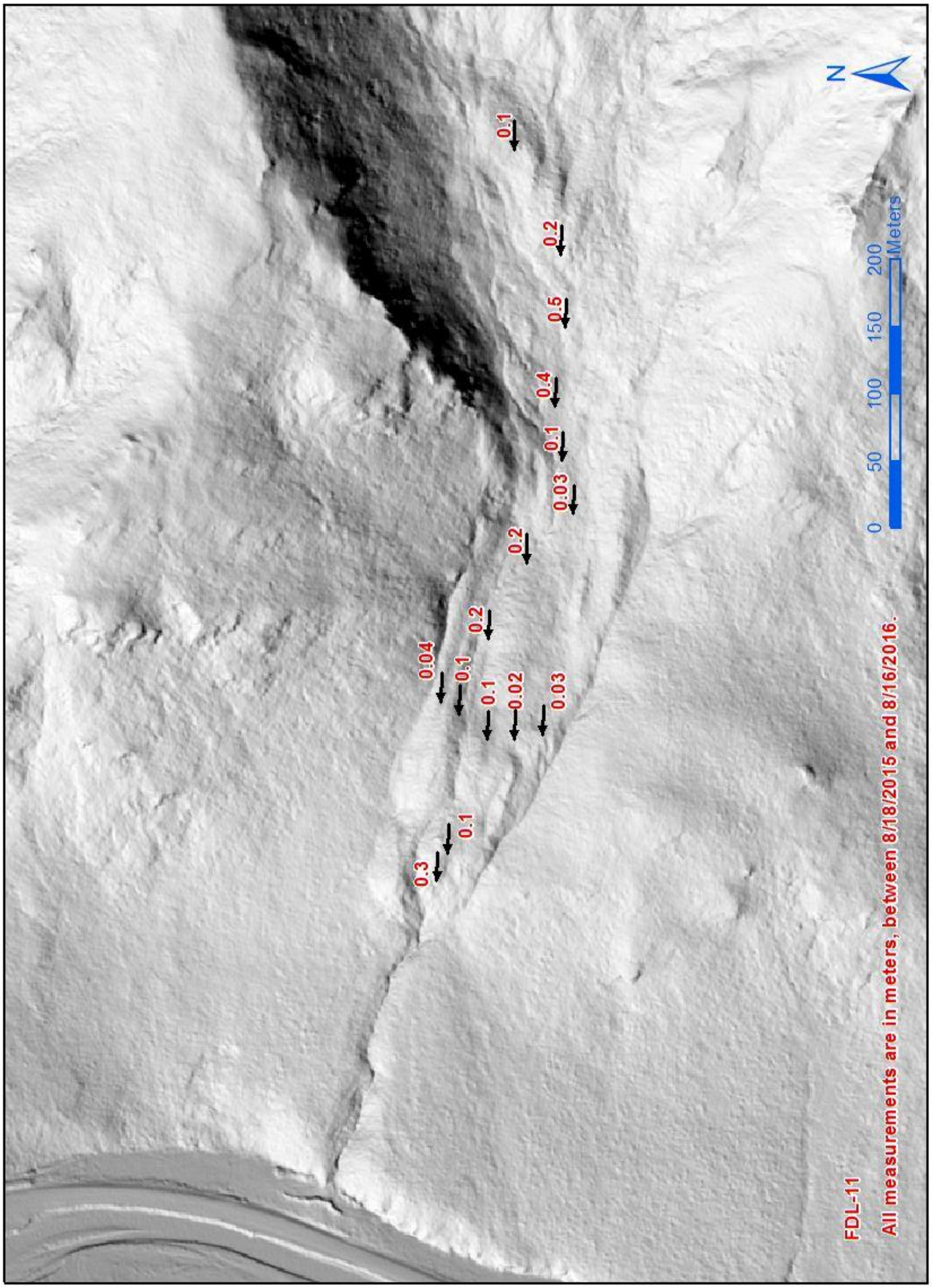

Figure A.9. Spatial distribution of yearly movement for FDL-11. Values shown are in meters and indicate the amount of movement measured between August 18, 2015 and August 16, 2016.

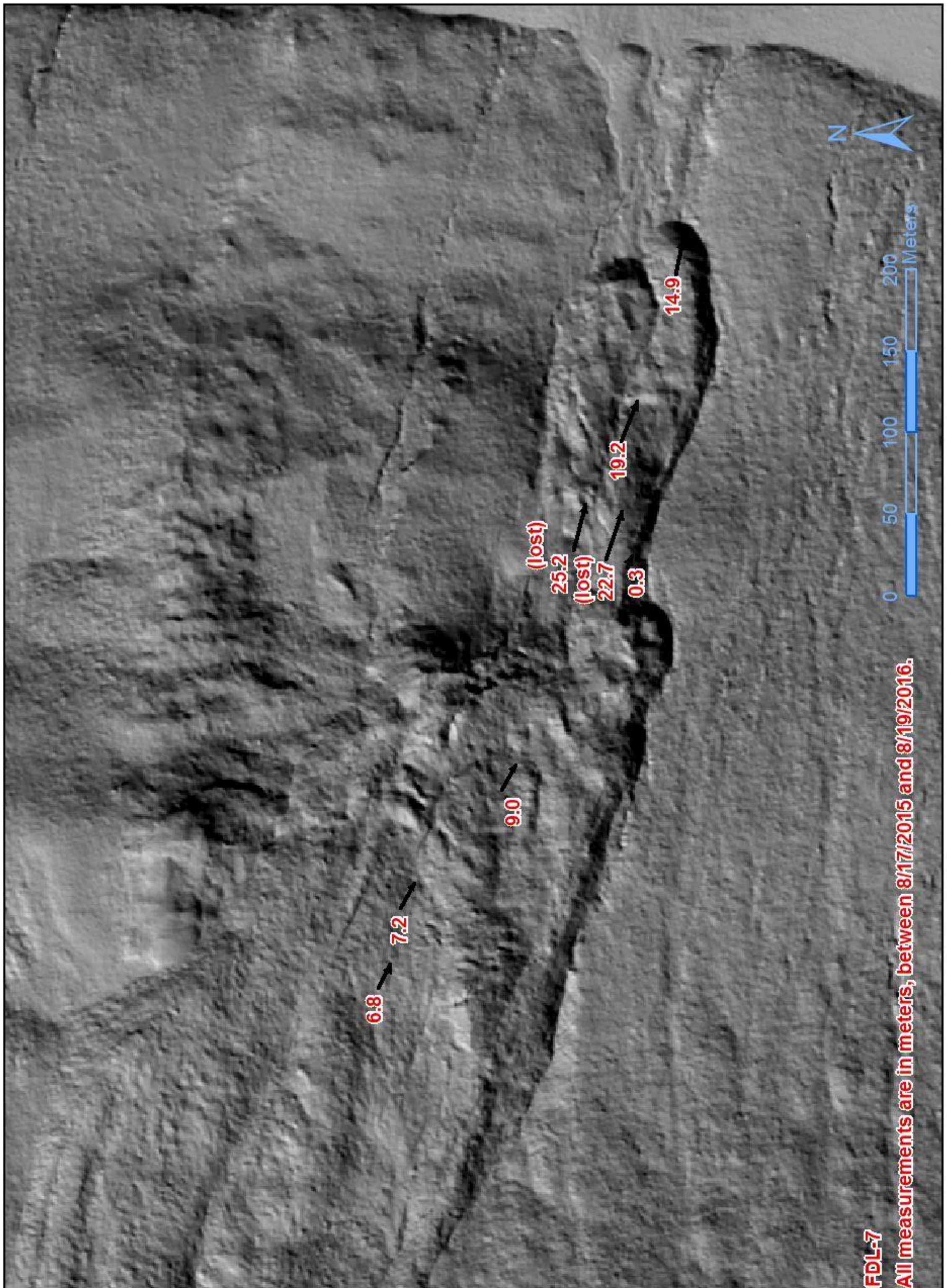

Figure A.10. Spatial distribution of yearly movement for FDL-7. Values shown are in meters and indicate the amount of movement measured between August 17, 2015 and August 19, 2016.

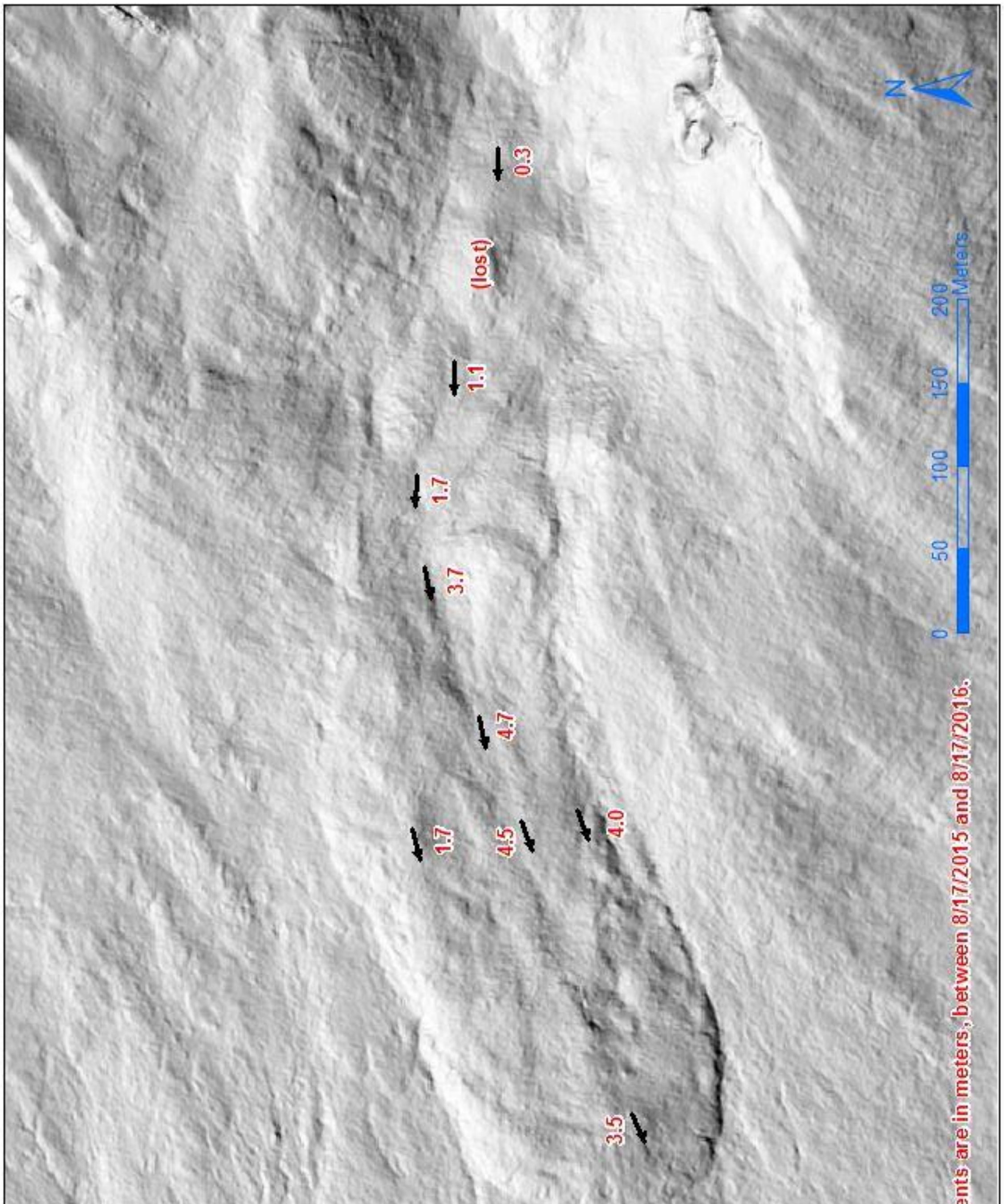

Figure A.11. Spatial distribution of yearly movement for FDL-B. Values shown are in meters and indicate the amount of movement measured between August 17, 2015 and August 17, 2016.

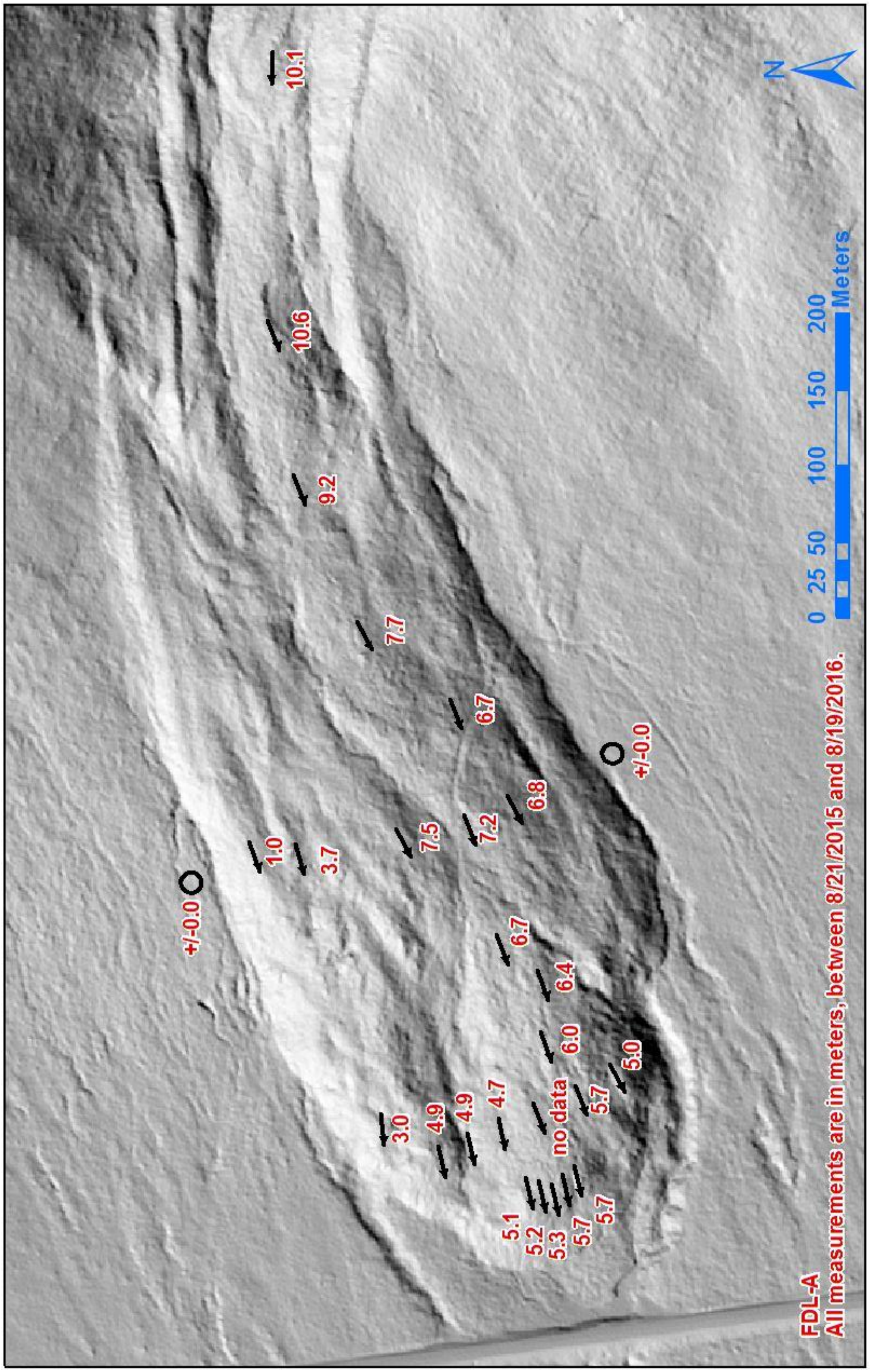

Figure A.12. Spatial distribution of yearly movement for FDL-A. Values shown are in meters and indicate the amount of movement measured between August 21, 2015 and August 19, 2016.

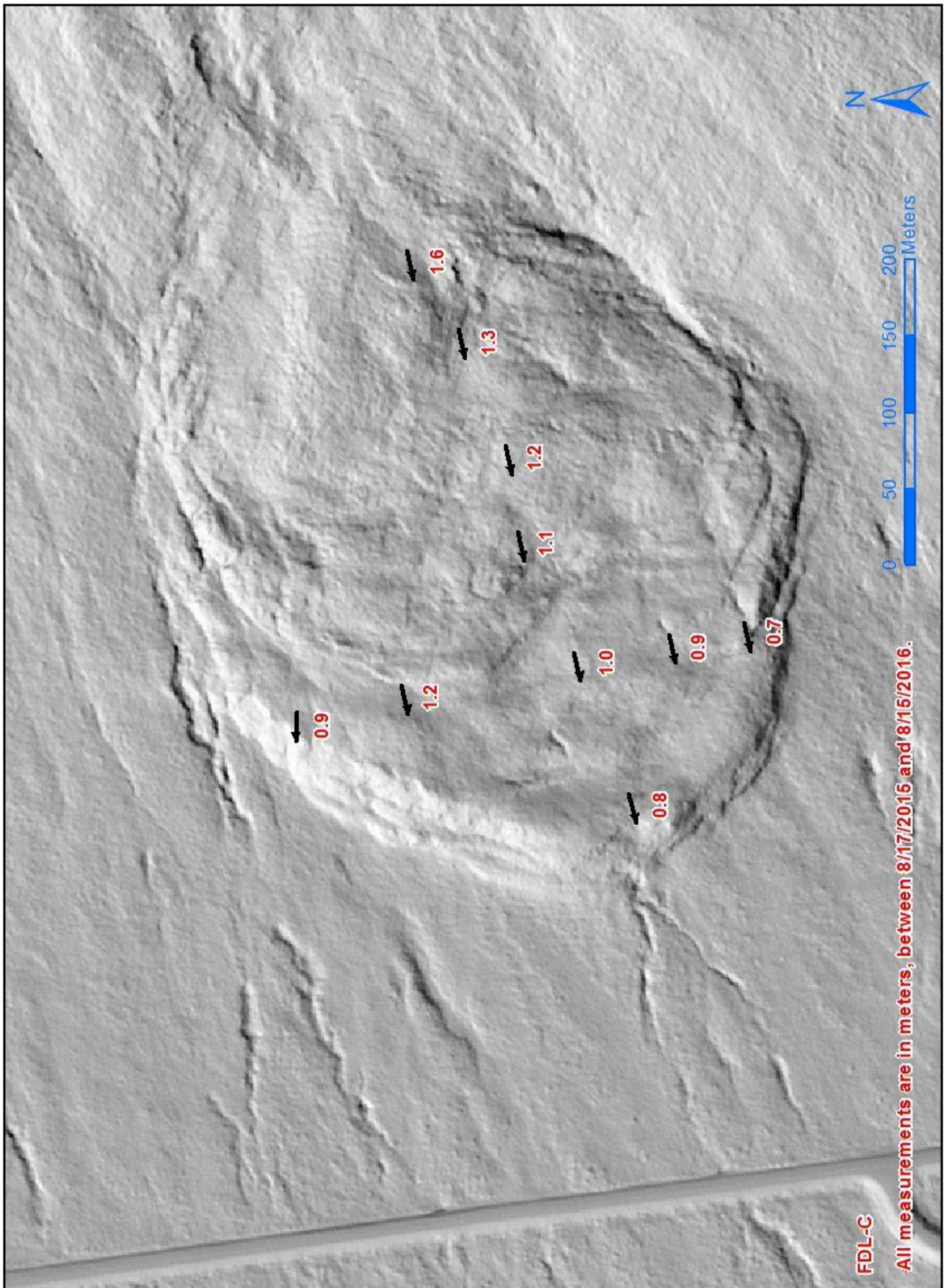

Figure A.13. Spatial distribution of yearly movement for FDL-C. Values shown are in meters and indicate the amount of movement measured between August 17, 2015 and August 15, 2016.

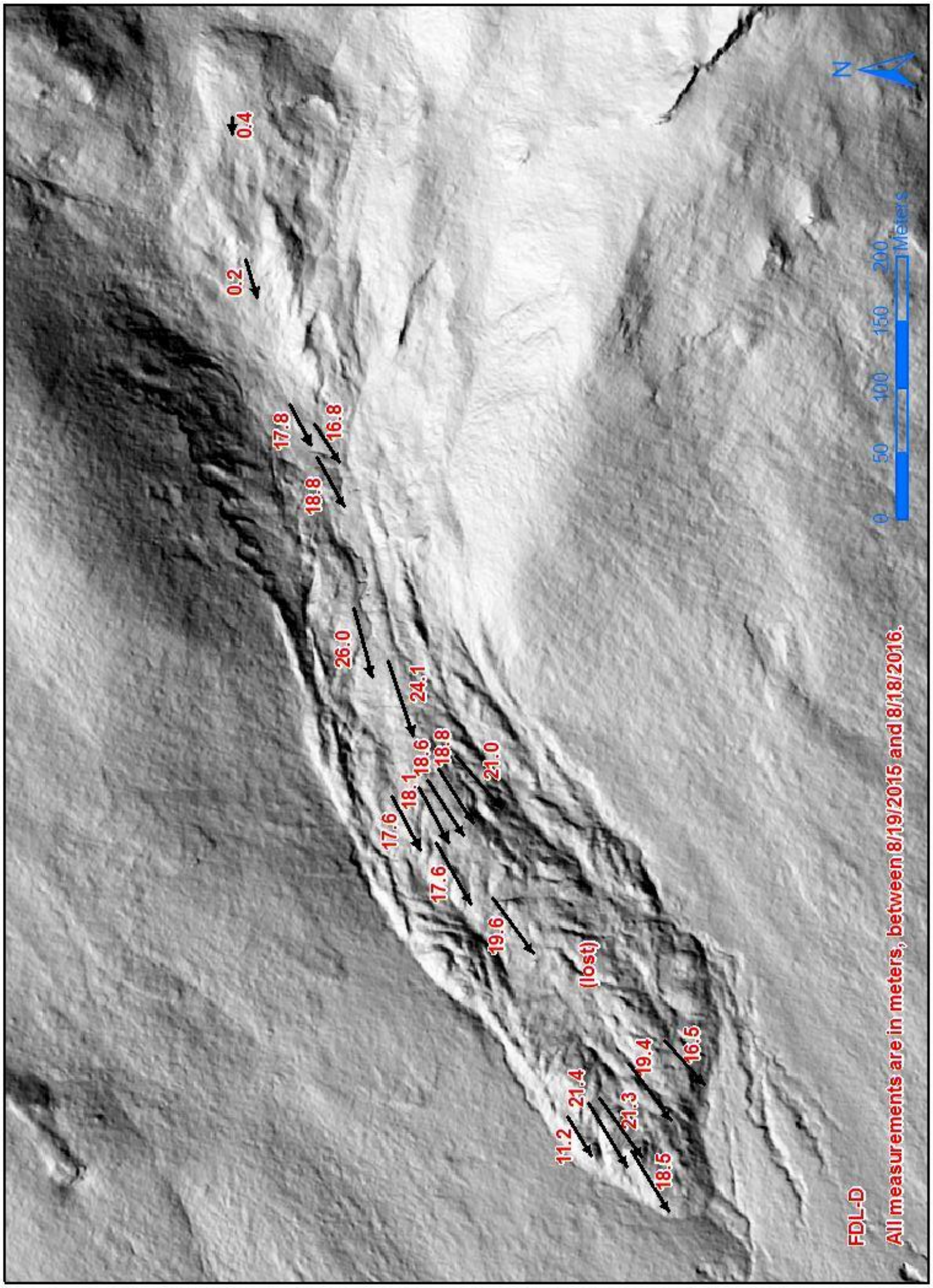

Figure A.14. Spatial distribution of yearly movement for FDL-D. Values shown are in meters and indicate the amount of movement measured between August 19, 2015 and August 18, 2016.

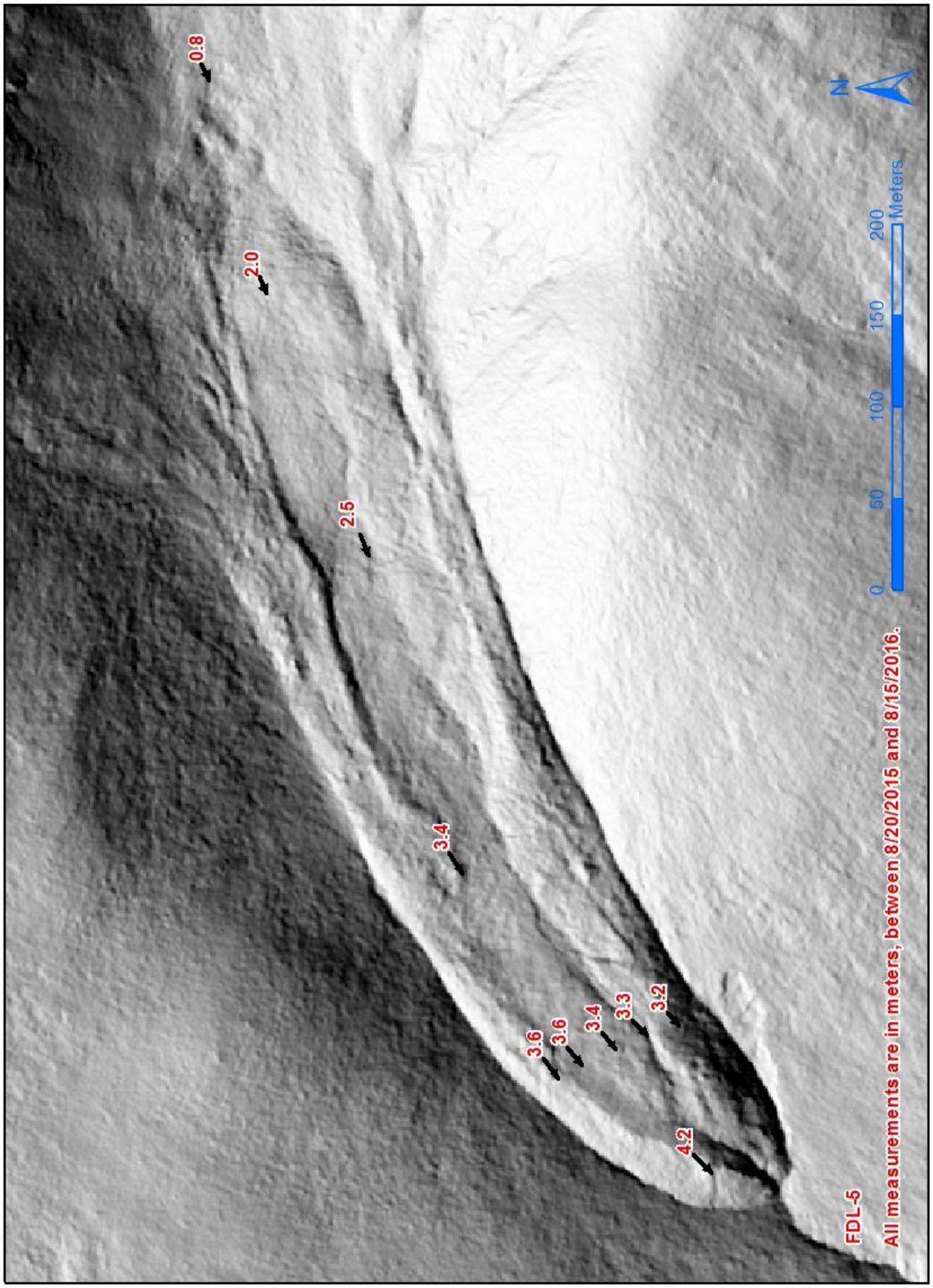

Figure A.15. Spatial distribution of yearly movement for FDL-5. Values shown are in meters and indicate the amount of movement measured between August 20, 2015 and August 15, 2016.

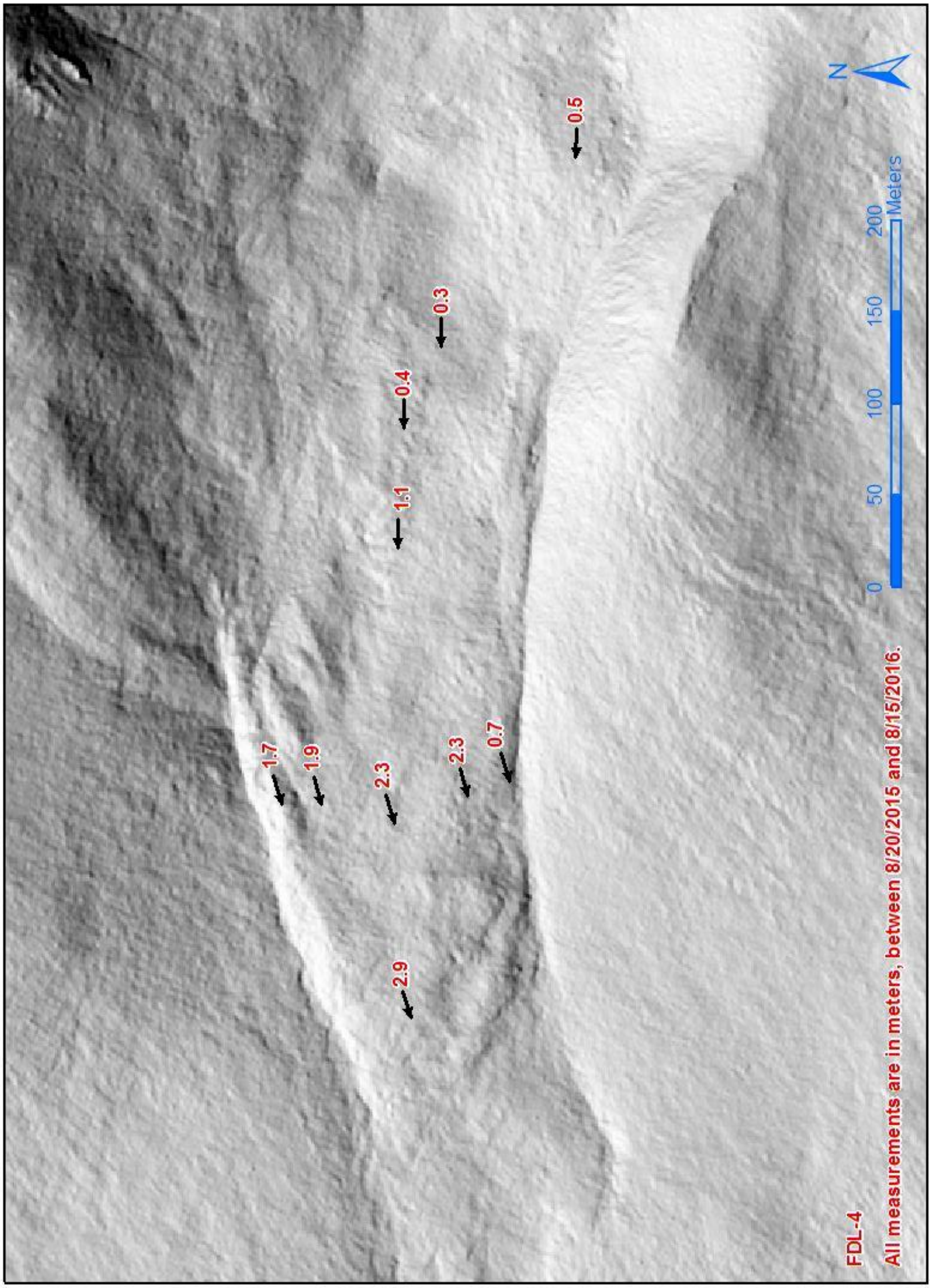

Figure A.16. Spatial distribution of yearly movement for FDL-4. Values shown are in meters and indicate the amount of movement measured between August 20, 2015 and August 15, 2016.

APPENDIX B: DEMs of Difference (DoD) for the eight investigated FDLs

The following figures are arranged in geographic order, presenting the FDLs from north to south within the AOI.

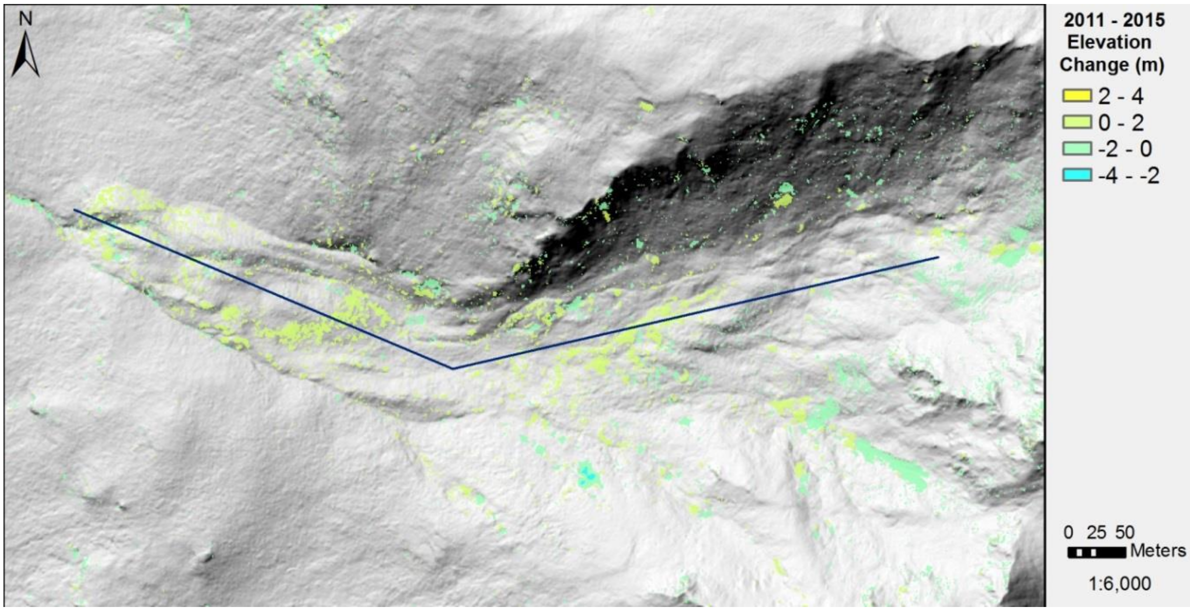

Figure B.1. DEM of Difference (DoD) for FDL-11, illustrating magnitude of vertical displacement from 2011 and 2015. Dark blue line indicates location of the profile in Figure B.2.

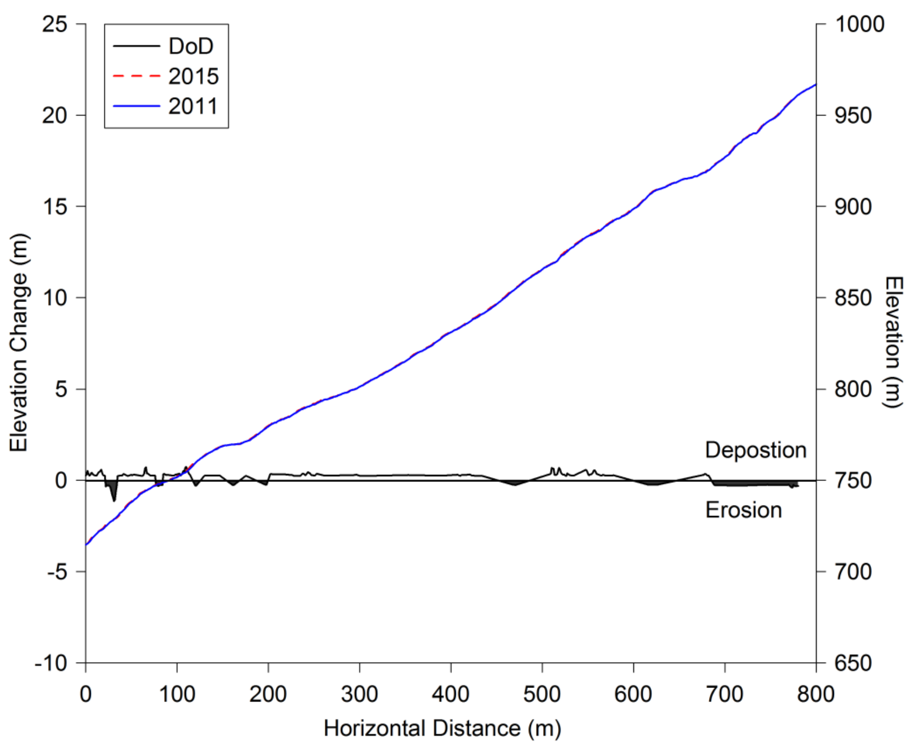

Figure B.2. Longitudinal profile of FDL-11 with a 2:1 vertical exaggeration (blue and red-dashed curves). Change in elevation is illustrated below the longitudinal profile.

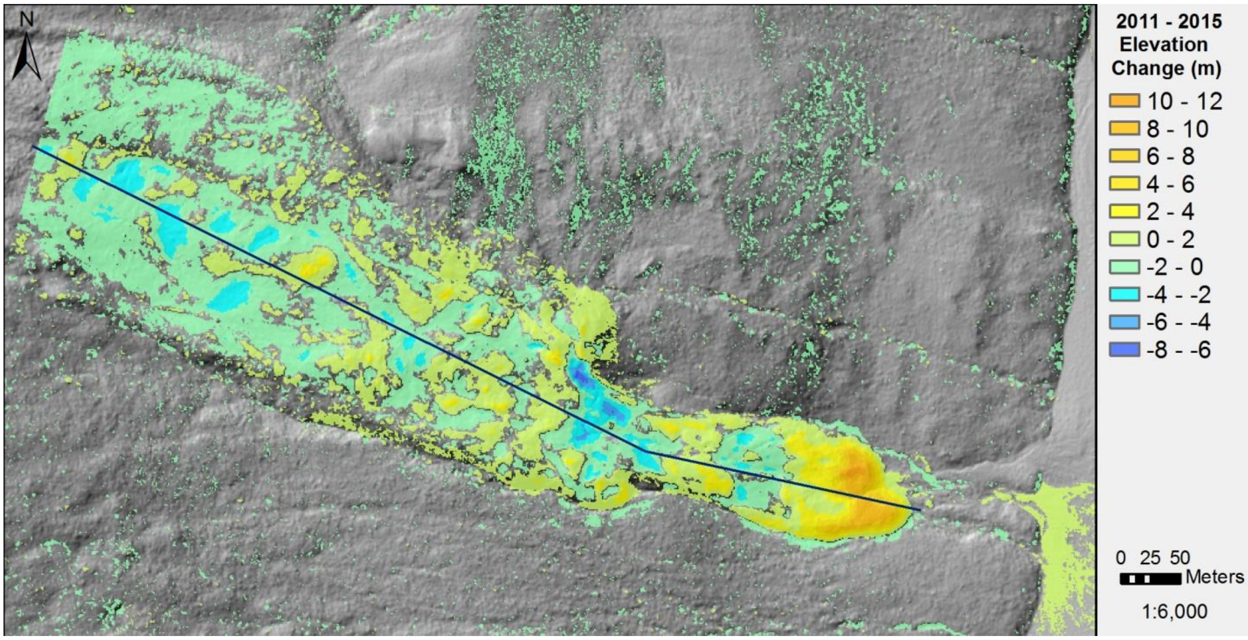

Figure B.3. DEM of Difference (DoD) for FDL-7, illustrating magnitude of vertical displacement from 2011 and 2015. Dark blue line indicates location of the profile in Figure B.4.

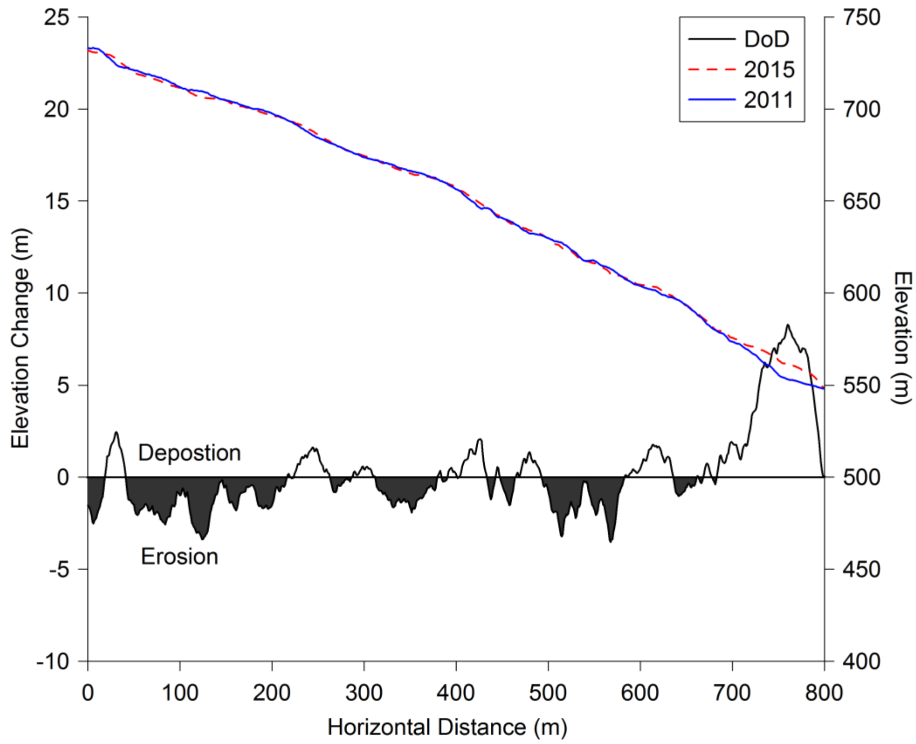

Figure B.4. Longitudinal profile of FDL-7 with a 2:1 vertical exaggeration (blue and red-dashed curves). Change in elevation is illustrated below the longitudinal profile.

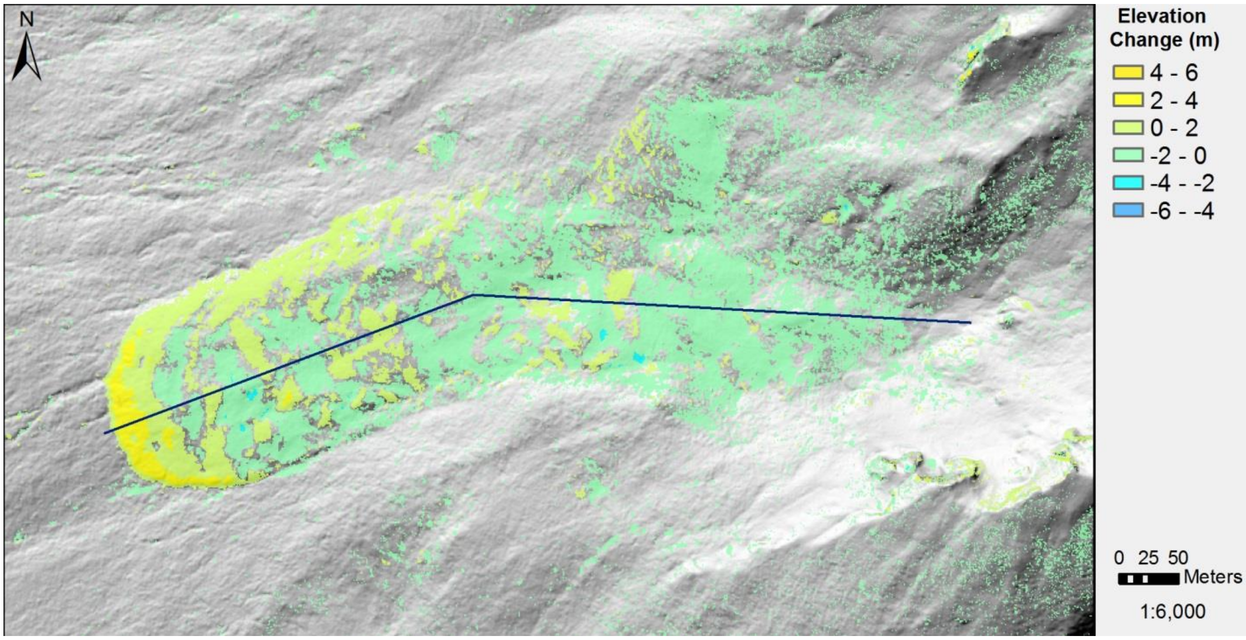

Figure B.5. DEM of Difference (DoD) for FDL-B, illustrating magnitude of vertical displacement from 2011 and 2015. Dark blue line indicates location of the profile in Figure B.6.

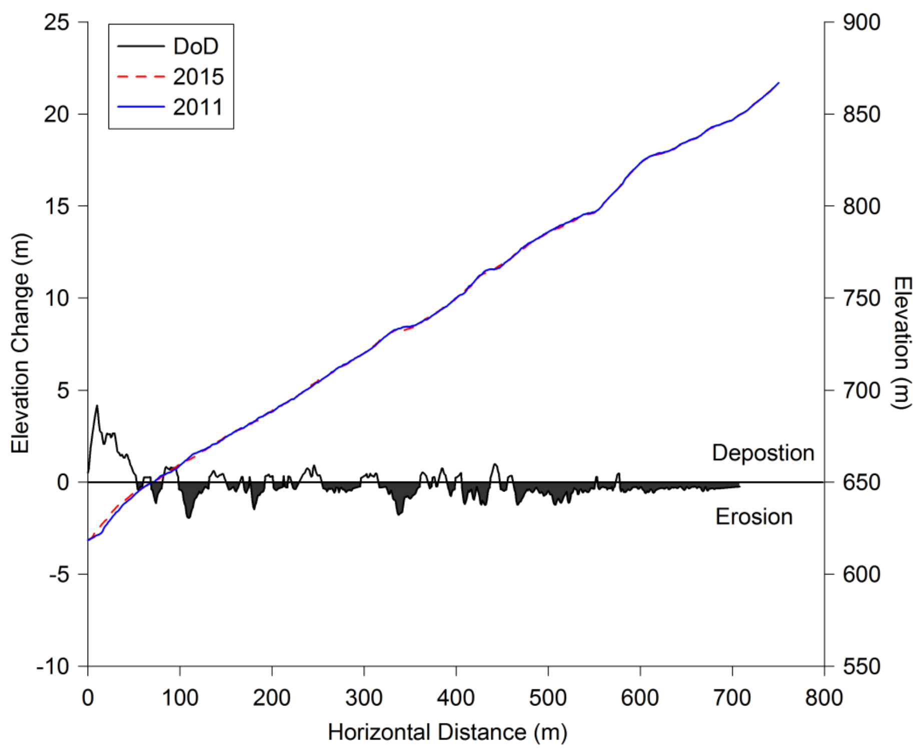

Figure B.6. Longitudinal profile of FDL-B with a 2:1 vertical exaggeration (blue and red-dashed curves). Change in elevation is illustrated below the longitudinal profile.

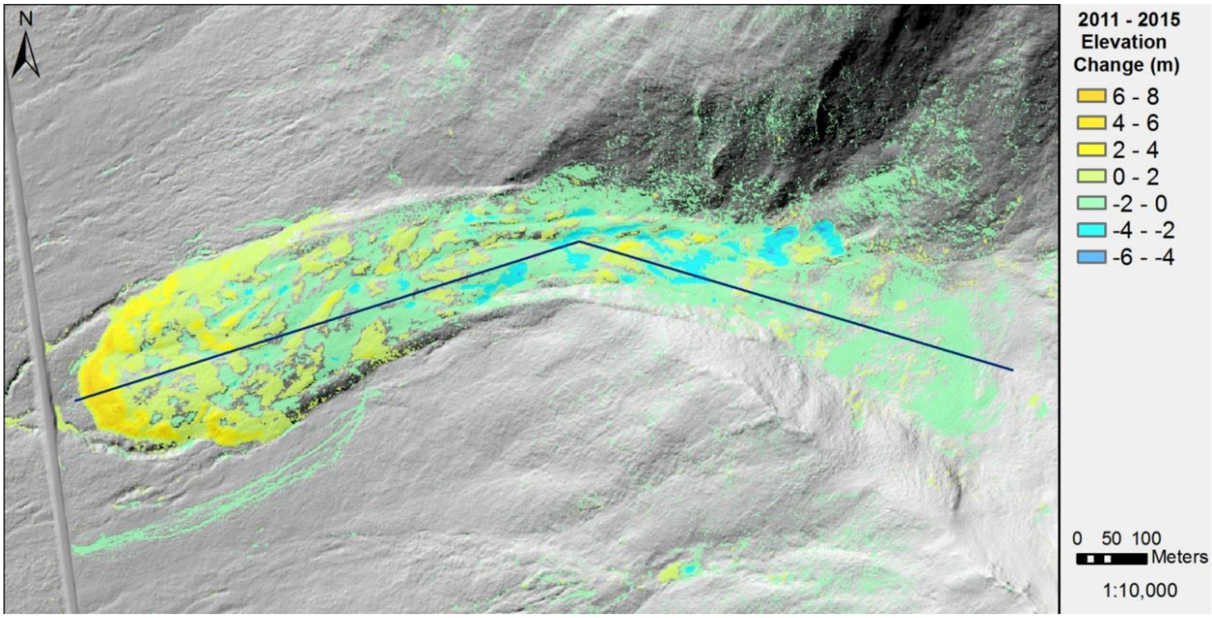

Figure B.7. DEM of Difference (DoD) for FDL-A, illustrating magnitude of vertical displacement from 2011 to 2015. Dark blue line indicates location of the profile in Figure B.8.

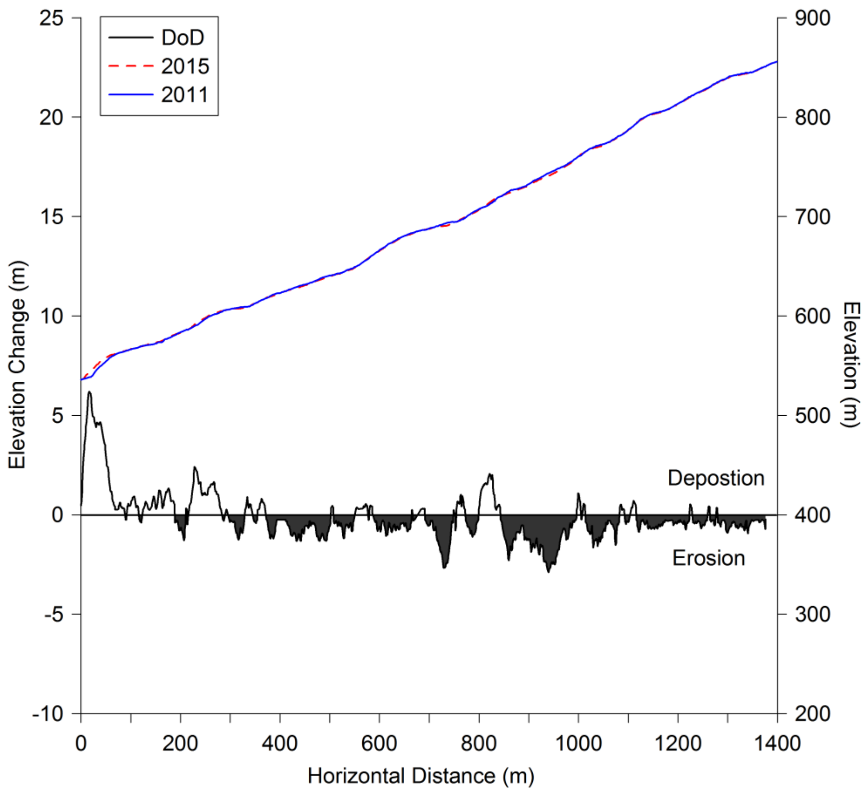

Figure B.8. Longitudinal profile of FDL-A with a 2:1 vertical exaggeration (blue and red-dashed curves). Change in elevation is illustrated below the longitudinal profile.

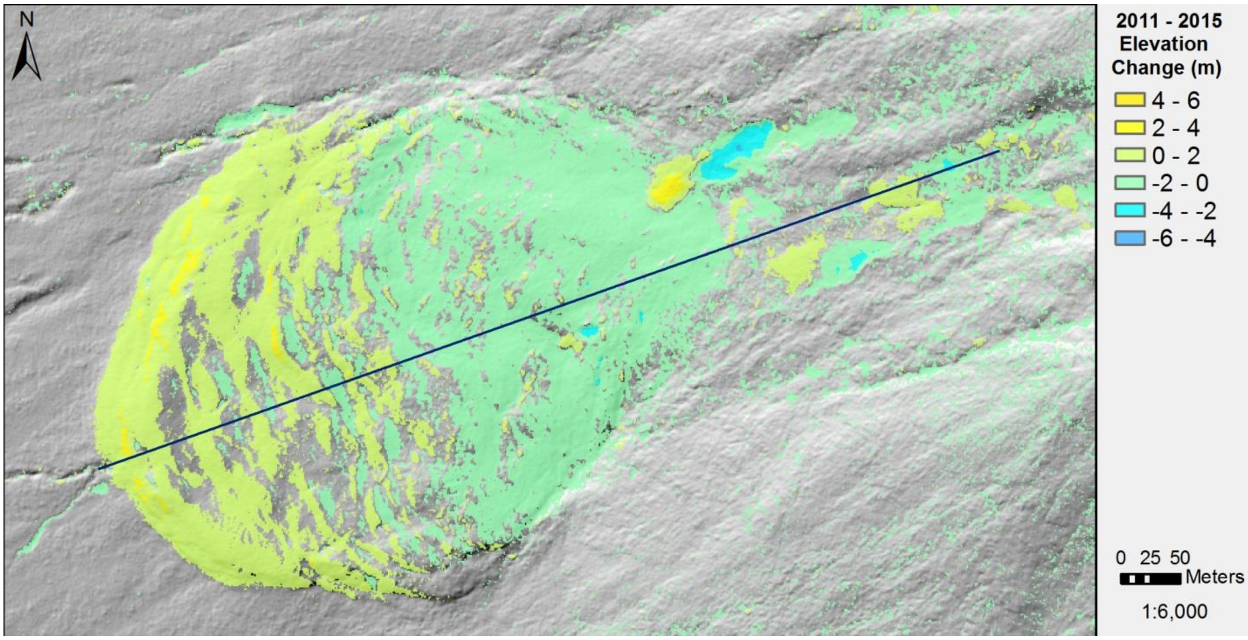

Figure B.9. DEM of Difference (DoD) for FDL-C, illustrating magnitude of vertical displacement from 2011 to 2015. Dark blue line indicates location of the profile in Figure B.10.

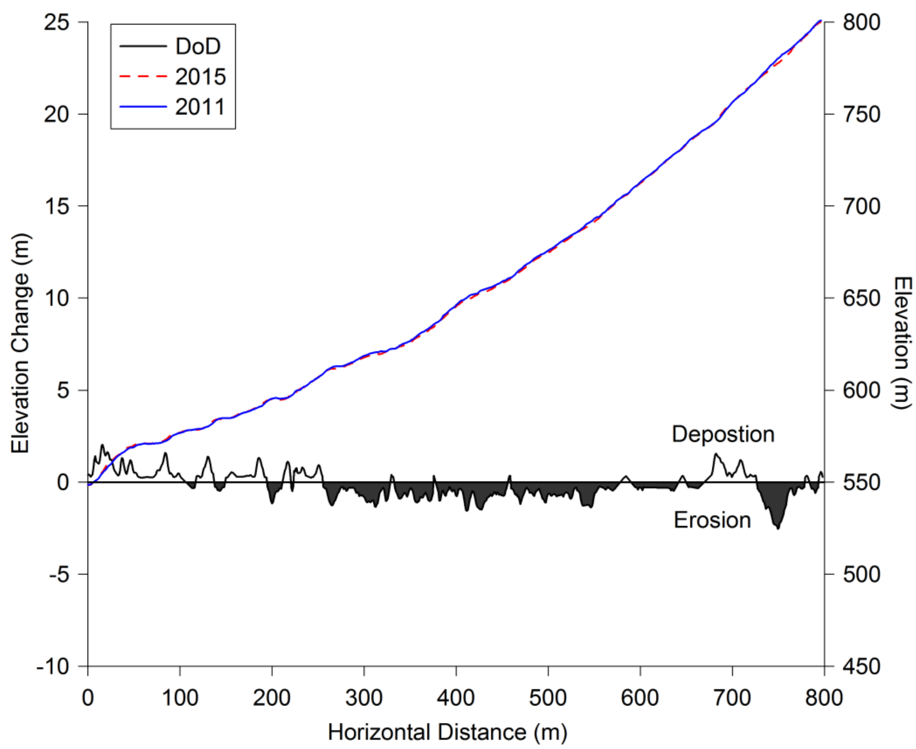

Figure B.10. Longitudinal profile of FDL-C with a 2:1 vertical exaggeration (blue and red-dashed curves). Change in elevation is illustrated below the longitudinal profile.

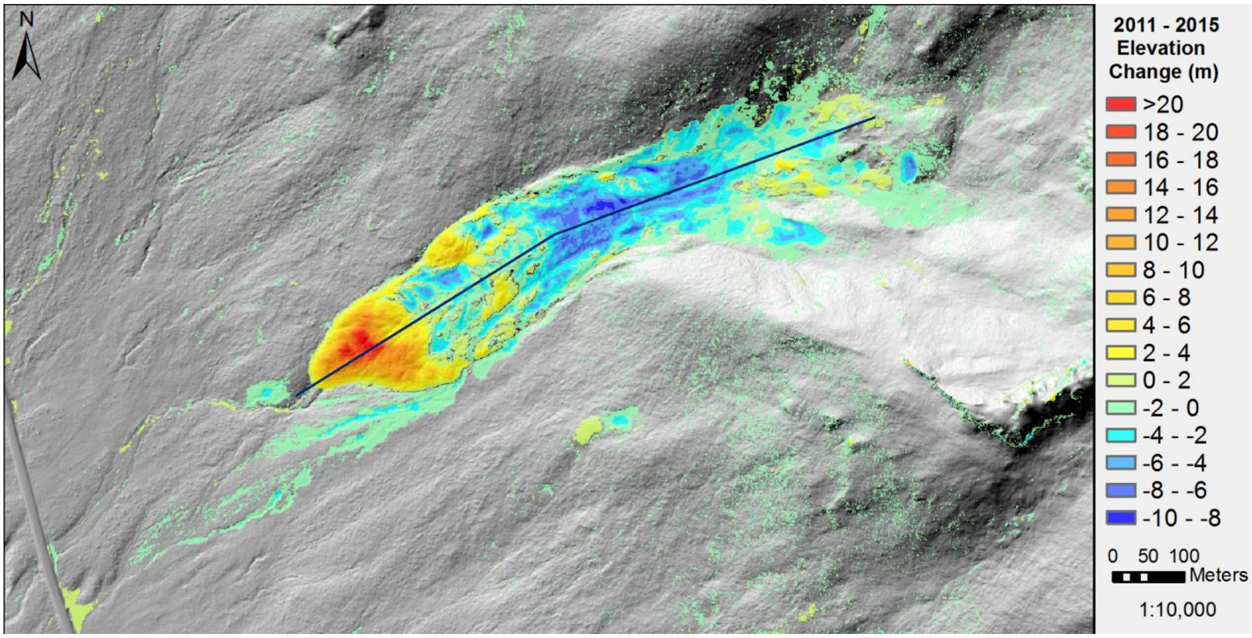

Figure B.11. DEM of Difference (DoD) for FDL-D, illustrating magnitude of vertical displacement from 2011 to 2015. Dark blue line indicates location of the profile in Figure B.12.

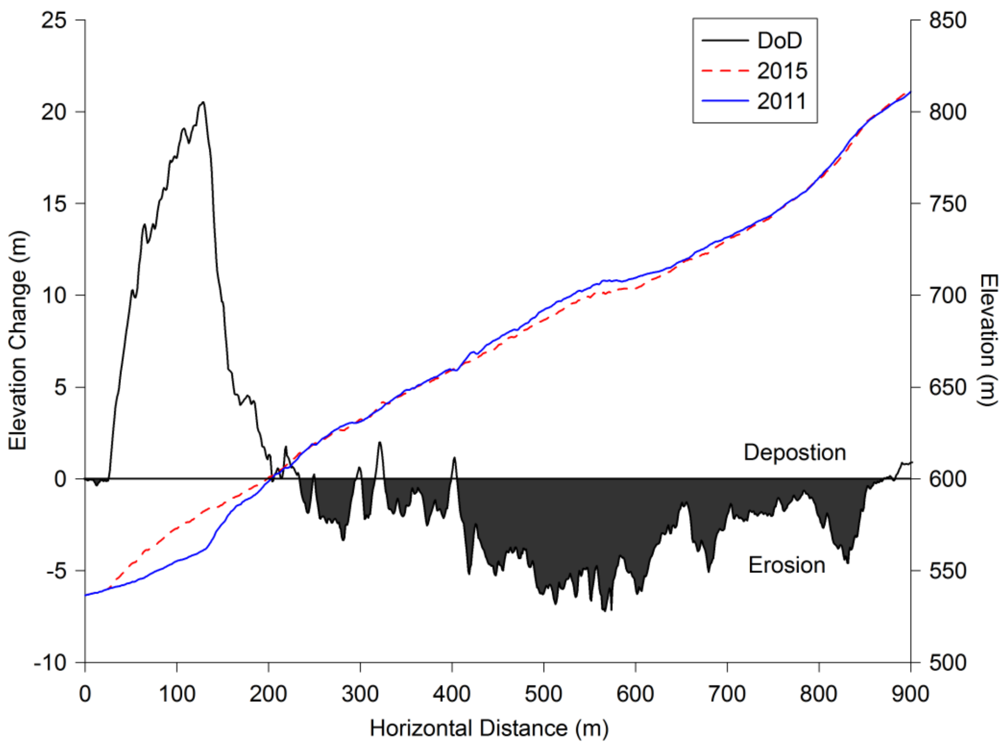

Figure B.12. Longitudinal profile of FDL-D with a 2:1 vertical exaggeration (blue and red-dashed curves). Change in elevation is illustrated below the longitudinal profile.

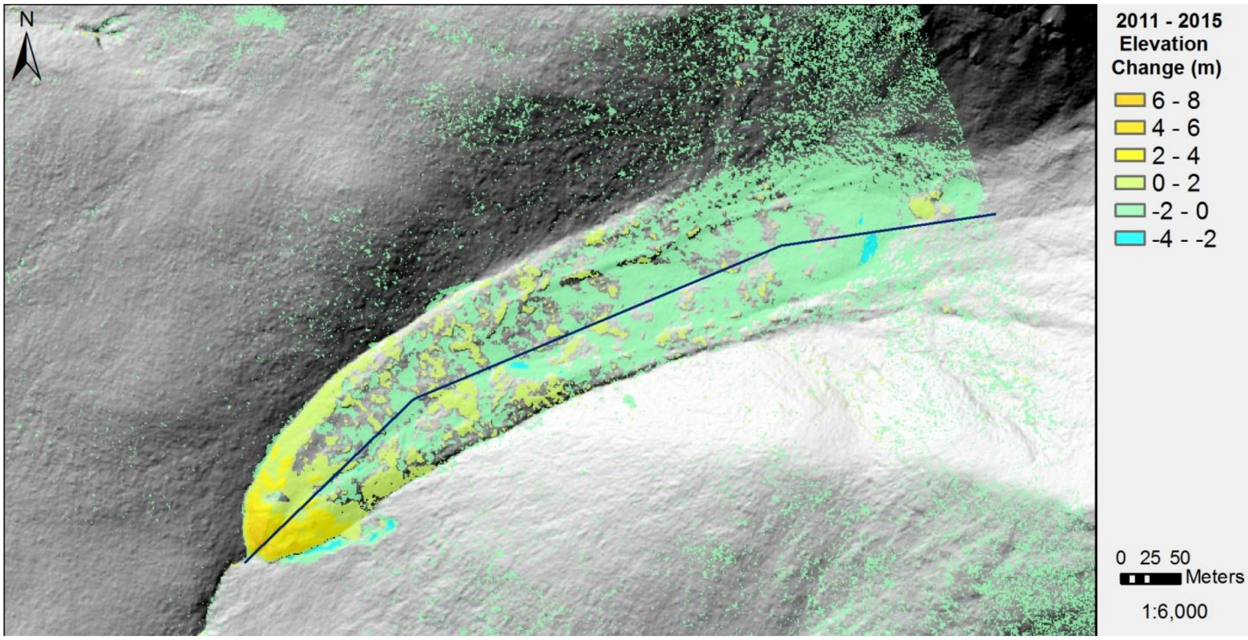

Figure B.13. DEM of Difference (DoD) for FDL-5, illustrating magnitude of vertical displacement from 2011 to 2015. Dark blue line indicates location of the profile in Figure B.14.

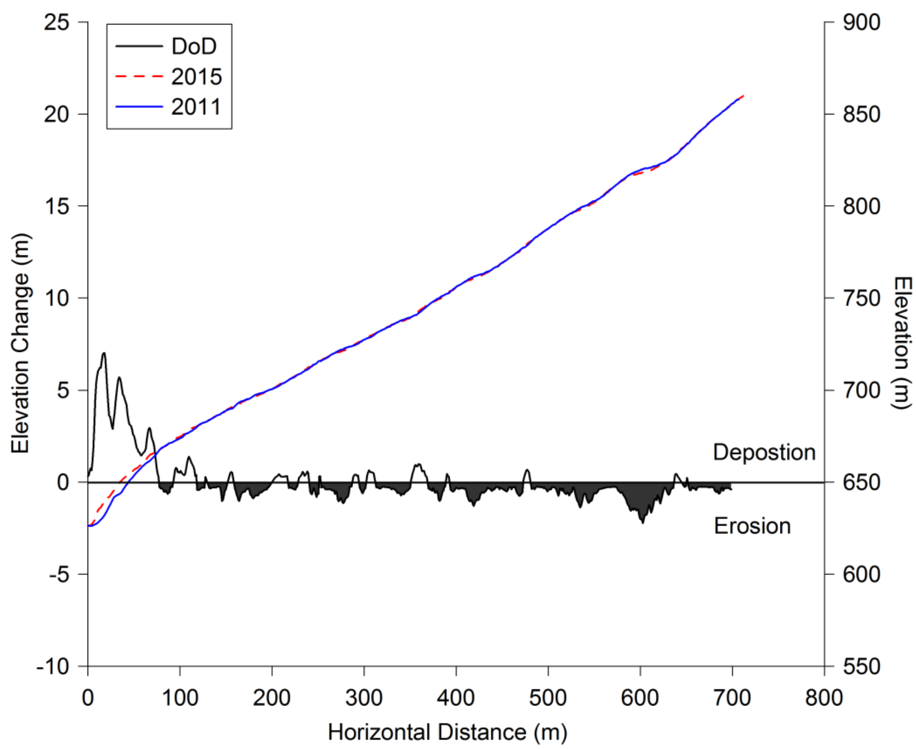

Figure B.14. Longitudinal profile of FDL-5 with a 2:1 vertical exaggeration (blue and red-dashed curves). Change in elevation is illustrated below the longitudinal profile.

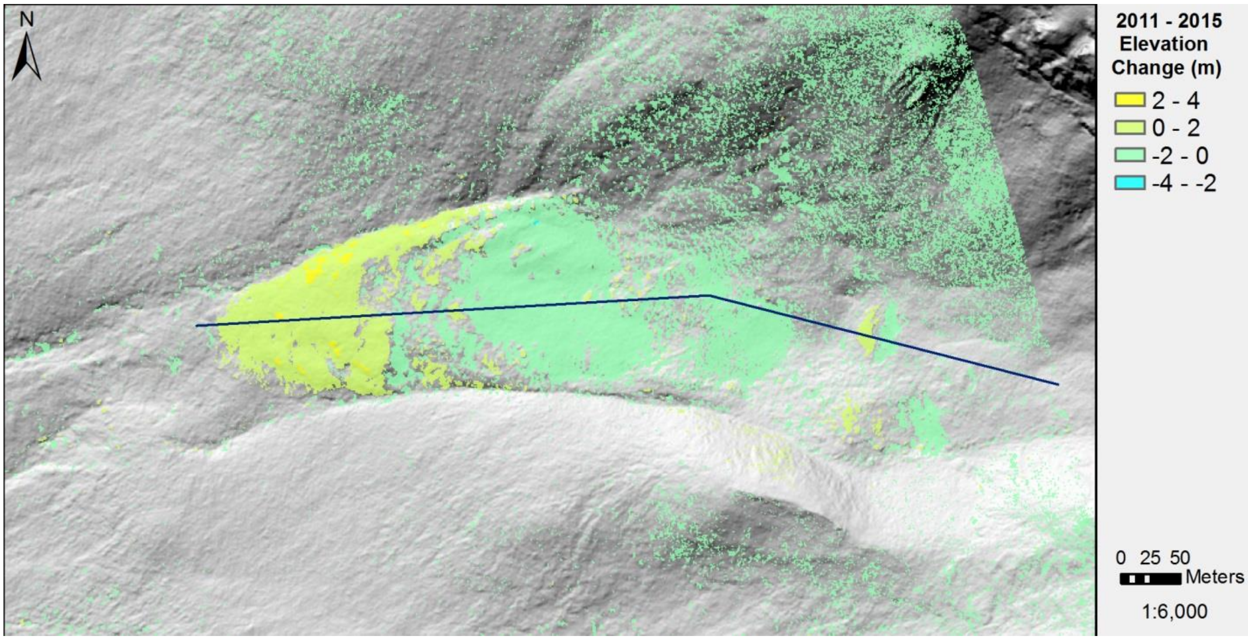

Figure B.15. DEM of Difference (DoD) for FDL-4, illustrating magnitude of vertical displacement from 2011 to 2015. Dark blue line indicates location of the profile in Figure B.16.

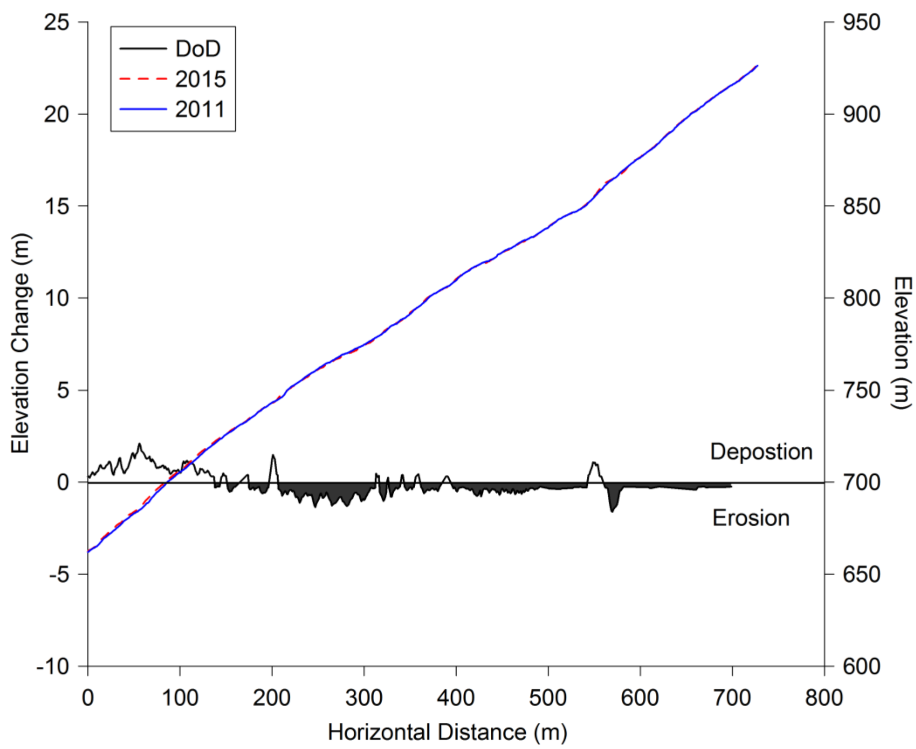

Figure B.16. Longitudinal profile of FDL-4 with a 2:1 vertical exaggeration (blue and red-dashed curves). Change in elevation is illustrated below the longitudinal profile.

APPENDIX C: Maps of Catchment Slope and Aspect Distribution for Investigated NDLs and Adjacent FDLs

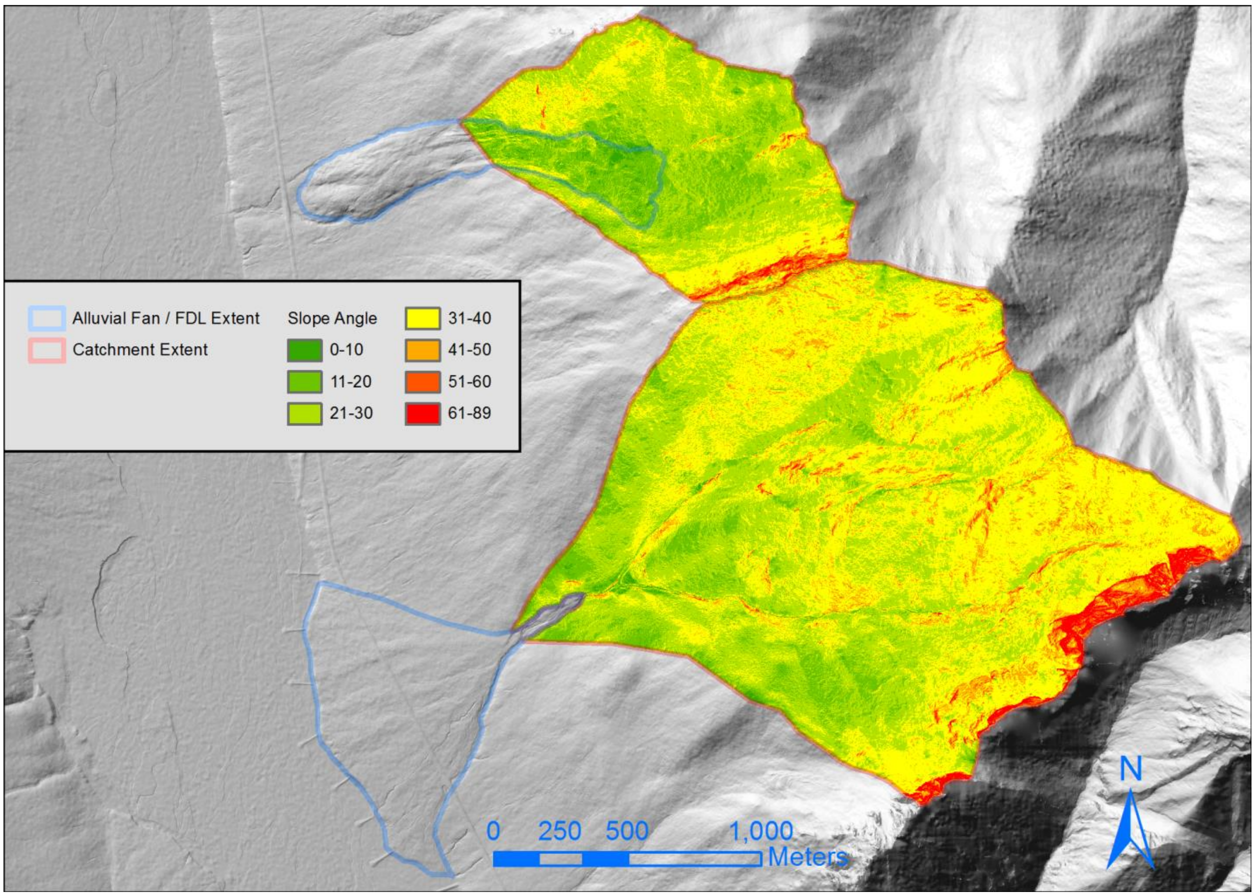

Figure C.1. Slope angle distributions of FDL-A and NDL-2 catchments.

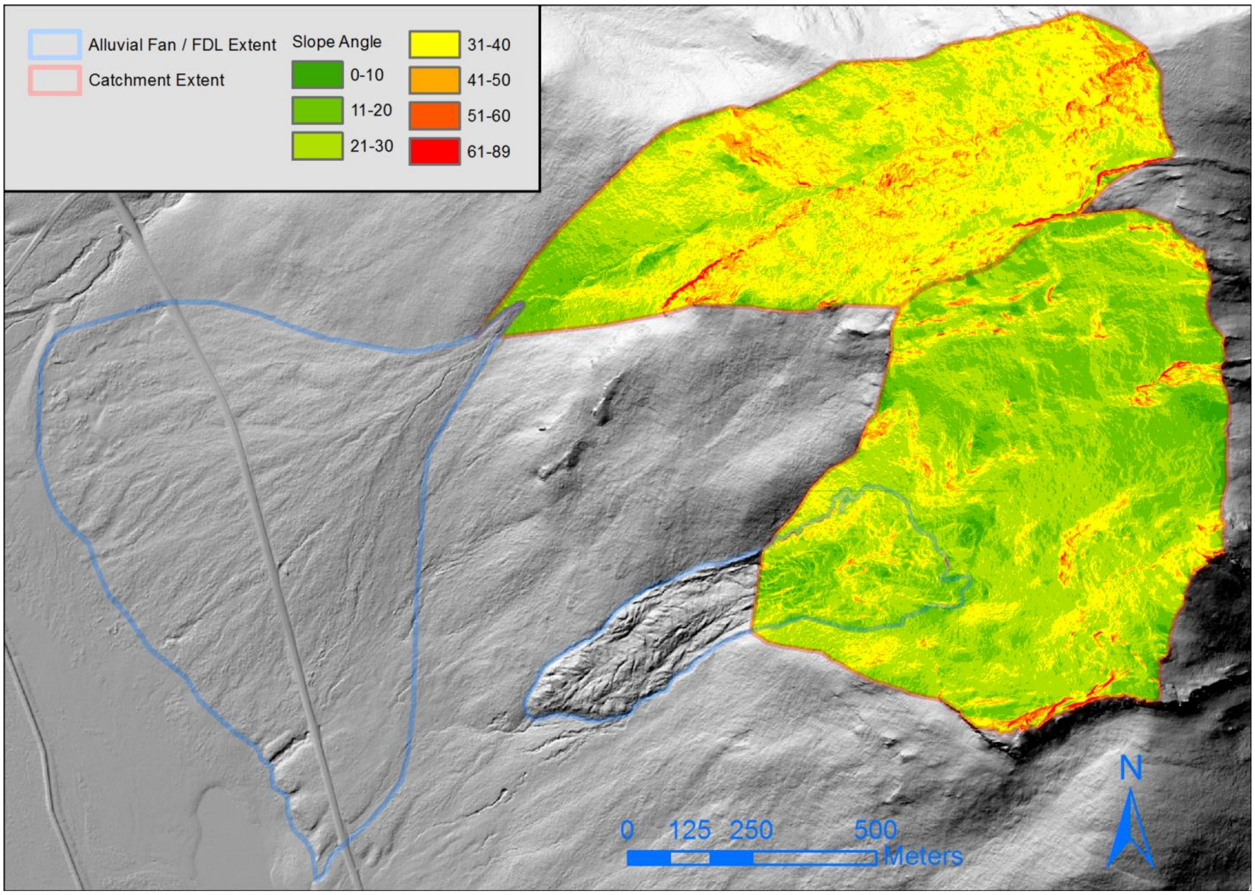

Figure C.2. Slope angle distributions of NDL-3 and FDL-D catchments.

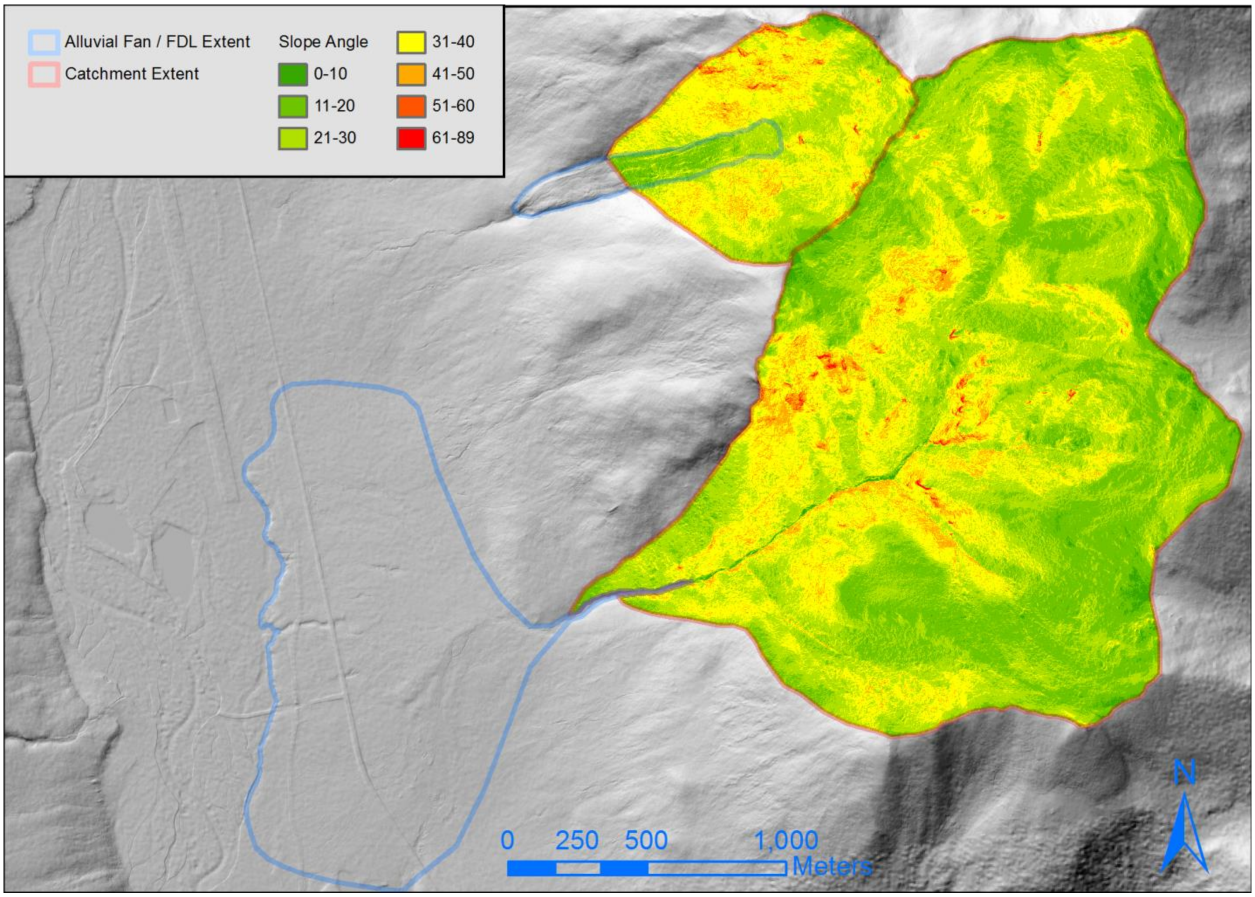

Figure C.3. Slope angle distributions of FDL-2 and NDL-4 catchments.

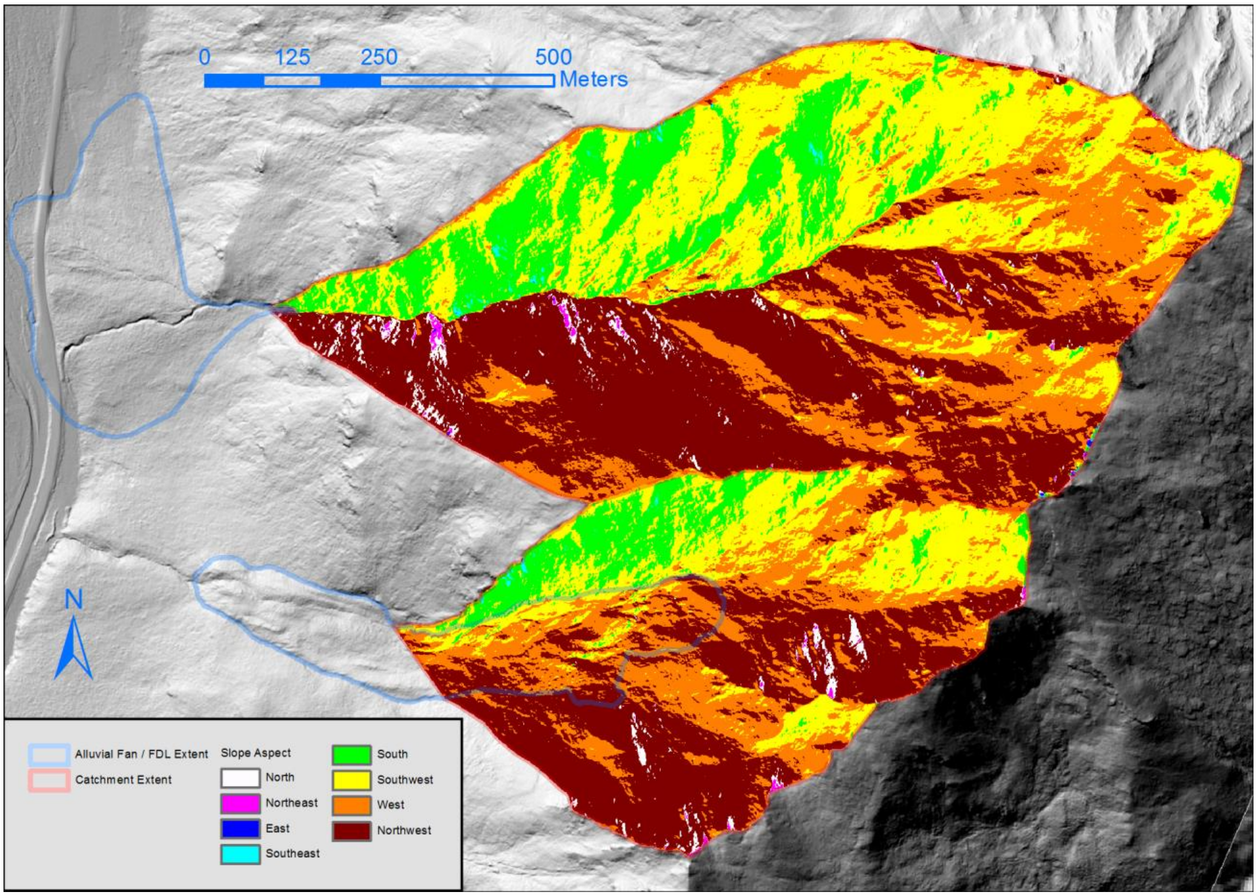

Figure C.4. Aspect distributions of NDL-1 and FDL-11 catchments.

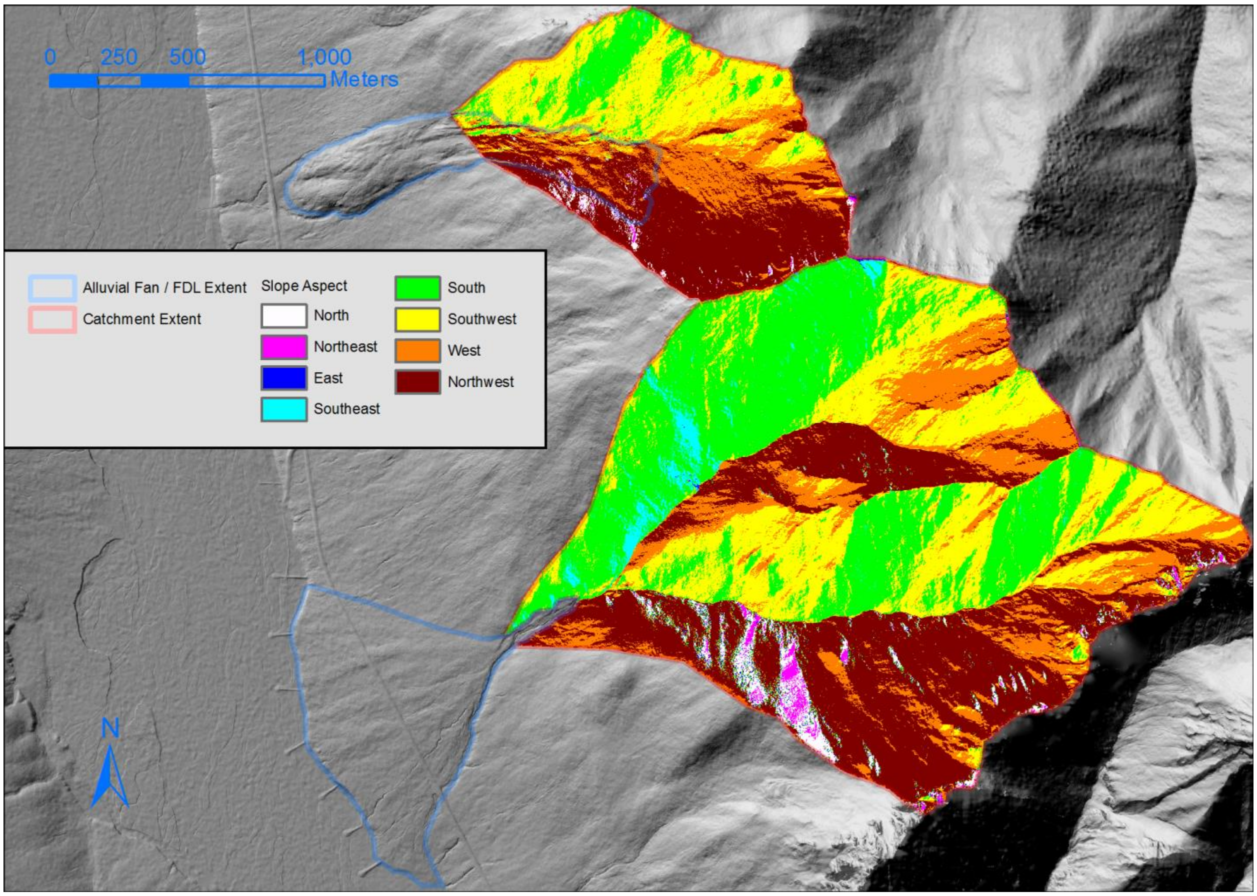

Figure C.5. Aspect distributions of FDL-A and NDL-2 catchments.

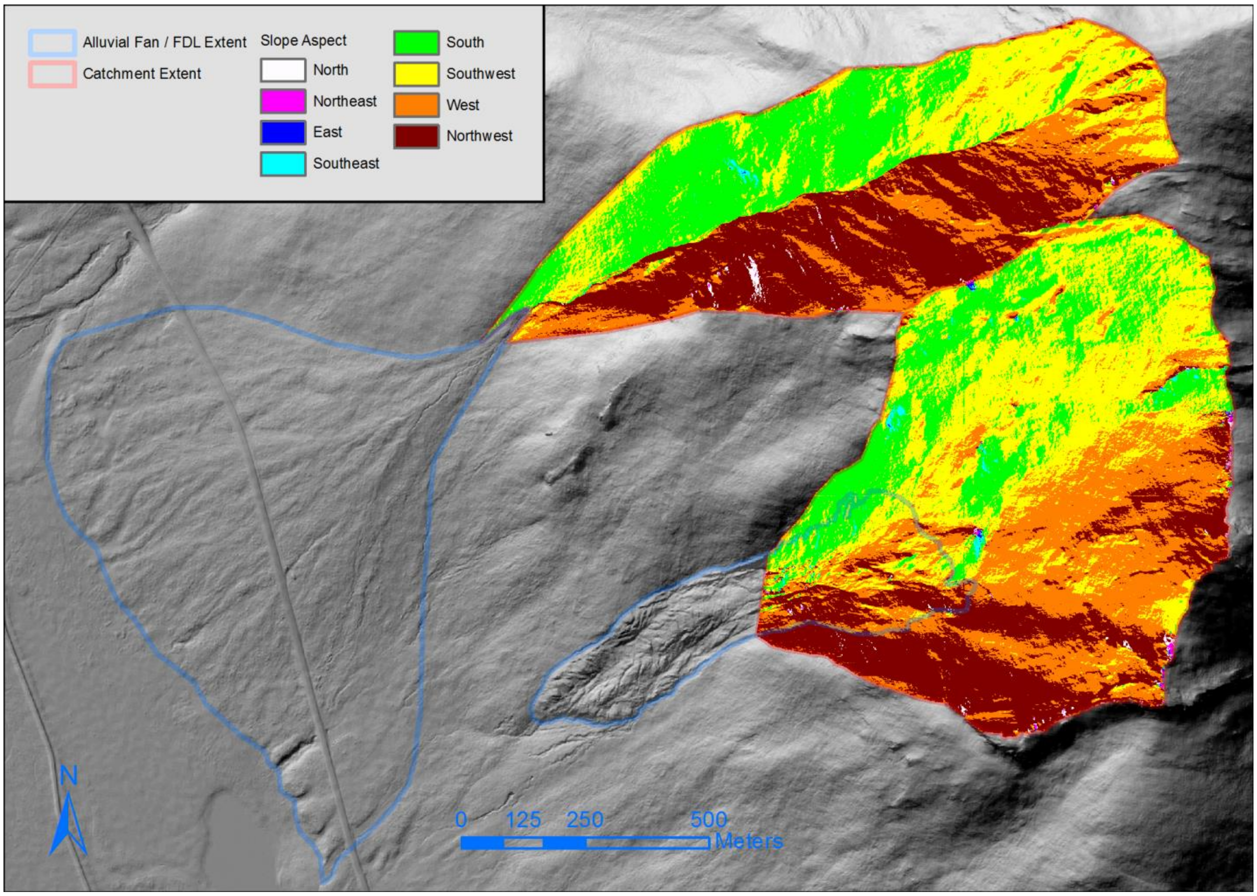

Figure C.6. Aspect distributions of NDL-3 and FDL-D catchments.

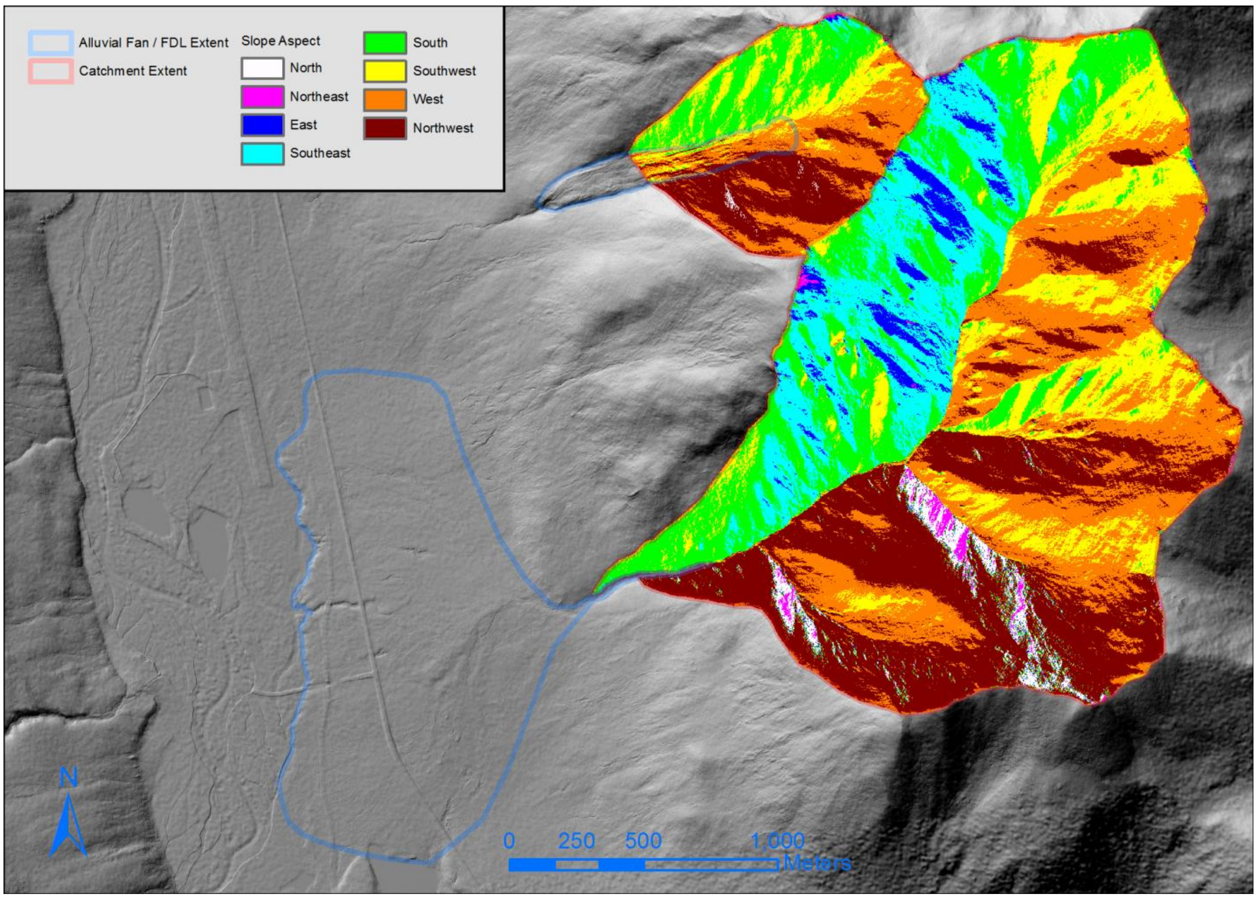

Figure C.7. Aspect distributions of FDL-2 and NDL-4 catchments.